THE UNIVERSITY *of* EDINBURGH

Differential equations on metric graphs: continuum and numerical methods

Sidney Holden

Doctor of Philosophy
University of Edinburgh
2024

Declaration

I declare that this thesis was composed by myself, that the work contained herein is my own except where explicitly stated otherwise, and that this work has not been submitted for any other degree or processional qualification except as specified.

(*Sidney Holden*)

To my family.

Abstract

Continuum modelling has proven exceedingly useful throughout science by assuming the infinite divisibility of a given system. However, high-density metric graphs—representing a range of natural and engineered systems—have seen limited modelling in this way. A metric graph is what one might expect intuitively: a spiderweb, neuronal network, water-supply system, or the British Rail. Physical continuity allows for one-dimensional differential equations along each edge. At vertices, solutions satisfy flux-balance conditions. We study the eigenvalues and eigenfunctions of the Laplace operator on an increasingly dense graph within a prescribed embedding space, e.g., a spiderweb filling the unit disc. The continuous, linear eigenvalue problem on the edges reduces to a discrete, nonlinear eigenvalue problem on the vertices. Numerically, solutions require a novel matrix-determinant root-finding algorithm. Alternatively, the discrete system becomes the eigenvalue equation of a continuous partial differential operator, resembling a Laplace–Beltrami operator but with several notable differences. Rather than a Riemannian metric, we derive a distinct symmetric tensor that scales linearly with distance. Rather than the determinant-based volume form, we find an analogous matrix-trace-based distance form. Our findings open the possibility for a new manifold geometry similar to geodesic structure but made from underlying "graph material". We discuss a series of examples of high-density networks, comparing PDE solutions to numerical solutions of vertex systems. We start with trivial cases and proceed to inhomogeneous and anisotropic media. We develop continuum models for random graphs, hierarchical networks, and cases of nonuniform edge conductances and capacities.

Lay Summary

Networks appear throughout the real world. Classic examples include the humble spiderweb, the not-so-humble neuronal network of the human brain, the Manhattan road network, electricity grids, river systems, social networks, vascular networks... These networks facilitate the spread of mechanical waves, electricity, sound, traffic, information, water, blood... The idea of this thesis is to develop a framework for understanding differential equations (the models of how these quantities spread) on metric graphs (networks) *when the networks are high-density*. Under a microscope, the capillary system of the human lung may be recognisable as any other branching tree or plant in your garden. However, as a whole, the 300 billion capillaries "fill in" the lung into which they are embedded and which they service. A feature of a such a network is that it can route and reroute oxygen and nutrients at various scales–from distributing locally between small groups of capillaries, to distributing globally on the scale of the entire embedding space. This large-scale capability enables networks to be robust to damage or defects, for example. Modelling this capability is crucial for understanding how these systems work. For a simple but foundational differential equation, which models waves, heat, and electrons, we determine how the density and structure of the network, as well as the shape and size of the embedding space, affect these large-scale dynamics. We find a new differential equation and framework, which we hope will be instructive in understanding large-scale behaviour of many extremely large networks which have remained elusive so far.

Contents

Acknowledgements

Along with being an incredible intellectual and interpersonal journey, a PhD is a battle with onself. I am deeply grateful to everyone who I have had on my side.

It is hard to put into words the appreciation I have for my advisor and mentor, Geoff Vasil. It is bittersweet to be finishing my PhD–it has been an utter joy working with him. I am lucky to call him a dear friend and I look forward to maintaining our collaboration into the future. I am also very grateful to Geoff's partner, Marisa Edwards, for her support (and food!) over the years.

I am particularly grateful to my thesis committee, Jacques Vanneste and Matthew Colbrook, for much useful feedback, and suggestions for future work. Thank you to my associate advisor, Alex Morozov, for general advice and for receiving my weekly thesis updates. I am grateful to all the other academics and colleages who I met during my time at the University of Edinburgh. To Echo and Katya; Miru, James and the rest of the PhD students–I have had many moments that I will cherish.

Thank you to the Dedalus team for the advice and for hosting me on various occasions. Thank you also to everyone at CCB at the Flatiron Institute for hosting me during the 2023 Summer–my advisor, Adam Lamson, in particular.

To those in Sydney, where I started, I am particularly grateful to my undergraduate supervisor, Robby Marangell. He was the catalyst for this entire journey, fatefully introducing me to Gregory Berkolaiko's "An elementary introduction to quantum graphs". I should have known better when Geoff intruded into one of our first meetings and remarked: "Ha! Elementary! Sure.". While I am at it, I am grateful to Gregory Berkolaiko who, though I have never met him, did make the effort to reply to a question I once emailed him as a clueless undergraduate, and who co-authored the standard reference on quantum graphs [1] which I have relied on relentlessly. I am also grateful to my fellow undergraduate and PhD students in Sydney: Mitch, Zach, Cecilia, Maddie...

Lastly, to Mum, Dad, Belle, Gough, Mary, and all my friends, family, housemates–thank you for everything.

It has been a truly wonderful adventure.

All of my love.

Chapter 1

Introduction

1.1 Problem statement

This thesis reports a new macroscopic medium that emerges systematically from a dense network of interconnected wires or conduits. The mathematical notion of a *discrete* graph dates back to Euler's 1726 solution of the Seven Bridges of Königsberg problem, abstracting the city's street network to a discrete collection of pairwise relations between nodes. But perhaps a more overt definition would "address" the thoroughfares as contiguous physical connections between junctions. In this case, the appropriate structure is a "metric graph" a.k.a. "geometrised network" a.k.a. "continuous graph": a discrete graph with physical length along each edge. A significant advantage of metric graphs over their discrete counterparts is that they support the placement of *differential equations* along their edges. Metric graphs are ubiquitous, whether in optical fibre networks, electrical power grids, spider webs, vasculature, river systems, neuronal networks, textiles, fishing nets, or British Rail. Moreover, metric graphs find application in diverse and less obvious abstract settings, such as microwave lattices, quantum chemistry, and dynamical systems theory. We embed a metric graph within some common space (e.g. a smooth manifold such as Euclidean space or the 2-sphere). We pose a typical dynamical model as a one-dimensional differential equation on each edge, with "boundary" conditions at each vertex. Overall, the dynamics on a given edge depend on the dynamics over the entire graph. In this sense, we envision a kind of "*meso*scopic" system giving way to fully coarse-grained dynamics.

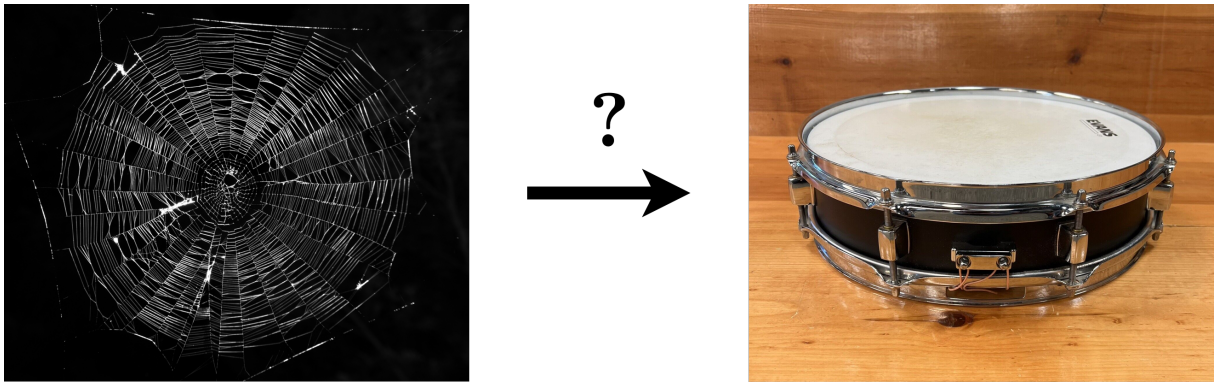

Figure 1.1: Does a high-density spiderweb vibrate like a snare drum?

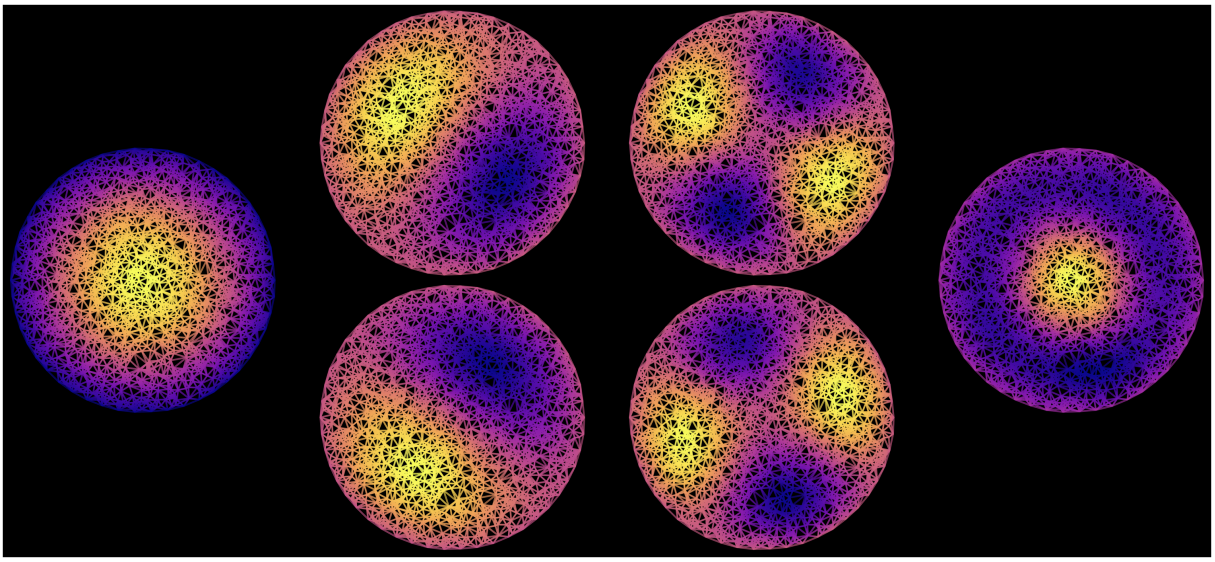

Figure 1.2: Large scale (*edgewise*) modes on metric graphs. How can these be modelled in the continuum?

The overall question we address is:

> *What partial differential equations result from taking the "continuum limit" of the metric graph, where the vertices become dense in the embedding space, and the edge lengths shrink to zero (figure 1.1)?*

We answer this question for the eigensystem of the Laplace operator $\Delta = d^2/dx^2$ eq. (2.12) on each edge of a given metric graph G and find the resulting PDE is eq. (2.42). We chose the differential Laplacian as a starting point because of its presence in innumerable applications. In line with Mark Kac's *"Can you hear the shape of a drum?"* [2] (you can't [3]), we refer to eigenvalues of the Laplace operator on metric graphs as simply eigenvalues of metric graphs–and no, you can't hear the shape of a metric graph [4], *unless* the edge lengths are rationally independent [5, 6]. There has been significant work studying differential equations on metric graphs, mainly focusing on quantum Hamiltonian Schrödinger operators, $\mathcal{H} = -\Delta + V(x)$ [1]. Linus Pauling first considered differential equations on metric graphs to model free electrons in organic molecules [7]. Recent modelling efforts include Hamiltonian dynamics in hydrocarbons [8–11] and low-energy eigenmodes of protonated methane [12, 13] using similar, 60 vertex models to the truncated icosahedron (buckminsterfullerene) in figure 5.5. Particular excitement exists regarding nanomaterials for their remarkable mechanical, electric and optical properties [14–22]. The Schrödinger equation on metric graphs is also equivalent to the telegraph equation on microwave networks [23–27]. Localisation landscape theory provides a promising model for charge-carrier dynamics in disordered semiconductors [28–33]. Anderson localisation has been studied extensively on quantum graphs [34–38]; including in random laser networks [39–43].

For biological applications, the brain presents an especially intriguing setting for high-density graph models [44–53]. However, comparatively little work has included Euclidean distances on the underlying graphs; only how distance affects neuron firing rate synchronisation [54, 55]. The cellular cytoskeleton network of protein filaments is another key area for metric graph applications [56–60].

Mathematical results for differential equations on metric graphs include hybrid monographs covering the nonlinear Schrödinger and reaction-diffusion equations [61–63]. Other examples include thin-branched structures [64, 65], control problems [66], and semigroup methods for evolution equations [67]. A related work [68] demonstrates how a discrete lattice of wires can nevertheless efficiently filter electromagnetic radiation as would a continuous substance. Lieb *et al.* solve and optimise a system of nonlinear conservation laws on idealised urban water-supply networks [69].

Little is understood regarding high-density metric graphs as embedded structures within manifolds. Previous work treats graphs with high levels of symmetry [1, 70–77]. Applications exist in the human circulatory system [78, 79], population dynamics [80], tissue membranes [81] and urban pollution [82]. Lastly, [83] shows Ollivier-to-Ricci curvature convergence for edges with positive weights.

1.2 Outline

In this thesis, we first introduce metric graphs and the edgewise Laplace operator with self-adjoint boundary conditions in chapter 2. We derive a continuum limit from a variational formalism as we take the limit as the density of vertices increases. We make several initial observations about the resulting operator, and introduce a generalization to edgewise constant parameters (edgewise conductivities and capacities). Before analysing a series of examples, we present numerical algorithms for solving the edgewise nonlinear eigenvalue problem, in chapter 3. In chapter 4, we present the first series of simple initial examples which give intuition about the distinction between the continuum limiting operator and the standard Laplace-Beltrami operator. In chapter 5, we demonstrate the limit for graphs with varying structure, and derive a series of semi-analytical examples. Until then, all graphs have explicitly resolvable local structure which produce well-defined continuum limits. In chapter 6, we apply a metric graph version of two-scale homogenization to graphs with periodic, highly oscillatory structure at the scale of vertex neighours. This sets us up to finally generalise to random graphs in chapter 7. Here, we present a continuum limit of the metric graph Laplace operator on the uniformly random triangulation of space.

Chapter 2

Continuum limit of the *metric* graph Laplace operator

2.1 Mathematical setup

2.1.1 Metric graphs

A graph $G = (V, E)$ consists of a set of vertices $v \in V$, pairs of which are connected by edges $e \in E$. A metric graph is a *weighted* graph, where the weights consist of edge lengths ℓ_e given by the standard one-dimensional Euclidean metric. We also use the notation $G = (V, E)$ to refer to metric graphs. In set notation, the numbers of vertices and edges are $|V|$ and $|E|$, and the graph *size*, unless stated otherwise, is $|V| < \infty$. An edge $e \in E$ connects vertices $v, w \in V$, which are, therefore, neighbours. In a metric graph, an edge is not just a label, but an interval $e = [0_e, \ell_e] \subset \mathbb{R}$ with some coordinate $x \in e$. Here, 0_e corresponds to the starting vertex, say v, and the edge length ℓ_e corresponds to the end vertex, say w. We denote these associations as $v \simeq 0_e$, $w \simeq \ell_e$. A weighted and oriented $|V| \times |E|$ *incidence matrix* $B_{v,e}$ encodes the internal structural information

$$B_{v,e} = \begin{cases} +\ell_e & \text{if} \quad v \simeq 0_e \in [0_e, \ell_e], \\ -\ell_e & \text{if} \quad v \simeq \ell_e \in [0_e, \ell_e], \\ 0 & \text{otherwise.} \end{cases} \tag{2.1}$$

The incidence matrix helps to define functions and their derivatives on G. The signs of the incidence matrix entries, $\hat{B}_{v,e} = \text{sign}(B_{v,e})$, are unit normal vectors pointing away from v. For example, if $v \simeq \ell_e$, then for $x \in e$ with endpoints v and w, $x + \hat{B}_{v,e}$ points away from v and $x + \hat{B}_{w,e}$ points towards v. *Global* coordinates on G are denoted (e, x), where x is the local coordinate on e. We refer to e as a subset of G, and v as an element of G.

2.1.2 Functions and derivatives

We denote scalar-valued functions $f : G \to \mathbb{R}$ as $f(e, x)$ for $x \in e$ (see figure 2.1 for an illustration). A function is *continuous* on G if it is continuous on all individual edges up to and including the endpoints. The endpoints of adjacent edges are the same unique

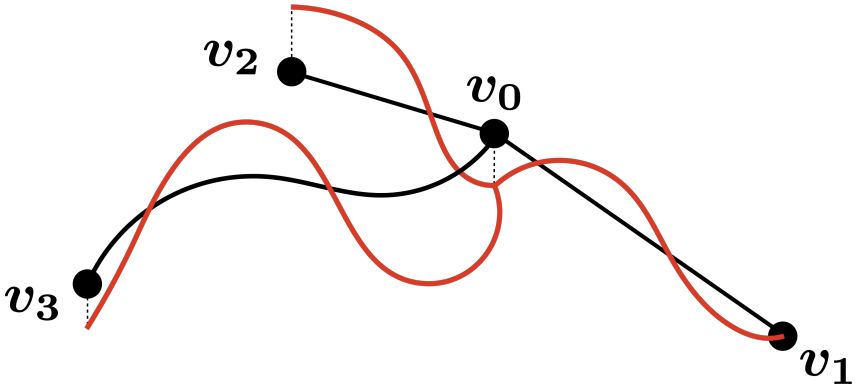

Figure 2.1: Real-valued function f (in red) on G (in black). Neumann-Kirchhoff conditions are enforced at v_0, v_2, v_3 and the Dirichlet 0 condition is enforced at v_1.

point $v \in G$. Therefore, a continuous function on G also has unique values at the vertices, denoted $f(v)$. Differentiability on metric graphs is straightforward in the middle of the edges. For $x + \varepsilon\,\hat{n} \in e$ where $\varepsilon > 0$ and $\hat{n} \in \{\pm 1\}$, a real-valued function $f : G \to \mathbb{R}$ is *edgewise differentiable* if the following exists,

$$D_{\hat{n}} f(e,x) \;=\; \lim_{\varepsilon \to 0} \frac{f(e, x+\varepsilon\,\hat{n}) - f(e,x)}{\varepsilon} \;=\; \hat{n}\,\frac{d}{dx} f(e,x). \tag{2.2}$$

Functions need not have unique derivatives at vertices. The derivative at v is an edgewise function

$$D_e f(v) \;=\; \hat{B}_{v,e}\,\frac{d}{dx} f(e,x)\Big|_{x=v}. \tag{2.3}$$

This is a coordinate-parameterisation invariant directional derivative *away* from v.

2.1.3 The Laplace operator

We define the L_2 inner product over the whole graph as the sum of L_2 inner products on each edge. For complex-valued functions f, g on G,

$$\langle f, g \rangle_G \;=\; \sum_{e \in E} \int_{0_e}^{\ell_e} f(e,x)\overline{g(e,x)}\,\mathrm{d}x, \tag{2.4}$$

with norm, $\|f\|_G = \sqrt{\langle f, f\rangle_G}$. We can associate an L^2 Hilbert space and an $H^2 = W^{2,2}$ Sobolev space to each edge, and by extension to the whole graph as

$$L^2(G) \;:=\; \bigoplus_{i=1}^{|E|} L^2\left([0,\ell_i]\right) \quad \text{and} \quad H^2(G) \;:=\; \bigoplus_{i=1}^{|E|} H^2\left([0,\ell_i]\right). \tag{2.5}$$

The Laplace operator $\Delta : H^2(G) \to L^2(G)$ acts edgewise as

$$\Delta f(e,x) \;=\; \frac{d^2}{dx^2} f(e,x). \tag{2.6}$$

To ensure self-adjointness, we must specify boundary conditions on each edge interval. [1] derives a full classification of boundary conditions which ensure self-adjointness. We derive "natural" vertex conditions by applying a graph analogue of the Rayleigh-Ritz extremum principle on standard manifolds. We define the Dirichlet energy over G as

$$\|Df\|_G^2 \;=\; \sum_{e\in E}\int_{0_e}^{\ell_e}\left|\frac{d}{dx}f(e,x)\right|^2 \mathrm{d}x. \tag{2.7}$$

This is independent of the edge orientations because $\hat{B}_{v,e}^2 = 1$. We define the eigenfunctions of the Laplacian from the stationary points of the Rayleigh quotient, starting with eigenvalue

$$k^2 \;=\; \min_{\|f\|_G=1}\|Df\|_G^2. \tag{2.8}$$

For any globally continuous and differentiable variation $g(e,x)$, the Euler-Lagrange equations are

$$\sum_{e\in E}\left\{\left[g(e,x)\frac{d}{dx}f(e,x)\right]_{0_e}^{\ell_e} - \int_{0_e}^{\ell_e} g(e,x)\left(k^2+\frac{d^2}{dx^2}\right)f(e,x)\,\mathrm{d}x\right\} \;=\; 0. \tag{2.9}$$

The boundary term is

$$\sum_{e\in E}\left[g(e,x)\frac{d}{dx}f(e,x)\right]_{0_e}^{\ell_e} \;=\; \sum_{e\in G}\left(g(e,\ell_e)\frac{d}{dx}f(e,\ell_e) - g(e,0_e)\frac{d}{dx}f(e,0_e)\right). \tag{2.10}$$

We restrict ourselves to cases in which vertex conditions are local. That is, function values at a vertex v do not depend directly on function values at other vertices–only on the values at v of functions on incident edges. In order for this to vanish, there are two natural options. If f satisfies Dirichlet conditions at each v, then we have $g(e,v) = 0$. Alternatively, the *Kirchhoff condition* is

$$\sum_{e\sim v} D_e f(v) \;=\; 0, \tag{2.11}$$

where the sum is over all edges e incident to v denoted $e \sim v$. The edge orientations $\hat{B}_{v,e}$ account for the sign differences between ℓ_e and 0_e in eq. (2.10). In either case, we have the edge differential equation

$$\frac{d^2}{dx^2}f(e,x) \;=\; -k^2 f(e,x). \tag{2.12}$$

The Kirchhoff condition (eq. (2.11)) shows why relevant functions often have multi-valued derivatives at vertices. Δ is self-adjoint when restricted to a dense domain $\mathcal{D} \subset H^2(G)$ on which eq. (2.10) vanishes [1]. The eigenvalue $\lambda = -k^2$ is real-valued and discrete and could represent (e.g.) heat diffusion ($\partial_t \to -k^2$), wave-like dynamics ($\partial_t^2 \to -k^2$), or Schrödinger evolution ($-i\partial_t \to -k^2$).

If a given edge e has endpoints $v \simeq 0_e$, $w \simeq \ell_e$, then we express solutions of eq. (2.12)

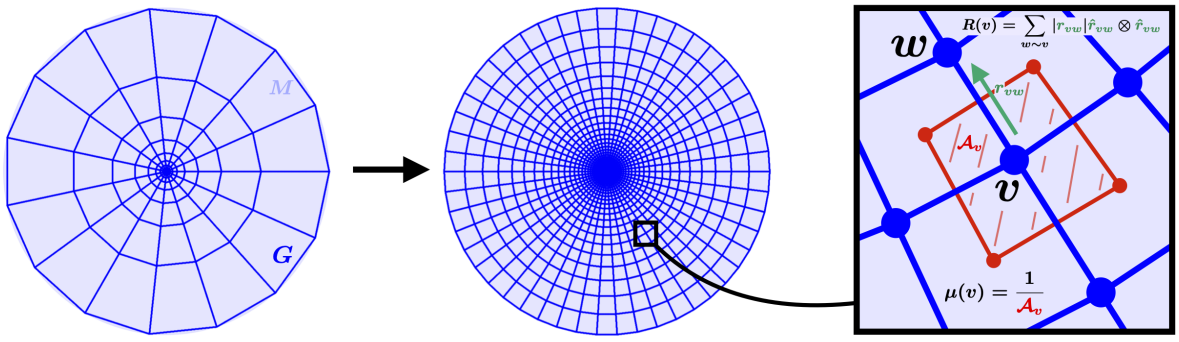

Figure 2.2: An illustration of the continuum limiting graph quantities. The *edge* tensor sums over (tensor products of) displacements to neighbouring vertices. It has units of length. The *vertex* density can be approximated the inverse of the cell area $\mathcal{A}$.

as

$$f(e,x) \;=\; f(v)\frac{\sin(k(\ell_e - x))}{\sin(k\ell_e)} + f(w)\frac{\sin(kx)}{\sin(k\ell_e)}, \tag{2.13}$$

which manifestly expresses continuity with $f(e,0_e) = f(v)$ and $f(e,\ell_e) = f(w)$. Here, we require that $k \neq \frac{n\pi}{\ell_e}$ for $n \in \mathbb{N}$. Such values of k correspond to Dirichlet eigenvalues of Δ. This is because if we set Dirichlet conditions $f(v) = f(w) = 0$ at the endpoints of e, we obtain the standard clamped vibrating string condition

$$\sin(k\ell_e) \;=\; 0. \tag{2.14}$$

In general, we will apply continuity and the Kirchoff condition eq. (2.11) at vertices. Later, when setting up continuum limiting boundary value problems, we will often set the Dirichlet condition $f(v) = 0$ at predefined "boundary vertices" $\partial V \subset V$.

2.1.4 The metric graph Kirchoff condition

Given eq. (2.13), we have

$$\frac{d}{dx}f(e,x) \;=\; k\left(-f(v)\frac{\cos(k(\ell_e - x))}{\sin(k\ell_e)} + f(w)\frac{\cos(kx)}{\sin(k\ell_e)}\right). \tag{2.15}$$

Substituting this into eq. (2.11), we obtain

$$\sum_{w\sim v} \csc(k\ell_{vw})f(w) - \cot(k\ell_{vw})f(v) \;=\; 0, \tag{2.16}$$

where the sum is over every neighbour w of v, denoted $w \sim v$, and ℓ_{vw} is the length of the edge connecting v and w. Over the entire vertex set, we then have the algebraic system

$$L(k)f(V) \;=\; 0, \tag{2.17}$$

where

$$f(V) \;=\; \begin{pmatrix} f(v_1) & f(v_2) & \cdots & f(v_{|V|}) \end{pmatrix}^T \tag{2.18}$$

is the vector of values of f at each vertex and

$$L_{vw}(k) \;=\; \begin{cases} -\csc(k\ell_{vw})\,, & \text{if } w \sim v \\ \sum_{w\sim v} \cot(k\ell_{vw})\,, & \text{if } w = v \\ 0, & \text{otherwise.} \end{cases} \tag{2.19}$$

This is a weighted, graph Laplacian-like matrix function of the spectral parameter k. Indeed, it has the same sparsity structure as the graph (or discrete or combinatorial) Laplacian $L = D - A$ where the (diagonal) degree matrix D and the adjacency matrix A are defined as

$$D_{vw} \;=\; \begin{cases} \deg(v), & \text{if } w = v, \\ 0, & \text{otherwise,} \end{cases} \quad ; \quad A_{vw} \;=\; \begin{cases} 1, & \text{if } w \sim v, \\ 0, & \text{otherwise.} \end{cases} \tag{2.20}$$

Eq. (2.17) is a finite, *nonlinear eigenvalue problem* (NEP), which itself has eigenvalues k and eigenvectors $f(V)$. We demonstrate the theory for such eigenvalue problems and a custom solution method in chapter 3.

In summary, we refer to the *edgewise Laplace operator* as the Laplace operator acting on functions $f \in \mathcal{D} \subset H^2(G)$, with continuity and Kirchoff's condition at all vertices except for some possibly empty set of Dirichlet vertices at which $f = 0$. The eigenvalues/vectors $(k, f(V))$ of the graph NEP eq. (2.17) provide the eigenvalues/functions $(-k^2, f)$ of the edgewise Laplace operator in eq. (2.12). An edgewise eigenfunction $f : G \to \mathbb{R}$ of the edgewise Laplace operator is the union of the edge eigenfunctions in eq. (2.13).

2.2 Continuum limit

The purpose of this thesis is to derive the continuum limit of the edgewise Laplace operator as the graph G fills in some embedding space M densely. A simple example is the square $N \times N$ grid G filling in the planar unit square $M \subset \mathbb{R}^2$ as $N \to \infty$ (figure 2.3). Does the union of the edge eigenfunctions (eq. (2.13)) of the edgewise Laplace operator converge to the eigenfunction $f : M \to \mathbb{R}$ of some continuum limiting partial differential operator? As we have just seen, one can construct a metric graph by simply positing a set of intervals with certain identifications between interval endpoints. To enable the notion of graph density, we pick some embedding space M along with a graph type and a space-filling procedure. We consider a variety of bounded regions of Euclidean space (discs, squares...) and compact Riemannian manifolds (with or without boundary) (n-tori, n-spheres,...) as embedding spaces. The vertices $v \in M$ are then points of the embedding space. The edges are either parametrised curves $e : [0, \ell] \to M$, with lengths given by the metric of the embedding space, or could be straight chords embedded within a higher-dimensional Euclidean space. In the continuum limit, both options will give the same result: for any two adjacent vertices, $w \sim v$, we take the limit as $\ell_{vw} \to 0$ but allow the number of

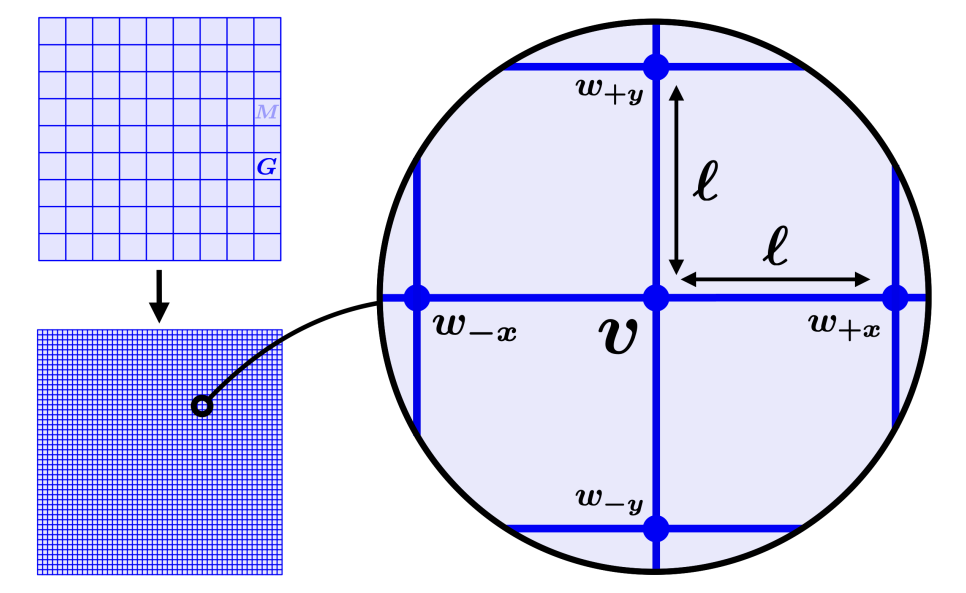

Figure 2.3: A simple first example of the continuum limit setup.

vertices to fill in densely in M.

2.2.1 Continuum limit of bilinear form

To derive a formal continuum limit of the edgewise Laplace operator we first construct a manifestly symmetric bilinear form corresponding to the eigenfunction vertex condition eq. (2.16). We then take the continuum limit of this finite-dimensional bilinear form, invoking a vertex number density with respect to the underlying Riemannian volume measure. Finally, we derive the corresponding extremizing PDE condition as the formal continuum limit.

The vertex condition eq. (2.16) is equivalent to

$$\sum_{w\sim v} \cot(k\ell_{vw})\, f(v) - \cot(k\ell_{vw})\, f(w) - \csc(k\ell_{vw})\, f(w) + \cot(k\ell_{vw})\, f(w) \;=\; 0 \qquad (2.21)$$

$$\sum_{w\sim v} \cot(k\ell_{vw})\, (f(v) - f(w)) - \tan\left(\frac{1}{2}k\ell_{vw}\right) f(w) \;=\; 0 \qquad (2.22)$$

This is the first-order stationarity condition of the following quadratic form,

$$Q(f) \;=\; \sum_{v\in V}\sum_{w\sim v} \cot(k\ell_{vw})\, (f(v) - f(w))^2 - 2\tan\left(\frac{1}{2}k\ell_{vw}\right) f(v)f(w). \qquad (2.23)$$

We assume the embedding space M has a Riemannian structure with a natural volume measure. To take the continuum limit of the graph, we require a *vertex number density*, $\mu(x)$, such that for all sufficiently coarse-grained subsets $S \subseteq G$,

$$\int_S \mu(x)\mathrm{d}x \;=\; \text{number vertices} \in S. \qquad (2.24)$$

The function, $\mu(x)$, is the Radon-Nikodym derivative with respect to the Riemannian measure on the manifold. Trivially, we can use the empirical measure on the vertices

$$\mu_V(x) \;=\; \sum_{v\in V} \delta(x-v). \tag{2.25}$$

Then we have

$$\sum_{v\in V} f(v) \;=\; \int_M f(x)\mu_V(x)\mathrm{d}x. \tag{2.26}$$

Under suitable conditions, the empirical measure converges weakly to a continuum limit μ as the graph becomes dense. In practice, we approximate μ with a finite number N of orthonormal basis functions of $L^2(M)$:

$$\mu_N(x) \;=\; \sum_{p\leq N} a_p(c)\psi_p(x) \tag{2.27}$$

for coefficients $a_k(c)$. These coefficients are given via the orthonormality relation, with

$$\begin{aligned} a_p(c) \;&=\; \int_M \mu_N(x)\psi_p(x)\mathrm{d}x &(2.28)\\ &=\; \int_M \sum_{v\in V} \delta(x-v)\psi_p(x)\mathrm{d}x &(2.29)\\ &=\; \int_M \sum_{v\in V} \psi_p(v)\mathrm{d}x. &(2.30)\end{aligned}$$

Therefore

$$\mu_N(x) \;=\; \sum_{p\leq N} \psi_p(x) \sum_{v\in V} \psi_p(v). \tag{2.31}$$

In the examples of this thesis, we find a sufficient representation to be

$$\mu_N(x) \;\approx\; \frac{1}{|\mathcal{A}_v|}, \tag{2.32}$$

for $x \in \mathcal{A}_v$, the Voronoi cell area (volume in general) surrounding a given vertex (see figure 2.2). This cell area is discussed in detail in section 4.1. It corresponds to the region that is closer to v than any other vertex. This is the standard form used in finite element theory. The spectral representation approximates the empirical measure for functions of bounded variation, which is also sufficient to define the weak derivative [84].

We now derive a leading order expression of eq. (2.23) for $\ell_{vw} \to 0$. First, to leading

order, the trigonometric terms are

$$\cot(k\ell_{vw}) \;=\; \frac{1}{k\ell_{vw}} + \mathcal{O}(\ell_{vw}) \tag{2.33}$$

$$2\tan\left(\frac{1}{2}k\ell_{vw}\right) \;=\; k\ell_{vw} + \mathcal{O}\big(\ell_{vw}^3\big)\,. \tag{2.34}$$

The difference term is given by a directional derivative in terms of r_{vw}, the tangent vector at v to M in the direction of the embedded parametrised edge connecting v and w. That is

$$f(w) - f(v) \;=\; r_{vw}\cdot\nabla f(v) + \mathcal{O}\big(\ell_{vw}^2\big)\,. \tag{2.35}$$

We impose a local Riemannian structure when stating $\|r_{vw}\| = \ell_{vw}$ is the geodesic distance along e and $\hat{r}_{vw}\cdot\hat{r}_{vw} = 1$. Now comes the crux of the derivation. We define the following symmetric *edge* tensor at each vertex

$$R(v) \;=\; \sum_{w\sim v} \|r_{vw}\|\,\hat{r}_{vw}\otimes\hat{r}_{vw}, \tag{2.36}$$

$$\mathrm{tr}(R(v)) \;=\; \sum_{w\sim v} \|r_{vw}\|. \tag{2.37}$$

Altogether, to $\mathcal{O}(\ell_{vw}^2)$, we have the continuum functional

$$Q(f) \;=\; \int_M \big(\nabla f(x)\cdot R(x)\cdot\nabla f(x) - k^2\,\mathrm{tr}(R(x))\,f(x)^2\big)\,\mu(x)\mathrm{d}x. \tag{2.38}$$

Note that we have also multiplied through by k to obtain a more recognisable form. We now take the functional variation of Q

$$\frac{d}{d\varepsilon}Q(f+\varepsilon\nu)\Big|_{\varepsilon=0} \;=\; 0, \tag{2.39}$$

for $\nu(\partial M) = 0$. This produces

$$\int_M \big(\nabla\nu(x)\cdot R(x)\cdot\nabla f(x) - k^2\mathrm{tr}(R(x))\,f(x)\nu(x)\big)\,\mu(x)\mathrm{d}x \;=\; 0. \tag{2.40}$$

Integrating by parts

$$\begin{aligned}\int_M \nabla\nu(x)\cdot R(x)\cdot\nabla f(x)\mu(x)\mathrm{d}x \;=\; &\int_{\partial M}\hat{n}\cdot R(x)\cdot\nabla f(x)\,\nu(x)\mu(x)\mathrm{d}x \\ &- \int_M \nabla\cdot(\mu(x)R(x)\cdot\nabla f(x))\nu(x)\mathrm{d}x.\end{aligned} \tag{2.41}$$

where $\hat{n}$ is the unit normal to the boundary. Altogether, we have

$$\frac{1}{\mathrm{tr}(\mu(x)R(x))}\nabla\cdot(\mu(x)R(x)\cdot\nabla f(x)) \;=\; -k^2 f(x), \quad x\in M, \tag{2.42}$$

with the "natural" condition

$$\hat{n} \cdot \mu(x) R(x) \cdot \nabla f(x) \;=\; 0, \quad x \in \partial M. \tag{2.43}$$

We will apply $f(x) = 0$ on ∂M when we set Dirichlet conditions at vertices v filling in ∂M.

In the examples of this thesis, we determine a well-defined continuum limiting PDE for the graphs in question. We know that the operator $\mathcal{L}$ in eq. (2.42) with boundary conditions eq. (2.43) is self-adjoint in $L^2(M, \mu(x)\,\mathrm{tr}(R(x)))$ with real, negative eigenvalues. That is, for

$$\langle f(x), g(x) \rangle \;=\; \int_M f(x) g(x)\, \mu(x)\, \mathrm{tr}(R(x))\, \mathrm{d}x, \tag{2.44}$$

we have

$$\begin{aligned} \langle \mathcal{L} f(x), g(x) \rangle \;&=\; \int_M \nabla \cdot (\mu(x) R(x) \cdot \nabla f(x)) g(x) \mathrm{d}x & (2.45) \\ &= \int_{\partial M} (\mu(x) R(x) \cdot \nabla f(x) g(x)) \cdot \hat{n} \mathrm{d}x - \int_M \mu(x) R(x) \cdot \nabla f(x) \cdot \nabla g(x) \mathrm{d}x & (2.46) \end{aligned}$$

where the boundary term vanishes and integrating by parts again, we have $\langle \mathcal{L} f(x), g(x) \rangle = \langle f(x), \mathcal{L} g(x) \rangle$. Furthermore, we know that $R(x)$ is positive definite at the vertices,

$$u \cdot R(x) \cdot u \;=\; \sum_{w \sim v} \ell_{vw} u \cdot \hat{r}_{vw} \otimes \hat{r}_{vw} \cdot u \;=\; \sum_{w \sim v} \ell_{vw} (u \cdot \hat{r}_{vw})^2 \;>\; 0. \tag{2.47}$$

We can interpolate a sufficiently smoothed tensor to be positive definite in the voids. The empirical measure converges weakly via several interpolations. By standard Sturm-Liouville theory, $\mathcal{L}$ has real, negative eigenvalues, and orthogonal eigenfunctions which form a complete basis of $L^2(M, \mu(x)\,\mathrm{tr}(R(x)))$.

2.3 An introductory example

Consider the square grid G filling in the unit square $M \subset \mathbb{R}^2$ as in figure 2.3. We consider the set $\partial V \subset V$ as the set of boundary vertices lying on the boundary of M. At any interior vertex $v \in V \backslash \partial V$, we know that the vertex density is some constant $\mu(v) = \mu$. Displacement vectors to the neighbours $\{w_{+x}, w_{-x}, w_{+y}, w_{-y}\}$ of v are expressed in terms of the standard basis vectors e_x, e_y:

$$\begin{aligned} r_{v w_{\pm x}} \;&=\; w_{\pm x} - v \;=\; \pm \ell e_x & (2.48) \\ r_{v w_{\pm y}} \;&=\; w_{\pm y} - v \;=\; \pm \ell e_y. & (2.49) \end{aligned}$$

Therefore, the edge tensor is

$$R = \ell\Big(e_x \otimes e_x + (-e_x) \otimes (-e_x) + e_y \otimes e_y + (-e_y) \otimes (-e_y)\Big) \tag{2.50}$$
$$= 2\ell I. \tag{2.51}$$

Altogether, the PDE is

$$\frac{1}{\mu 4\ell} \nabla \cdot (\mu 2\ell I \cdot \nabla f(x)) = -k^2 f(x) \tag{2.52}$$
$$\frac{1}{2}\left(\frac{\partial^2}{\partial x^2} + \frac{\partial^2}{\partial y^2}\right) f(x) = -k^2 f(x). \tag{2.53}$$

We briefly discuss the appearance of this rescaled Laplace operator in the following section, and discuss this specific example further in section 4.3.4

2.4 Tensor comparisons

The edge tensor is analogous to other examples appearing in diverse applications but with a different inverse length scaling. The general form of the summand in the R tensor can be rewritten as

$$q_{vw}^{(\alpha)} = |r_{vw}|^{\alpha}\, r_{vw} \otimes r_{vw} \tag{2.54}$$

For the edge tensor we have $\alpha = -1$.

Nematic comparison For $\alpha = 0$, the conformation (a.k.a neumatic-order) tensor, Q, gives the degree of alignment in liquid crystals [85],

$$Q(v) \propto \sum_w \left(q_{vw}^{(0)} - \frac{1}{d}\operatorname{tr}\big(q_{vw}^{(0)}\big)\, I\right), \tag{2.55}$$

so that $\operatorname{tr}(Q) = 0$ by definition. An isotropic material implies $Q = 0$. For a perfect nematic, Q is a diagonal matrix.

Riemannian comparison At first glance, the continuum limit of the edgewise Laplace operator eq. (2.42) appears similar to the standard Laplace-Beltrami operator on a d-dimensional Riemannian manifold:

$$\frac{1}{\sqrt{\det(g)}} \frac{\partial}{\partial x^i}\left(\sqrt{\det(g)} g^{ij} \frac{\partial}{\partial x^j} f\right) = -k^2 f. \tag{2.56}$$

Here, the x^i are local coordinates for $1 \leq i \leq d$, and g and g^{-1} are the metric and inverse metric tensors expressed in the cotangent and tangent bases $\{dx^i\}$ and $\{\frac{\partial}{\partial x^i}\}$ respectively:

$$g = \sum_{i,j=1}^{d} g_{ij} \mathrm{d}x^i \otimes \mathrm{d}x^j \tag{2.57}$$

$$g^{-1} = \sum_{i,j=1}^{d} g^{ij} \frac{\partial}{\partial x^i} \otimes \frac{\partial}{\partial x^j} \tag{2.58}$$

We can make a closest correspondence as follows. Suppose we are in a manifold with distance and consider two nearby points, $x \approx y$. Then consider the ratio,

$$S(x,y) = \frac{(f(x) - f(y))^2}{\mathrm{dist}(x,y)^2}. \tag{2.59}$$

If $\gamma(t)$ is a parameterised curve connecting $x = \gamma(0)$ to $y = \gamma(t)$. Then as $t \to 0$,

$$S(x,y) \sim \frac{(v \cdot \mathrm{d}f(x))^2}{v \cdot g(x) \cdot v}, \quad \text{as} \quad y \to x, \tag{2.60}$$

where the tangent vector $v = \gamma'(0)$. The local metric tensor at the point x is $g(x)$ and $\mathrm{d}f(x)$ is the local gradient 1-form. The tangent vector, v, does its best to "point" from x to y, the closest analogue to an edge in a metric graph. Because of the definition of the ratio, the magnitude of v cancels out of the total expression. In a local orthogonal basis,

$$g = \sum_{i=1}^{d} h_i \, \mathrm{d}x^i \otimes \mathrm{d}x^i, \tag{2.61}$$

with scale factors $h_i > 0$. A general unit vector is

$$\hat{v}_{\hat{n}} = \sum_{i=1}^{d} \frac{\hat{n}_i}{\sqrt{h_i}} \partial_i, \qquad \text{where} \qquad \sum_{i=1}^{d} \hat{n}_i^2 = 1, \tag{2.62}$$

where $\mathrm{d}x^i \cdot \partial_j = \delta_{i,j}$. That is, $\hat{v}_{\hat{n}} \cdot g \cdot \hat{v}_{\hat{n}} = 1$. There is some direction for a typical point, y, $\hat{n}$ "pointing" at it. Therefore,

$$S(x,y) \sim (\hat{v}_{\hat{n}} \cdot \mathrm{d}f(x))^2 \tag{2.63}$$

If we average this expression over the sphere S^{d-1}, then

$$\begin{aligned} \lim_{y \to x} \langle S(x,y) \rangle &= \frac{1}{|S^{d-1}|} \int_{S^{d-1}} (\hat{v}_{\hat{n}} \cdot \mathrm{d}f(x))^2 \mathrm{d}\hat{n} \\ &= \sum_{i,j} \frac{\langle \hat{n}_i \hat{n}_j \rangle}{\sqrt{h_i h_j}} \partial_i f \, \partial_j f. \end{aligned} \tag{2.64}$$

However, for a unit vector in the sphere, $\langle \hat{n}_i \hat{n}_j \rangle = d^{-1}\, \delta_{i,j}$. Therefore,

$$\lim_{y \to x} \langle S(x,y) \rangle \;=\; \frac{1}{d} \mathrm{d}f(x) \cdot g(x)^{-1} \cdot \mathrm{d}f(x), \tag{2.65}$$

where

$$g(x)^{-1} \;=\; \sum_{i,j} \frac{1}{h_i} \partial_i \otimes \partial_i. \tag{2.66}$$

To make an analogy with the metric graph, with normal vectors along the edges, $\hat{r}_{vw}$,

$$\frac{d}{\deg(v)} \sum_{w \sim v} \hat{r}_{vw} \otimes \hat{r}_{vw} \;\approx\; g(x_v)^{-1}, \tag{2.67}$$

where $\deg(v)$ is the number of neighbours (degree) of vertex v and d is the dimension of space. The inverse Riemannian metric tensor roughly corresponds to $\alpha = -2$ in eq. (2.54). The edge tensor is defined similarly to a discrete approximation of a Riemannian metric, but with a different distance scaling, *i.e.*, with closest correspondence. For Riemannian metrics, $\mathrm{tr}(g) = \dim(M)$ by definition. As far as we know, there is no straightforward way to relate R to other standard tensors commonly defined on Riemannian manifolds. Moreover, the local Riemannian volume measure is $\sqrt{\det(g)}$. There appears to be no simple procedure to obtain the vertex density, $\mu(x)$, in terms of a function of $R(x)$ alone. If we force the following correspondences

$$\mu \mathrm{tr}(R) \;=\; \sqrt{\det g} \quad ; \quad \mu R \;=\; \sqrt{\det g} g^{-1} \tag{2.68}$$

then taking determinants on the second equation,

$$\mu^d \det R \;=\; \det g^{d/2-1} \tag{2.69}$$

and so

$$\mu^2 \;=\; \frac{\mathrm{tr}(R)^{d-2}}{\det R}. \tag{2.70}$$

This is not true in general, and it is unclear whether such a continuum limiting graph structure can be constructed at all. The underlying presence of a metric graph "substance" cannot be described purely in geometrical terms. We can see that the eq. (2.42) gives genuinely distinct behaviour from a traditional Laplace-Beltrami operator, with the main differences resulting from the trace, $\mathrm{tr}(R)$. For a completely homogeneous isotropic graph, the only symmetric rank-2 tensor is proportional to the d-dimensional identity, and as we see in extended detail in chapter 4,

$$R \;=\; \frac{\mathrm{tr}(R)}{d} I_d \quad \Longrightarrow \quad \frac{1}{d} \Delta f \;=\; -k^2 f. \tag{2.71}$$

Isotropy implies $\mathrm{tr}(R) = \ell \deg(v)$ is constant for every vertex. For this special case, eq. (2.42) reduces to the standard Laplace-Beltrami operator, *but weighted by the spatial dimension of the graph embedding.* Overall, the continuum "graph material" can resemble

many other materials but is (roughly speaking) less stiff by the dimension of the embedding space. On square grids [86–89] rigorously prove formal operator convergence to eq. (2.71), particularly commenting about the anomalous dimensional factor.

2.5 Incorporating physical parameters

Here, we take a detour to derive the more general form of the Helmholtz equation. Consider the local conservation of energy,

$$\partial_t E + \nabla \cdot F = 0, \tag{2.72}$$

where E is the energy density and F is the (outward) flux density. That is,

$$\frac{d}{dt}\int_V E\, dV = -\int_{\partial V} F \cdot dA. \tag{2.73}$$

Derive a local entropy density equation,

$$dE = T dS \implies \partial_t S = \frac{\partial_t E}{T}. \tag{2.74}$$

Use the energy equation and integrate over a closed volume,

$$\frac{d}{dt}\int_V S\, dV = -\int_V \frac{\nabla \cdot F}{T}\, dV \geq 0. \tag{2.75}$$

That is, the total entropy in a closed volume can't decrease. However,

$$\nabla \cdot \frac{F}{T} = \nabla \cdot \left(\frac{F}{T}\right) + \frac{F \cdot \nabla T}{T^2}. \tag{2.76}$$

The divergence term vanishes because we are integrating over an isolated volume. Therefore,

$$\frac{d}{dt}\int_V S\, dV = -\int_V \frac{F \cdot \nabla T}{T^2}\, dV \geq 0. \tag{2.77}$$

The only way to guarantee entropy cannot decrease is Fourier's Law of heat conduction,

$$F \;=\; -K\nabla T, \tag{2.78}$$

where $K > 0$ is the *conductivity*. Other than positivity, there are no constraints; it can be nonlinear. More generally, the conductivity could even be a nonlocal tensorial operator, as long as it's positive definite. Therefore, the energy equation is

$$\partial_t E = \nabla \cdot (K \nabla T). \tag{2.79}$$

However, this is not quite done yet because we don't know the direct relation between energy and temperature. This is the heat capacity,

$$dE = C\,dT \tag{2.80}$$

Going back to the definition of temperature,

$$\frac{1}{C} = -T^2 \frac{d^2 S}{dE^2} > 0. \tag{2.81}$$

The positivity of the capacity implies a concave entropy function. Therefore, the general heat equation,

$$C\partial_t T = \nabla \cdot (K \nabla T). \tag{2.82}$$

Notice that this evolves until $T =$ constant in space and time; then it stops. Therefore, now we have a complete list of the classification of every *type* of macroscopic physical parameter

- Entropy: The statistical overlord.
- Energy: A globally time-conserved quantity.
- Energy Flux: The transfer of energy through a physical surface.
- Temperature: The conjugate varible to energy.
- Conductivity: The proportionality factor between temperature and energy flux.
- Capacity: The proportionality factor between temperature and energy.

This argument stays the same if energy is replaced with any other conserved quantity. For example, momentum (conserved), stress tensor (momentum flux), velocity (conjugate), mass density (momentum capacity), and viscosity (momentum conductivity). Of course, what we discuss here is about statistical phonemona that are approaching equlibrium. However, we can also see close similarities with oscillating mechanical systems. In the most general version of the scalar wave displacement equation,

$$\rho\,\partial_t^2 X = \nabla \cdot (\tau \nabla X), \tag{2.83}$$

where ρ is mass density and τ is a tension througout the medium. We can see that treating both dissipation and oscilation as eigenvalue problmes least to the correspondence $\rho \leftrightarrow C$, $\tau \leftrightarrow K$. Even though the time dependence is different, it's clear that mass density is a kind of wave capicity and tension is a kind of wave conductivity. We keep these general ideas in mind when deriving new continuum models from underlying microscopic metric graphs.

We can use a similar derivation from the original continuum limit to incorporate edgewise constant parameters as a way of accounting for physical characteristics of a particular system. A more general Helmholtz equation is

$$\frac{1}{C(x)} \nabla \cdot (K(x) \cdot \nabla f(x)) \;=\; \lambda\, f(x). \tag{2.84}$$

In the heat equation, $K(x)$ and $C(x)$ represent the thermal conductivity tensor and heat capacity respectively. In the wave equation, $K(x)$ is the stress tensor and $C(x)$ is the density. For some graph $G = (V, E)$, consider the modified equation on each edge e

$$K_e \Delta f(e,x) \;=\; \lambda\, C_e\, f(e,x). \tag{2.85}$$

For simplicity, we eventually assume K_e, C_e are constant on e. However, they could depend on length along each edge. We proceed exactly as for the original equation eq. (2.12) in deriving a continuum limit. The corresponding action is

$$\mathcal{L}(f) \;=\; \sum_e \int_{0_e}^{\ell_e} \left(K_e(x) \left| \frac{d}{dx} f_e(x) \right|^2 + \lambda\, C_e(x)\, |f_e(x)|^2 \right) \mathrm{d}x. \tag{2.86}$$

Then the stationarity condition $\delta\mathcal{L} = 0$ gives for all globally continuous and differentiable g

$$\sum_e \int_{0_e}^{\ell_e} K_e(x) f_e'(x) g_e'(x) + \lambda\, C_e(x)\, f_e(x) g_e(x) \mathrm{d}x \;=\; 0 \tag{2.87}$$

$$\sum_e \left[K_e(x) f_e'(x) g_e(x) \right]_{0_e}^{\ell_e} - \int_{0_e}^{\ell_e} \left((K_e(x)\, f_e'(x))' - \lambda C_e(x)\, f_e(x) \right) g_e(x) \mathrm{d}x \;=\; 0. \tag{2.88}$$

For $g_e(0_e) = g_e(\ell_e) = 0$,

$$\partial_x (K_e \partial_x f_e) \;=\; \lambda\, C_e f_e. \tag{2.89}$$

For g_e with support at a single vertex v, the Kirchhoff condition is

$$\sum_{w \sim v} K_{vw}\, D_e f(e_{vw}, v) \;=\; 0, \tag{2.90}$$

where $K_{vw} = K_e$ and $C_{vw} = C_e$ on the edge $e = e_{vw}$ connecting v, w. From here, we specialise to constant edgewise K_e, C_e, which we can do without loss of generality in the short-edge limit. Denoting $k = \sqrt{-\lambda\, C_e / K_e}$, the edge eigenfunctions are as before

$$f(e,x) \;=\; f(v) \frac{\sin(k(\ell - x))}{\sin(k\ell)} + f(w) \frac{\sin(kx)}{\sin(k\ell)}. \tag{2.91}$$

Substituting these into eq. (2.90), we obtain

$$\sum_{w \sim v} \sqrt{C_{vw} K_{vw}}\, (\cot(k\ell_{vw})\, f(v) - \csc(k\ell_{vw})\, f(w)) \;=\; 0. \tag{2.92}$$

The corresponding continuum functional is

$$Q(f) \;=\; \int_M \left(\nabla f(x) \cdot R_K(x) \cdot \nabla f(x) + \lambda\, \mathrm{tr}(R_C(x))\, f(x)^2 \right) \mu(x) \mathrm{d}x, \tag{2.93}$$

where

$$R_K \;=\; \sum_{w\sim v} K_{vw}|r_{vw}|\hat{r}_{vw}\otimes\hat{r}_{vw} \quad ; \quad R_C \;=\; \sum_{w\sim v} C_{vw}|r_{vw}|\hat{r}_{vw}\otimes\hat{r}_{vw}, \tag{2.94}$$

and the corresponding PDE is

$$\frac{1}{\mu(x)\mathrm{tr}(R_C(x))}\nabla\cdot(\mu(x)R_K(x)\cdot\nabla f(x)) \;=\; \lambda\, f(x) \tag{2.95}$$

with

$$\hat{n}(x)\cdot(\mu(x)R_K(x))\cdot\nabla f(x) = 0 \quad \text{for} \quad x\in\partial M. \tag{2.96}$$

We retrieve a form of the general Helmholtz equation eq. (2.84), with separated, spatially varying K and C functions. It is not immediately obvious that this should result from the edgewise equation eq. (2.85). With two parameters on each edge, we now have more flexibility in the types of continuum limits we can construct. For example, we scale out the the anomalous factor of the dimension in eq. (2.71) by enforcing a certain ratio between K and C. If we have a homogeneous and isotropic graph, then $\mu(x)=\mu$ is constant and

$$R_K \;=\; \frac{\mathrm{tr}(R_K)}{d} I_d \qquad ; \qquad R_C \;=\; \frac{\mathrm{tr}(R_C)}{d} I_d. \tag{2.97}$$

Eq. (2.95) then reduces to

$$\frac{\frac{\mathrm{tr}(R_K)}{d}}{\mathrm{tr}(R_C)}\Delta f(x) \;=\; \lambda f(x). \tag{2.98}$$

The condition to retrieve the standard Helmholtz equation is

$$\frac{\mathrm{tr}(R_K)}{\mathrm{tr}(R_C)} \;=\; d. \tag{2.99}$$

On the square grid of the introductory example where $R = 2\ell I$, we can set $R_K = 2\ell K I$ and $R_C = 2\ell C I$ for global constants K, C. Then

$$K \;=\; d\,C. \tag{2.100}$$

Roughly speaking, this suggests that to diffuse information like d-dimensional continuous space, a network of wires needs to have a conductivity (K) that is a multiple d of the capacity (C) on each wire. That is, the wires cannot transfer information as quickly as space, and to make up for this, each wire needs to have a lower capacity to hold information.

2.6 A coarse-grained model–*not* a discretization method

In particular cases, as we have just seen, there may be ways to reproduce the Laplace-Beltrami operator by carefully tuning edgewise parameters. However, the purpose of this thesis is to develop a coarse-grained model of the edgewise Laplace operator, and to study the continuum-like behaviour whatever it may be. In general, our continuum limit and the metric graph problem are not the Laplace-Beltrami operator and a discretization scheme in disguise. We saw a glimpse of this in eq. (2.53), where even on a highly structured grid, we obtained a dimension-scaled Laplace operator. As we will see, on more complicated graphs, the vertex density and edge tensor can produce highly nontrivial continuum limiting PDEs.

Here, we present a comparison with the *cotangent Laplacian* [90], the finite element discretization of the Laplace operator in two dimensions:

$$L_{vw} = \begin{cases} -\frac{1}{2}\left(\cot(\alpha_{vw}) + \cot(\beta_{vw})\right), & \text{if } w \sim v \\ \sum_{\sigma_m} \frac{1}{2}\left(\cot(\alpha_{vw}) + \cot(\beta_{vw})\right), & \text{if } w = v \\ 0, & \text{otherwise,} \end{cases} \tag{2.101}$$

where α_{vw} and β_{vw} opposite angles to v and w as illustrated in 2.6. It turns out that it is only a coincidence that the cotangent function appears both in this discretization and the edgewise Laplace operator's NEP matrix:

$$L_{vw}(k) \;=\; \begin{cases} -\csc(k\ell_{vw}), & \text{if } w \sim v \\ \sum_{w\sim v} \cot(k\ell_{vw}), & \text{if } w = v \\ 0, & \text{otherwise.} \end{cases} \tag{2.102}$$

2.6.1 The cotangent Laplacian

Consider some closed surface S embedded in $\mathbb{R}^3$. Let G be a triangulation of S with vertices V, and let $L_2(G)$ be the space of square integrable functions on G with inner product given by

$$\langle f(x), g(x)\rangle \;=\; \int_G f(x)g(x)\mathrm{d}x \;=\; \sum_m \int_{\sigma_m} f(x)g(x)\mathrm{d}x, \tag{2.103}$$

where σ_m is the mth face (triangular region) of G. For $v, w \in V$, let $\psi_v \in H^1(G)$ be an affine basis (hat) function (as illustrated in figure 2.4) where $\psi_v(w) = \delta_{vw}$. Define functions f as linear combinations of the ψ_i

$$f(x) \;=\; \sum_{w\sim v} f_v \psi_v(x). \tag{2.104}$$

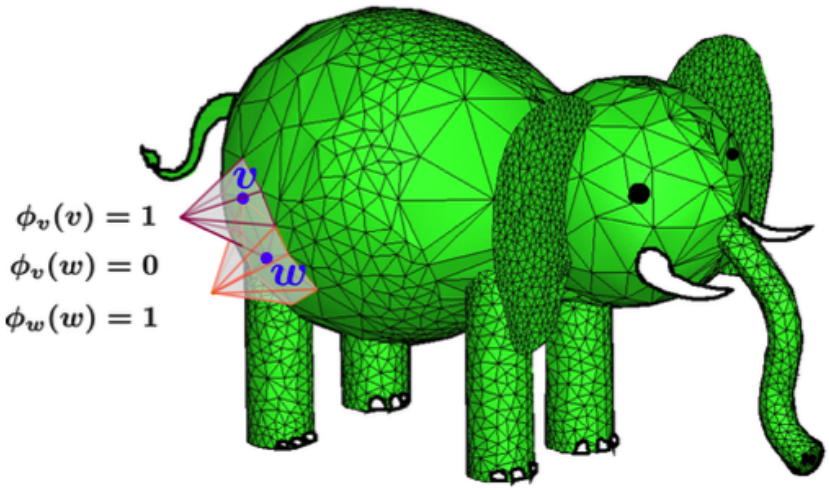

Figure 2.4: Hat functions on a finite elephant [91].

The finite element approximation of the weak form of the eigenvalue equation for the Laplace operator on G is then

$$\sum_v \langle \Delta\psi_v, \psi_w \rangle f_v = \lambda \sum_v \langle \psi_v, \psi_w \rangle f_v \tag{2.105}$$

$$-\sum_v \langle \nabla\psi_v, \nabla\psi_w \rangle f_v = \lambda \sum_v \langle \psi_v, \psi_w \rangle f_v \tag{2.106}$$

We can write this as a matrix equation

$$-Lf(V) = \lambda M f(V), \tag{2.107}$$

where $f(V)$ is the vector of coefficients f_v and $L_{vw} = \langle \nabla\psi_v, \nabla\psi_w \rangle$ and $M = \langle \psi_v, \psi_w \rangle$. We start by determining L. ψ_v is an affine function on each face σ_m (figure 2.5), where it takes the value 1 at v, and 0 along the segment connecting w_0 and w_1. Therefore

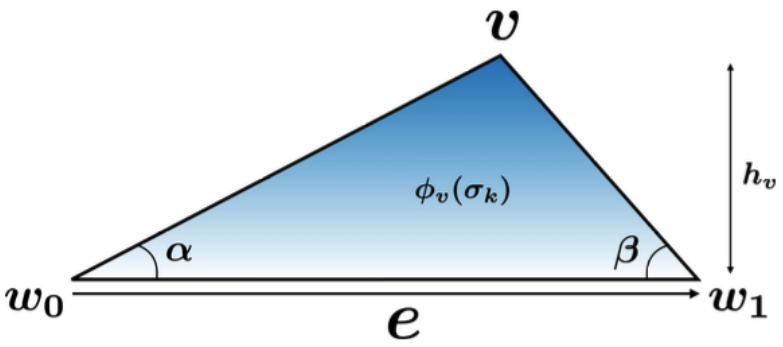

Figure 2.5: ψ_v restricted to a face σ_m.

$\nabla\psi_v(x \in \sigma_m) = \nabla\psi_v$ is constant. We can find the direction and magnitude of $\nabla\psi_v$ by

considering the exact Taylor expansion of ψ_v on σ_m around v:

$$\psi_v(x) \;=\; \psi_v(v) + \nabla\psi_v \cdot (x - v) \;=\; 1 + \nabla\psi_v \cdot (x - v) \tag{2.108}$$

$\nabla\psi_v$ is perpendicular to e:

$$0 \;=\; \psi_v(w_1) - \psi_v(w_0) \;=\; 1 + \nabla\psi_v \cdot (w_1 - v) - (1 + \nabla\psi_v \cdot (w_0 - v)) \;=\; \nabla\psi_v \cdot e. \tag{2.109}$$

If $e^\perp$ is the vector orthogonal to e in the upwards direction and with the same magnitude, then we can then express $\nabla\psi_v$ as

$$\nabla\psi_v \;=\; \|\nabla\psi_v\| \frac{e^\perp}{\|e\|}. \tag{2.110}$$

Next consider

$$\psi_v\left(v - h_v \frac{e^\perp}{|e|}\right) \;=\; 1 + \nabla\psi_v \cdot \left(v - h_v \frac{e^\perp}{|e|} - v\right) \tag{2.111}$$

$$0 \;=\; 1 - \frac{h_v}{\|e\|} \nabla\psi_v \cdot e^\perp \tag{2.112}$$

By the expression for $\nabla\psi_v$ we have

$$\|\nabla\psi_v\|^2 \;=\; \frac{\|\nabla\psi_v\|}{\|e\|} \nabla\psi_v \cdot e^\perp \tag{2.113}$$

$$\psi_v \cdot e^\perp \;=\; \|\nabla\psi_v\| \, \|e\| \tag{2.114}$$

and so eq. (2.112) gives

$$\|\nabla\psi_v\| \;=\; \frac{1}{h_v}. \tag{2.115}$$

If $A_{\sigma_m} = h_v\|e\|/2$ is the area of σ_m, then we finally have

$$\nabla\psi_v \;=\; \frac{1}{2A_{\sigma_m}} e^\perp. \tag{2.116}$$

Now,

$$\int_{\sigma_m} \nabla\psi_v, \nabla\psi_v \mathrm{d}x \;=\; \frac{\|e\|^2}{4A_{\sigma_m}^2} \;=\; \frac{\|e\|}{2h_v} \;=\; \frac{1}{2}(\cot(\alpha) + \cot(\beta)), \tag{2.117}$$

where the last identity comes from straightforward trigonometry on figure 2.5. Applying the exact same procedures at the other vertices, we obtain the other cotangent relations: $\langle \nabla\psi_v, \nabla\psi_{w_0} \rangle = -\frac{1}{2}\cot(\alpha)$ and $\langle \nabla\psi_v, \nabla\psi_{w_1} \rangle = -\frac{1}{2}\cot(\beta)$. Altogether, summing over all

adjacent triangles and relabelling angles as in figure 2.6 we obtain the cotangent Laplacian

$$L_{vw} = \begin{cases} -\frac{1}{2}\left(\cot(\alpha_{vw}) + \cot(\beta_{vw})\right), & \text{if } w \sim v \\ \sum_{\sigma_m} \frac{1}{2}\left(\cot(\alpha_{vw}) + \cot(\beta_{vw})\right), & \text{if } w = v \\ 0, & \text{otherwise.} \end{cases} \tag{2.118}$$

Next, for the mass matrix M, if we parameterize σ_m so that $v = (0,0), w_0 = (a,0)$ and

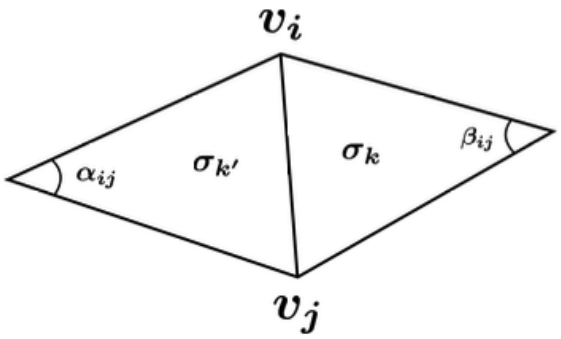

Figure 2.6: Angles for the cotangent Laplacian.

$w_1 = (b,c)$, then

$$\psi_v(x,y) = -\frac{1}{a}x + \frac{b-a}{ac}y + 1 \tag{2.119}$$

$$\psi_{w_1}(x,y) = \frac{1}{c}y. \tag{2.120}$$

Then

$$\langle \psi_v, \psi_{w_1} \rangle_{\sigma_m} = \int_0^b \int_0^{\frac{b}{c}x} \psi_v \psi_{w_1} \mathrm{d}y\mathrm{d}x + \int_b^a \int_0^{\frac{c}{a-b}(a-x)} \psi_v \psi_{w_1} \mathrm{d}y\mathrm{d}x = \frac{1}{12} A_{\sigma_m}, \tag{2.121}$$

and

$$\langle \psi_v, \psi_{w_1} \rangle = \frac{1}{6} A_{\sigma_m}. \tag{2.122}$$

Therefore

$$M_{vw} = \begin{cases} \frac{1}{12}\left(A_{\sigma_m} + A_{\sigma_{m'}}\right), & \text{if } w \sim v \\ \sum_{\sigma_m} \frac{1}{6} A_{\sigma_m}, & \text{if } w = v \\ 0, & \text{otherwise.} \end{cases} \tag{2.123}$$

Finally, we have our full system eq. (2.107). An extension to the n-dimensional cotangent Laplacian is in [92]. This is well known to converge to the Laplace-Beltrami operator under suitable conditions on the graph refinement [93]. In summary, we see that any resemblance between the cotangent Laplacian and the edgewise Laplace operator is superficial.

Chapter 3

Nonlinear eigenvalue problems

The original metric graph Laplace problem is an abstract eigenvalue system, commonly called a "linear eigenvalue" problem.

$$\Delta f \;=\; \lambda\, f. \tag{3.1}$$

Two caveats are relevant here: first, despite its outward simplicity, the system in its current form is infinite-dimensional, hence not solvable exactly without some further intervention. The second caveat is that even though the system is in a traditional "linear" form, any eigenvalue problem is inherently nonlinear because of the multiplication of the eigenvalue and eigenvector, making such systems notoriously tricky in general. Nevertheless, using "linear" to describe finite-dimensional eigenvalue systems makes practical sense because we can bring to bear much of the standard numerical linear algebra tools, especially various matrix factorisations.

One standard way to progress on an infinite-dimensional PDE system like eq. (3.1) is to discretise the continuous spatial structure and build a very large linear matrix-based system that grows with the degree of spatial truncation.

$$\Delta_N \cdot f_N \;=\; \lambda_N\, f_N, . \tag{3.2}$$

where now $N \gg 1$ is a measure of the discretisation, Δ_N is a large finite matrix, f_N is a commensurately large finite vector, and $\lambda_N \approx \lambda$ is an approximation to the real thing that hopefully converges as $N \to \infty$.

However, a big part of the work in this thesis considers an alternate approach that renders the system exactly into a completely finite system, albeit with the added complexity that the resulting matrix depends nonlinearly on the spectral parameter. As usual, defining the alternative parameter, $k = \sqrt{-\lambda}$, we have a general system of the form,

$$L(k) \cdot f(V) = 0, \tag{3.3}$$

where now the "eigenvector" is the exact values of the mathematical function $f(x)$ evaluated at the set of finite vertices, V, and $L(k)$ is a $|V| \times |V|$ linear matrix that depends nonlinearly on the spectral parameter, k. In this sense, we say that eq. (3.3) is a *nonlinear eigenvalue problem* (NEP). While, technically, eq. (3.3) is no more or less linear than before, the lack of general functional form for $L(k)$ makes using standard matrix

factorisations like LU or QR difficult or impossible.

In our case, we have a symmetric matrix trigonometric function of the real-valued parameter, k,

$$L_{vw}(k) \;=\; \begin{cases} \sum_{w\sim v} \cot(k\ell_{vw}) & \text{if } \; w = v, \\ -\csc(k\ell_{vw}) & \text{if } \; w \sim v, \\ 0 & \text{otherwise.} \end{cases} \tag{3.4}$$

Very often, $L(k)$ is moderately large, e.g., $|V| \approx 10^2$-10^4. Fortunately, it tends to be sparse but also unstructured. Two popular types of solution methods of NEPs are [94]:

1. Contour integral methods: these exploit Cauchy's residue theorem by calculating contour integrals around the poles of the resolvent L^{-1} (eigenvalues of L). [95, 96]

2. Newton-type methods: these iteratively solve for the roots of some function which the eigenvalues must satisfy, e.g. $\det L(k) = 0$, and solve (possibly simultaneously) for the corresponding eigenvectors [94].

In the following, we discuss several variants and accelerations of Newton-type methods. In particular, we develop a statistical trace-estimation algorithm that does not require computing the complete matrix inverse, the main bottleneck for (e.g.), $|V| \approx 10^5$ and beyond. We also discuss singular-value decomposition methods. We deploy the methods discussed in this chapter everywhere throughout this thesis in calculating spectra of large metric graphs.

3.1 Newton-type methods

The obvious solution to finding the spectrum in eq. (3.3) is to solve

$$\det(L(k)) = 0, \tag{3.5}$$

which is akin to solving the characteristic polynomial in a linear EVP, e.g.,

$$\det(\Delta_N - \lambda_N I_N) = 0, \tag{3.6}$$

which is, formally, a very high degree polynomial in λ_N. Solving eq. (3.5) directly is next to impossible for the same reason as with a linear representation like eq. (3.6): in general, determinants are a terrible idea. While mathematically concise, a large determinant typically becomes *combinatorially large* as a function of the matrix size. Figure 3.1 demonstrates this fact with a simple experiment. The plot shows a histogram of $|\det(M)|$ of a 100×100 matrix filled with uniformly random integers $|n| \leq 10$ for $10,000$ independent samples. It is common for $|\det(M)|$ to have well over 100 decimal digits. The huge dynamic range is problematic for numerical precision but also becomes a problem for overflow and underflow with sizes not far beyond the example we show here. However, the example also begs the following question: if determinants are so awful, then doesn't the linear eigenvalue characteristic polynomial suffer from the same trouble? In part, the standard tools of numerical linear algebra developed over decades to avert disasters when solving linear eigenvalue problems. In contrast, tools for nonlinear eigenvalue problems are

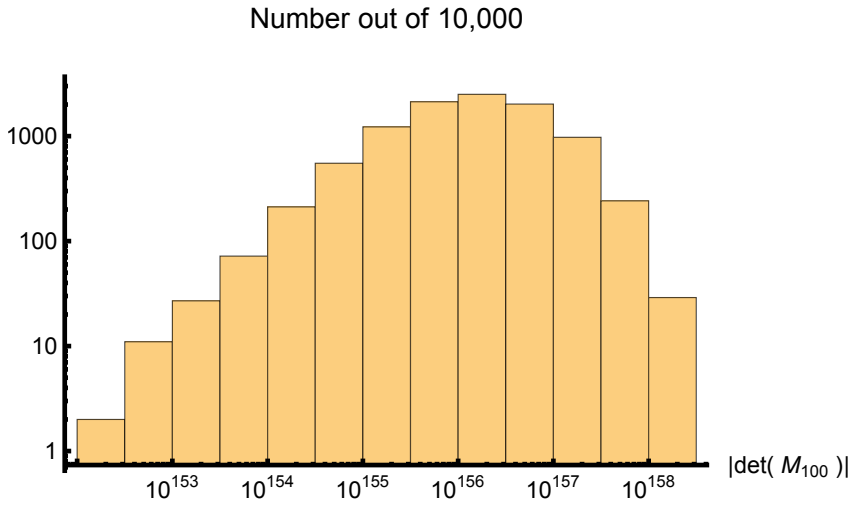

Figure 3.1: A histogram of 10^4 samples of the absolute value of the determinant for a 100×100 matrix with uniformly random integers $|n| \leq 10$.

much less well-developed. Given that nonlinear eigenvalue problems are the correct way to formulate many modern applications, numerical tools are rapidly catching up. However, given the vast diversity of ways for a function to be nonlinear, fully general-purpose solutions are unlikely beyond a handful of workhorse methods.

Foremost, Newton's method via the logarithm is especially suitable when encountering a vast dynamic range in a nonlinear problem. For $F(k) = \det(L(k))$, we can attempt

$$k_{n+1} = k_n - \frac{F(k_n)}{F'(k_n)}. \tag{3.7}$$

However, in the denominator,

$$\frac{F'(k)}{F(k)} \;=\; \frac{d}{dk}\log(\det(L(k))). \tag{3.8}$$

We might have tamed the determinant. There's one more trick to apply. For any matrix A,

$$\det(e^A) \;=\; e^{\mathrm{tr}(A)}, \tag{3.9}$$

which leads to Jacobi's formula for the logarithmic derivative,

$$\frac{F'(k)}{F(k)} \;=\; \frac{d}{dk}\mathrm{tr}\big(L(k)^{-1}L'(k)\big)\,. \tag{3.10}$$

We can easily compute the derivative, $L'(k)$ analytically from eq. (3.4). The iterative scheme is then

$$k_{n+1} \;=\; k_n - \frac{1}{\mathrm{tr}(L^{-1}(k_n)L'(k_n))}. \tag{3.11}$$

This is known as *Newton trace iteration*, and it is known to converge quadratically within a

neighbourhood of a semi-simple (algebraic = geometric multiplicity) eigenvalue k [97, 98]. The only serious numerical challenge remains solving the inverse, $L(k)^{-1}$, for which we can deploy sparse matrix algorithms. If L is an $m \times m$ matrix, then the problem now is one of solving for an $m \times m$ matrix X at each Newton step:

$$L(k_n)X \;=\; L'(k_n). \tag{3.12}$$

The main benefit is that the only crucial parameter is the initial guess. This makes this method particularly suitable for our purposes. The continuum limit provides good initial guesses which become better at higher densities when most needed. There are numerous variants of Newton-type methods based on different representative functions F. The eigenvectors are determined by solving for the nullvectors of $L(k)$ directly, or arise naturally from the particular iteration scheme, say in *Newton-QR iteration* [94]. A method that is particularly simple to implement uses the SVD of $L(k)$ [99]. At an eigenvalue k, we have $L(k)x = 0$ for nontrivial x, and so the minimum singular value $F = \sigma_m$ of L is 0. We therefore apply Newton's method to

$$\sigma_m(k) \;=\; 0. \tag{3.13}$$

We have

$$\sigma_m(k) \;=\; u_m^H(k)L(k)v_m(k) \tag{3.14}$$

for left and right singular vectors u_m and v_m corresponding to σ_m. For the derivative, [100] shows that $\sigma_m'(k) = u_m^H(k)L'(k)v_m(k)$. In Newton's method,

$$k_{n+1} \;=\; k_n - \frac{\sigma_m(k_n)}{u_m^H(k_n)F'(k_n)v_m(k_n)}. \tag{3.15}$$

[99, 100] show that local quadratic convergence is maintained for simple eigenvalues if we approximate u_m and v_m by inverse iteration at each step. They suggest calculating the decomposition of σ_m exactly at the first step, and performing inverse iteration steps simultaneously with the Newton steps to obtain subsequent u_m and v_m:

1. Start with a guess k_0. Calculate k_0, u_0, v_0.
2. Until convergence,
   (a) Calculate $k_{n+1} = k_n - \sigma_n/(u_n^T L'(k_n)v_n)$
   (b) Set $v_{n+1} = x_{n+1}/\|x_{n+1}\|$ where $L(k_{n+1})x_{n+1} = u_n$
   (c) Set $u_{n+1} = y_{n+1}/\|y_{n+1}\|$ where $L(k_{n+1})y_{n+1} = v_{n+1}$
   (d) Set $k_{n+1} = u_{n+1}^T L(k_n)v_{n+1}$

We now present our variant of a Newton-type method.

3.2 Stochastic Newton-trace iteration

As is, eq. (3.11) requires a significant calculation eq. (3.12) per step. However, we only need the *trace* of X. The method we devise reduces the computational complexity by

estimating the trace at every step.

3.2.1 Stochastic trace estimation

Trace estimation is a stochastic, matrix-free method which estimates the trace of some $n \times n$ matrix A by averaging over quadratic forms $u^T Au$. It is based on two ideas. The first is that if u is some random vector with mean vector $\mu = 0$ and covariance matrix $\Sigma = I$, then by the identity for the expectation of the quadratic form $u^T Au$ in u

$$\mathbb{E}\left[u^T Au\right] \;=\; \mathrm{tr}(A\Sigma) + \mu^T A\mu \;=\; \mathrm{tr}(A)\,. \tag{3.16}$$

Hutchinson trace estimation uses *Rademacher* random vectors (uniform random vectors of ± 1) and Gaussian trace estimation uses standard Gaussian random vectors. The second idea is that Au can be easier to compute than A is to construct. In our case eq. (3.11), we have $A = L^{-1}(k_n)L'(k_n)$. Then calculating $u^T L^{-1}(k_n)L'(k_n)u$ only requires one full solve in $u^T L^{-1}(k_n)$:

$$L^T(k_n)x \;=\; u. \tag{3.17}$$

We then have $\mathbb{E}\left[x^T L'(k_n)u\right] = \mathrm{tr}(L^{-1}(k_n)L'(k_n))$.

The first questions are then: what is the error, and how many u's should we average over? That is, when and how is the following a good approximation

$$\mathrm{tr}(A) \;\approx\; \mathrm{tr}(A)_m \;:=\; \frac{1}{m}\sum_{i=1}^{m} u_m^T A u_m \tag{3.18}$$

for i.i.d. random vectors u_m? We know, for example, that we have exactly $\sum_{i=1}^{n} e_i^T A e_i = \mathrm{tr}(A)$. But here, you need *all* n vectors–in the above example, this would correspond to fully inverting L. Why and how it is that in practice, $m \ll n$ gives high accuracy is an active area of research. Trace estimation was invented in [101, 102], using Gaussian and uniform random vectors. It was shown that, for example, the Hutchinson trace estimator for positive semidefinite matrices has variance bounded by [103]

$$\mathrm{Var}\left[u^T Au\right] \;\leq\; \mathrm{tr}\big(A^2\big) - \frac{\mathrm{tr}(A)^2}{n}. \tag{3.19}$$

For $\mathrm{tr}(A)_m$, most results focus on positive definite matrices A. In this case, Hutchinson estimation requires $O\left(\log(1/\delta)/\varepsilon^2\right)$ estimations (queries) to achieve a $(1 \pm \varepsilon)\mathrm{tr}(A)$ approximation with probability $1 - \delta$ [104]. The Hutch++ algorithm, which calculates the $O\left(1/\varepsilon\right)$ largest magnitude eigenvalues exactly, and (Hutchinson) estimates the rest of the trace, reduces the number of queries from $O\left(1/\varepsilon^2\right)$ to the optimal $O\left(1/\varepsilon\right)$ with constant probability. Generally, estimation falls into two categories: non-adaptive (NA) and adaptive (A) or dynamic. Estimation is adaptive if queries depend on previous u's and Au's, and nonadaptive otherwise. Both have advantages. Namely, NA estimation is highly parallelizable and is used as a subroutine for estimating matrix norms in many low-memory streaming algorithms [105]. Estimation applications are in [96, 106, 107]. Examples include estimations of the density of states, eigenvalue counts and numerical ranks, and log-likelihoods. Log-determinants and log-likelihood for Bayesian and determinan-

tal point process methods: $A = \log(B)$ is $\mathcal{O}(N^3)$ while $Ax = \log(B)x$ is approximately $\mathcal{O}(N^2)$ with Lanczos Triangles counts in large graphs: if B is the adjacency matrix, $\text{tr}(B^3) = 6 \times \#\text{triangles}$. $A = B^3$ is $O(N^3)$, while $Ax = B(B(Bx))$ is $O(N^2)$. More abstract applications include matrix inverses, Schatten p-norms and the Estrada index. Better estimates of the variance and theory for general indefinite matrices are in [104]. Finding the first few eigenvalues gives a better approximation [108, 109]. Analysis for trace estimation generally focuses on positive definite matrices, bounding relative errors between $\text{tr}_m(A)$ and $\text{tr}(A)$. This can't work for indefinite A where we can have $\text{tr}(A) = 0$. The only work on indefinite matrices is by Cortinovis, Persson, et al. They first provide a bound for ordinary Hutchinson estimation [104]. For indefinite matrices, Hutchinson trace estimation is bounded as follows

$$\mathbb{P}\left(|\text{tr}_m(A) - \text{tr}(A)| \geq \epsilon\right) \;\leq\; 2e^{-\frac{m\epsilon^2}{8\|A-\text{diag}(A)\|_F^2 + 8\epsilon\|A-\text{diag}(A)\|_2^2}} \tag{3.20}$$

The vertices of the graphs we study are only connected to others in some local neighbourhood. This means that L is generally very sparse. For example, for a periodic square graph, L is filled on the order of $|V|^{-1}\%$. We use stochastic Newton-trace estimation throughout this thesis on a wide range of graph structures $L(k)$ and up to 10^6 vertices. We have found it to locally converge quadratically for semisimple eigenvalues over a range of sample sizes m. Up to 10^6 vertices we have found $m = 50$ to be sufficient to obtain quadratic convergence. Estimating the trace has allowed all calculations to be done in real time on a local machine where previously calculations had to be performed on HPC clusters. Our custom algorithm for calculating eigenvalues is as follows:

1. Start with a guess k_0. Pick $m > 0$ based on eq. (3.20) (or for $|V| < 10^6$, we find for our NEP no larger than $m = 50$ is required).

2. Until convergence,

   (a) Solve $L^T(k_n)X = U$ for U having m columns of independent Rademacher vectors.

   (b) Set $T = X^T L'(k_n)U/m$

   (c) Set $k_{n+1} \to k_n - 1/T$

All code for this thesis is in [110].

Chapter 4

Introductory examples

This chapter presents a series of simple initial examples of our continuum model. The purpose is to elaborate on the previous chapter's observations, and to give intuition into the nature of the continuum limit. The general setup involves picking a particular graph G which exhibits some new behaviour(s), and a suitable embedding space M. The examples we choose are of periodic graphs. A periodic graph is constructed by connecting translated copies of a "basis" subgraph. A simple example is the periodic square graph in the planar torus (figure 4.7). The basis subgraph is just a single vertex, translated by $\ell(me_x + ne_y)$ for $m, n \in [0, N-1]$ and some global edge length $\ell = 1/N$. Connections are between subgraphs within a distance 1 from each other. A more complicated example is that of the truncated trihexagonal graph, whose basis is two connected dodecagons, translated copies of which are connected as in figure 6.5. The local graph periodicity enables solutions as plane waves. The metric graph problem then has explicit solutions both from the vertex NEP standpoint, and the continuum limiting standpoint. We present examples in embedding spaces of one, two, and three dimensions.

4.1 Periodic metric graphs

In this chapter, we present a series of graphs with periodic structure. To do this, we first introduce several notions from the literature. A lattice Λ in $\mathbb{R}^n$ is a discrete subgroup of $\mathbb{R}^n$ of order n [111]. It is generated by a set of basis vectors $e_1, \ldots, e_n$ of $\mathbb{R}^n$ so that:

$$\Lambda = \left\{ \sum_i m_i e_i \mid m_i \in \mathbb{Z} \right\}. \tag{4.1}$$

In this context, the basis vectors are called *lattice* vectors. A simple example of a lattice in $\mathbb{R}^2$ is the square lattice generated by the standard basis vectors $e_1 = (1, 0)$, $e_2 = (0, 1)$ (illustrated in figure 4.1a)). Another example is the hexagonal lattice (figure 4.1b)) generated by $e_1 = (\cos(\pi/6), -\sin(\pi/6))$, $e_2 = (\cos(\pi/6), \sin(\pi/6))$. Lattice vectors do not uniquely determine a given lattice. For example, the vectors $e_1 = (1, 0)$, $e_2 = (1, 1)$ also generate the square lattice. The defining feature is that integer linear combinations reproduce the lattice exactly, as in eq. (4.1). For example, $e_1 = (1, 0)$, $e_2 = (0, 2)$ generates a rectangular lattice, not the square lattice. Lattices are characterised by their associated symmetry groups. These are determined by the lengths of and angles between the lattice

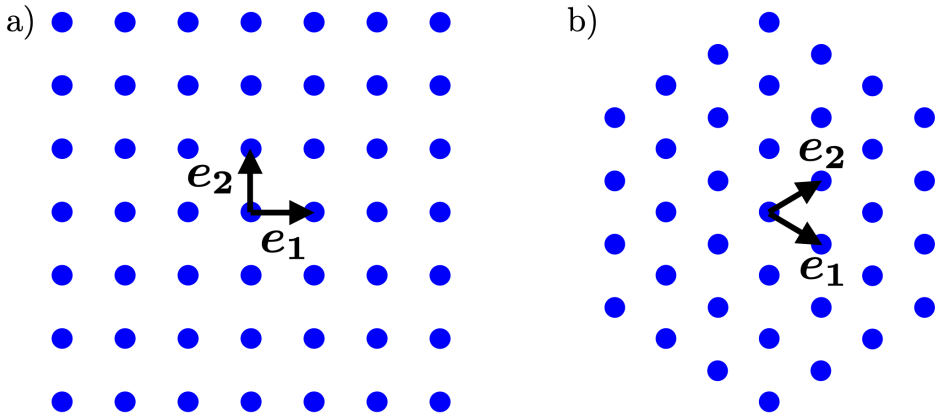

Figure 4.1: Examples of lattices in $\mathbb{R}^2$. The square lattice a) has lattice vectors $e_1 = (1, 0)$, $e_2 = (0, 1)$, and the hexagonal lattice b) has lattice vectors $e_1 = (\cos(\pi/6), -\sin(\pi/6))$, $e_2 = (\cos(\pi/6), \sin(\pi/6))$. In both cases, the subsets shown represent all combinations of the lattice vectors for $|m_i| \leq 3$ in eq. (4.1).

vectors. In crystallography, lattices in $\mathbb{R}^3$ are known as Bravais lattices for the physicist Auguste Bravais who classified the 14 nonisomorphic symmetry groups generated by any triple of basis vectors (there are 5 in the plane).

Lattices implicitly translate a *basis* vertex $v = (0, 0)$. We can couple a lattice to an arbitrary set of basis vertices to construct more complicated structures. Such an object has various names: Bravais lattice with a basis, crystal, crystal(line) structure [112], lattice with motif [113, 114], multilattice [115–117]. If $\{v_1, v_2, \ldots, v_N\}$ is a basis of N vertices, then the corresponding multilattice generated by lattice basis vectors e_j is given by

$$\Lambda = \bigcup_i \left\{ v_i + \sum_j m_j e_j \mid m_j \in \mathbb{Z} \right\}. \tag{4.2}$$

An example is the union of the green and red vertices in the hexagonal multilattice in figure 4.2. In this case, the basis consists of one green vertex v_1, one red vertex v_2, and the lattice vectors e_1, e_2 from figure 4.1b).

Together, a vertex basis and a set of lattice vectors provide a systematic way of representing periodic structures. However, the primary emphasis is on the vertices, contrary to metric graphs in which the primary emphasis is on the edges. For instance, the square lattice from figure 4.1a) produces different metric graphs depending on our choice of connections. Figure 4.3 shows three examples which we will investigate later. General tilings provide even more flexibility in constructing periodic structures. In fact, the classic reference [118] defines a planar tiling as a countable family of closed topological discs $\mathcal{T} = \{T_0, T_1, T_2, \ldots\}$ whose union is the plane, and whose interiors are pairwise disjoint. Examples are illustrated in figure 4.5. However, tilings include surplus higher-dimensional objects (faces, volumes, etc). We require the graph (or one dimensional) restrictions of tilings.

In total, there does not appear to be a direct reference to our objects of interest. Although we will employ much of the terminology above, we will refer to (metric) graphs

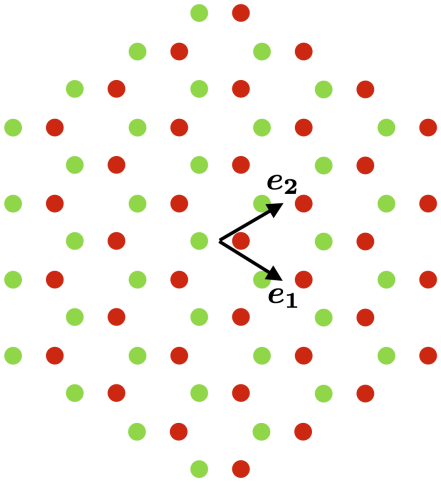

Figure 4.2: Hexagonal multilattice constructed from two hexagonal lattices as in figure 4.1b).

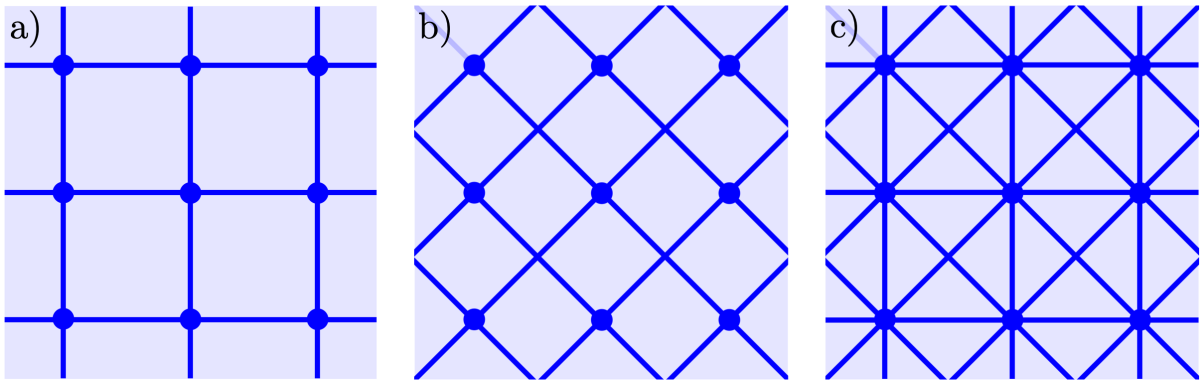

Figure 4.3: Some ways of connecting the square lattice (figure 4.1a)) to form a metric graph. We show a) the (square) cardinal connections, b) ordinal connections, and c) both.

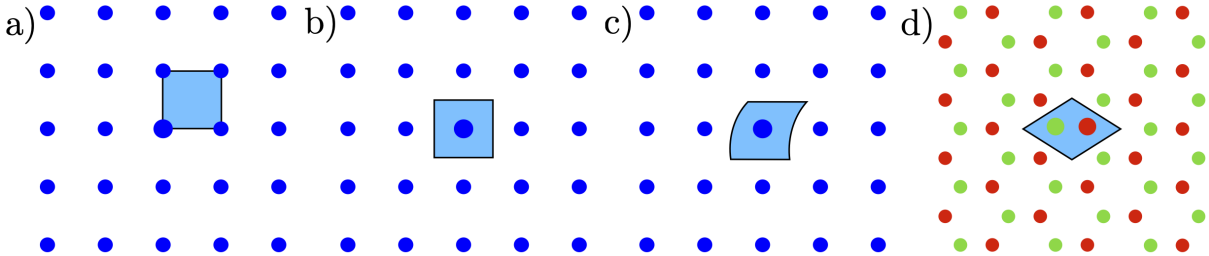

Figure 4.4: Examples of primitive cell areas for the square lattice and hexagonal multilattice. For the square lattice, each cell corresponds to one vertex (the (enlarged) central vertex in this case). a) and c) are arbitrarily shaped and positioned, and b) is the Voronoi cell (containing all points closest to the central vertex. d) is the Voronoi cell for the central basis of green/red vertices.

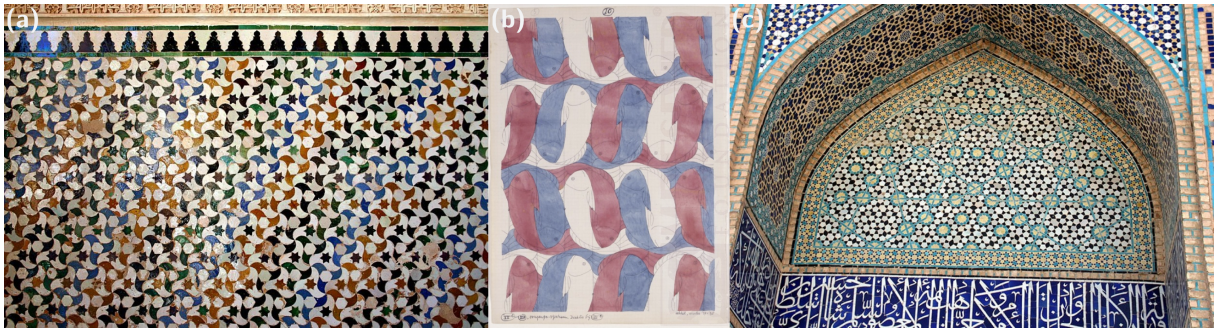

Figure 4.5: Some tilings of the plane. (a) An interior wall of the Alhambra Palace and fortress complex in Granada, Spain [119]. The decorations of this palace inspired (b) M. C. Escher [120]. (c) A Penrose tiling of the Darb-i Imam shrine in Isfahan, Iran from 1453 [121].

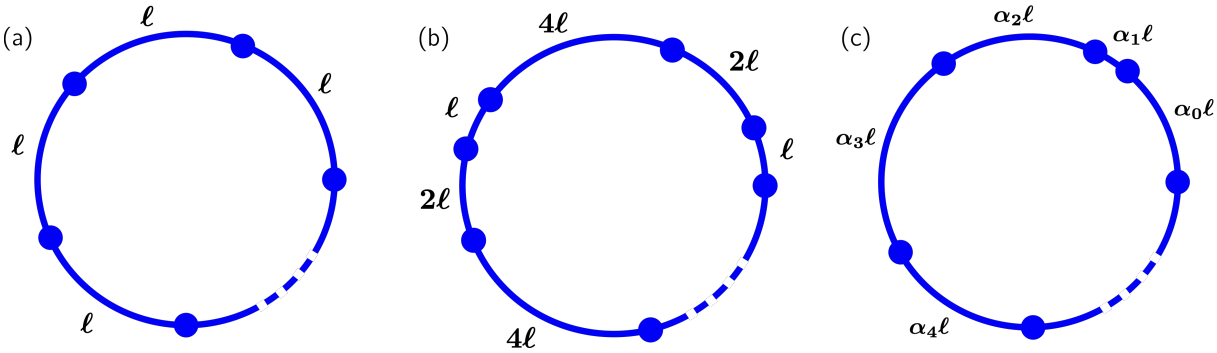

Figure 4.6: Examples of one-dimensional toroidal graphs of total length 1. (a) A uniform graph with constant spacing ℓ. (b) A periodic graph with repeated edge lengths $\ell, 2\ell, 4\ell$. (c) A uniformly random graph derived from (a) by rescaling each edge length with a uniformly random variable α_i.

constructed from lattices, multilattices and periodic tilings as *periodic (metric) graphs*.

4.2 In one dimension

In one dimension we should see no metric graph effects. This is because at degree two vertices, Kirchhoff's law is equivalent to standard differentiability. As a result, if a given graph G is embedded in some one-dimensional smooth manifold M, then the graph NEP constructed from the set of problems $\partial_x^2 f_i = -k^2 f_i$ is equivalent to the full problem $f''(x) = -k^2 f(x)$ on M. We verify this in the following examples.

4.2.1 1-Torus

Figure 4.6 illustrates a series of one-dimensional toroidal metric graphs. Each is normalized to have a total length of 1, and each vertex is connected to exactly two others by multiples α of some characteristic length ℓ. In the uniform case (figure 4.6a), each $\alpha = 1$. In the non-uniform case (figure 4.6b), α cycles through $\{1, 2, 4\}$. Finally, in figure 4.6c, the α's are sampled from $\mathcal{U}[0, 1]$–the uniform distribution of real numbers in $[0, 1]$. In

each case, any given vertex v is connected to vertices w_- and w_+ at distances of $\ell_- = \alpha_-\ell$ and $\ell_+ = \alpha_+\ell$. The vertex condition eq. (2.16) is

$$(\cot(k\ell_-) + \cot(k\ell_+))\, f(v) - (\csc(k\ell_-)\, f(v-\ell_-) + \csc(k\ell_+)\, f(v+\ell_+)) \;=\; 0. \tag{4.3}$$

In one dimension, we can determine the continuum limit from the vertex condition directly. We see that to leading order,

$$f''(x) \;=\; -k^2 f(x), \tag{4.4}$$

as expected. From the PDE standpoint, the edge tensor is

$$R(v) \;=\; \ell_-(-e)\otimes(-e) + \ell_+(+e)\otimes(+e) \;=\; (\ell_- + \ell_+)I_1. \tag{4.5}$$
$$\operatorname{tr}(R(v)) \;=\; \ell_- + \ell_+. \tag{4.6}$$

For the vertex density, we choose the cell area of a given vertex to be the average of the adjacent edge lengths: $\mathcal{A}_v = (\ell_- + \ell_+)/2$. Then as usual, $\mu(v) = \frac{1}{\mathcal{A}_v}$. We then have

$$\mu(v)R(v) \;=\; 2I_1 \tag{4.7}$$

and the PDE simplifies to eq. (4.4). Therefore, to leading order as $\ell \to 0$, the continuum limit is equivalent to the NEP, which we know already reduces to eq. (4.4) exactly. Furthermore, the nth order continuum equation is of the form

$$\sum_{i=1-\mathrm{Mod}(n,2)}^{\lfloor n/2\rfloor} c_{n,i}(f^{(i+2)}(x) + k^2 f^{(i)}(x)) \;=\; 0. \tag{4.8}$$

for constants $c_{n,i}$ and ith derivatives $f^{(i)}(x)$ of f. Therefore, assuming the leading order condition is satisfied, the continuum approximation is also exact.

It is worth noting that, particularly in the random case c), neighbour-to-neighbour fluctuations of $\mathcal{O}(\ell^{-d}) = \mathcal{O}(\ell^{-1})$ in μ balance fluctuations of $\mathcal{O}(\ell)$ in R. This is not in general the case in higher dimensions d. For such fluctuations, we homogenize the R tensor in chapters 6 and 7. In addition, $\mu R/\operatorname{tr}(\mu R) = I_1$ (the identity in $\mathbb{R}$) because we are in one dimension. As we will see, for homogeneous and isotropic μR, this generalises to $\frac{1}{d}I_d$, an interesting property of such metric graphs.

4.3 In two dimensions

In the following, we present a series of two-dimensional periodic graphs illustrating various features of the continuum limit. In each case, we present the graph characteristics and construction method, the explicit solutions of the NEP and PDE, and a comparison of the two solutions for increasing graph densities.

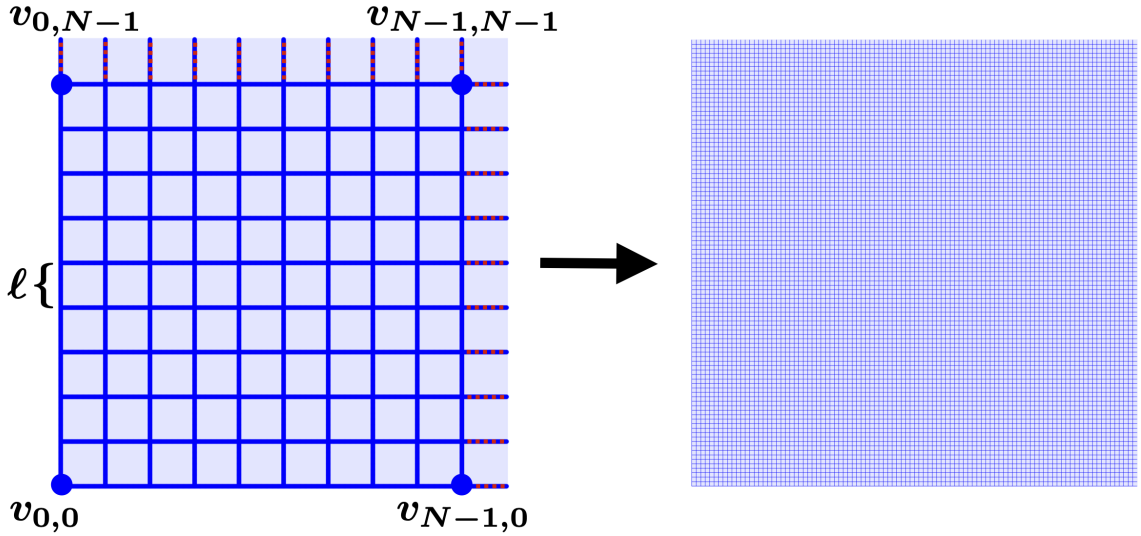

Figure 4.7: Illustration of the continuum limiting procedure for the periodic square graph filling in the flat torus $\mathbb{T}^2$. We fill in $\mathbb{T}^2$ by increasing the number N of vertices both in the horizontal and vertical directions. For the 10×10 graph (left), periodic/wrapped edges are dashed red. The length of each edge is given by the lattice spacing $\ell = \frac{1}{N}$.

4.3.1 Periodic square graph in the square flat torus

In this first setup, we consider the periodic square graph filling in the flat torus $\mathbb{T}^2 = \mathbb{R}^2 \backslash \mathbb{Z}^2$, as illustrated in figure 4.7. The periodic square graph is constructed from a finite, $N \times N$ square lattice, with lattice spacing $\ell = 1/N$. Vertices are connected to those within a distance ℓ–that is, in the horizontal and vertical directions. We index vertices by their number along each direction so that, for example, the bottom left and top right vertices have indices $(0, 0)$ and $(N-1, N-1)$, respectively. A vertex with index 0 in one dimension is connected to the vertex with index $N-1$ in the same dimension, and vice versa. For example, the vertex $(0, 0)$ is connected to vertices $(1, 0), (0, 1), (N-1, 0)$ and $(0, N-1)$. We analyse the continuum limit as $N \to \infty$.

Graph problem The periodic square graph in the 2-torus admits plane wave solutions of the NEP given by

$$f(v) \;=\; Ae^{i\kappa \cdot v} + \text{c.c.} \tag{4.9}$$

where the vertex coordinates are expressed as $v = ae_1 + be_2$ for integers $0 \leq a, b \leq N-1$ and lattice vectors

$$e_1 \;=\; \ell e_x, \quad e_2 \;=\; \ell e_y. \tag{4.10}$$

The wave vector $\kappa = q_1 \tilde{e}_1 + q_2 \tilde{e}_2$ is expressed in the dual basis given by the orthogonality relation

$$e_i \cdot \tilde{e}_j \;=\; \delta_{ij}. \tag{4.11}$$

Therefore

$$\tilde{e}_1 \;=\; \frac{1}{\ell}e_x, \quad \tilde{e}_2 \;=\; \frac{1}{\ell}e_y. \tag{4.12}$$

The wave vector components are determined by the global toroidal conditions

$$e^{i\kappa\cdot(v+Ne_1)} \;=\; e^{i\kappa\cdot v}, \quad e^{i\kappa\cdot(v+Ne_2)} \;=\; e^{i\kappa\cdot v}. \tag{4.13}$$

Therefore,

$$q_1 \;=\; \frac{2\pi m}{N}, \quad q_2 \;=\; \frac{2\pi n}{N}, \quad 0 \le m, n \le N-1. \tag{4.14}$$

Given that $\ell = 1/N$, we define $q_1 = \kappa_1\ell$, $q_2 = \kappa_2\ell$ for $\kappa_1 = 2\pi m$, $\kappa_2 = 2\pi n$. The vertex condition eq. (2.16) at v is then

$$4\cot(k\ell)\,e^{i\kappa\cdot v} \;=\; \csc(k\ell)\left(e^{i\kappa\cdot(v+e_1)} + e^{i\kappa\cdot(v-e_1)} + e^{i\kappa\cdot(v+e_2)} + e^{i\kappa\cdot(v-e_2)}\right) \tag{4.15}$$

$$\cos(k\ell) \;=\; \frac{1}{2}\left(\cos(\kappa_1\ell) + \cos(\kappa_2\ell)\right). \tag{4.16}$$

Explicitly, the eigenvalue parameters k are then given by

$$k \;=\; \frac{1}{\ell}\left(\arccos\left(\frac{1}{2}\left(\cos(2\pi m\ell) + \cos(2\pi n\ell)\right)\right) + 2\pi c\right), \tag{4.17}$$

for $c \in \mathbb{N}$. This relation is discussed below in the comparison of spectral densities. Before looking at the continuum limiting PDE directly, we see that to leading order, eq. 4.16 is

$$k^2 \;=\; \frac{1}{2}\kappa\cdot\kappa + \mathcal{O}\big(\ell^2\big) \;=\; \frac{1}{2}((2\pi m)^2 + (2\pi n)^2) + \mathcal{O}\big(\ell^2\big) \tag{4.18}$$

This is the relation we expect from the ordinary two-dimensional Laplace operator but with an extra factor of $1/2$. This is explained in the derivation of the continuum limit.

Continuum limit. The vertex density is constant $\mu(v) = \mu$. We can approximate it with $1/\mathcal{A}_v$ where the cell area $\mathcal{A}_v$ is simply given by ℓ^2. The edge tensor R is also constant,

$$R(v) \;=\; \frac{1}{\ell}\left(e_1\otimes e_1 + (-e_1)\otimes(-e_1) + e_2\otimes e_2 + (-e_2)\otimes(-e_2)\right) \;=\; 2\ell I. \tag{4.19}$$

Together, we have $\mu(v)R(v) = \mu 2\ell I$. In total, the PDE simplifies to

$$\frac{1}{\mu 2\ell\,\mathrm{tr}(I)}\nabla\cdot(\mu 2\ell I\cdot\nabla f(x,y)) \;=\; -k^2 f(x,y) \tag{4.20}$$

$$\frac{1}{2}\left(\frac{\partial^2}{\partial x^2} + \frac{\partial^2}{\partial y^2}\right) f(x,y) \;=\; -k^2 f(x,y) \tag{4.21}$$

This is the standard eigenvalue equation for the 2-dimensional Laplace operator with periodic boundary conditions and a rescaled eigenvalue $-2k^2$. Its solution is given by

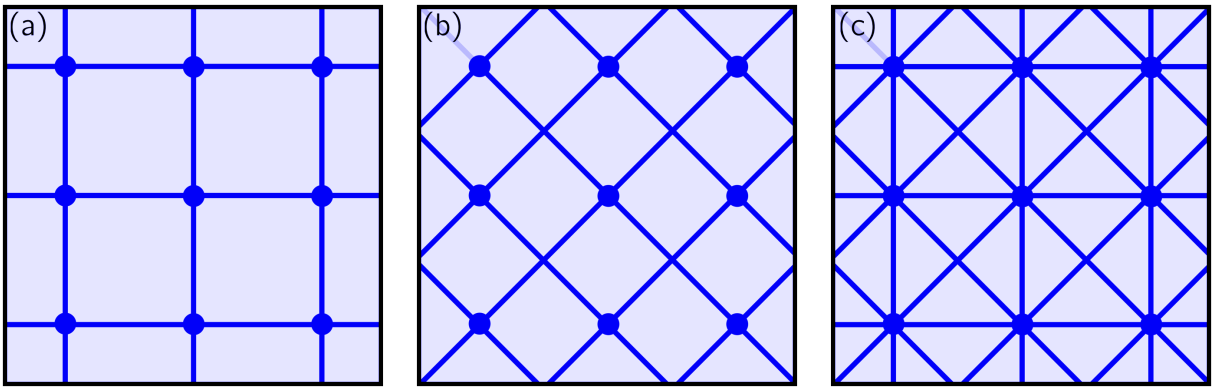

Figure 4.8: Three connection schemes for the square lattice. The standard cardinal connections in a), the ordinal connections in b), and the combined connections in c).

plane waves

$$f(x,y) \;=\; Ae^{i(\kappa_x x+\kappa_y y)} + \text{c.c.} \tag{4.22}$$

where $\kappa_x = 2\pi m$, $\kappa_y = 2\pi n$ for $m, n \in \mathbb{N}$ and setting $\kappa = (\kappa_x, \kappa_y)$,

$$k^2 \;=\; \frac{1}{2}\kappa\cdot\kappa \;=\; \frac{1}{2}\left((2\pi m)^2 + (2\pi n)^2\right). \tag{4.23}$$

This is the leading order term in eq. 4.18, confirming the continuum limit.

Eigenvalue rescaling by the embedding dimension d An interesting result is that in the graph and continuum dispersion relations eq. (4.18), eq. (4.23), the factor of $\frac{1}{2}$ comes from $1/\mathrm{tr}(I) = 1/d$ where d is the *dimension* of the embedding space. It is not just an artefact of the structure of the periodic square graph–corresponding to half of the degree of each vertex for example. Indeed, this $1/2$ factor comes from the vertex density being constant and the edge tensor being a multiple of the identity. For example, we could connect the vertices of the lattice in various different ways, as in figure 4.8. The dispersion relation for the ordinal connection scheme in b) is

$$4\cos\left(\sqrt{2}\ell k\right) \;=\; e^{i\ell(\kappa_1+\kappa_2)} + e^{i\ell(-\kappa_1+\kappa_2)} + e^{i\ell(-\kappa_1-\kappa_2)} + e^{i\ell(\kappa_1-\kappa_2)} \tag{4.24}$$

$$\cos\left(\sqrt{2}\ell k\right) \;=\; \cos(\kappa_1\ell)\cos(\kappa_2\ell)\,. \tag{4.25}$$

There is an interesting interpretation of this equation that shows intuitively why this also reduces to eq. (4.18) to leading order. This equation is the Pythagorean theorem on the sphere. Resetting $\ell = 1/N$, then on the sphere of radius N, this relation states that if arcs of length κ_1 and κ_2 meet at a right angle, k must be such that $\sqrt{2}k$ is the distance of the arc connecting their opposite endpoints:

$$\cos\left(\frac{\sqrt{2}k}{N}\right) \;=\; \cos\left(\frac{\kappa_1}{N}\right)\cos\left(\frac{\kappa_2}{N}\right). \tag{4.26}$$

For fixed κ_1, κ_2, as we increase the radius N of the sphere, the relation reduces to the standard Pythagorean theorem in flat space eq. (4.18). As a result, the dispersion relation for the combined connection scheme in c), which is simply the sum of the two dispersions relations, is to leading order eq. (4.18) as well.

In the continuum limit, the vertex densities are again constant, and the R tensors are constant and isotropic. For b),

$$\begin{aligned} R(v) &= \frac{1}{\sqrt{2}\ell}\left((e_1+e_2)\otimes(e_1+e_2)+(-e_1+e_2)\otimes(-e_1+e_2)\right. \\ &\left.+(-e_1-e_2)\otimes(-e_1-e_2)+(e_1-e_2)\otimes(e_1-e_2)\right) = 2\sqrt{2}\ell I \end{aligned} \tag{4.27}$$

and for c), we have $R(v) = 2\ell(1+\sqrt{2})I$. In both cases, we obtain the same continuum limit eq. (4.21).

Comparison between graph problem and continuum limit. We compare the edgewise graph Laplace operator to the continuum limiting PDE for increasing graph sizes (vertex densities). The questions of what to compare and how to do so first require some clarifications of terminology:

- The edgewise ODE has solutions given by *graph eigenvalues* $-k^2 \in \mathbb{R}$ and corresponding *graph eigenfunctions* $f \in \mathcal{D}_G \subset H^2(G)$.
- The nonlinear matrix eigenvalue problem (NEP) (eq. 2.17), equivalent to the edgewise ODE, has solutions given by *NEP eigenvalues* $k \in \mathbb{R}$ and corresponding *NEP eigenvectors* $f(V) \in \mathbb{R}^{|V|}$.
- The continuum limiting PDE has solutions given by *PDE* or *continuum eigenvalues* $-k^2 \in \mathbb{R}$ and corresponding *PDE* or *continuum eigenfunctions* $f \in \mathcal{D}_M \subset H^2(M)$.

We compare solutions (eigenvalues/eigenvectors) of the NEP and solutions (eigenvalues/eigenfunctions) of the PDE. In this first example, we explain and justify in detail the comparison methods used. First, we only look for positive NEP eigenvalues. This is because for each eigenvalue $-k^2$ of the edgewise ODE, the two eigenvalues k and $-k$ of the NEP correspond to the same eigenspace because L is an odd function of k. Indeed, L's entries (eq. (2.19)) are linear combinations of odd functions cot and csc of k. Therefore, if (k, f) is a solution of the NEP, then so is $(-k, f)$:

$$L(-k)f(V) = -L(k)f(V) = 0. \tag{4.28}$$

The examples in this chapter are on d-dimensional tori. We compare eigensolutions for the first 3^d eigensolutions. In this particular example, that is the 3×3 solutions $(m,n) \in \{0,1,2\}$ in eqs. 4.16 and 4.23. This ensures that we test a range of magnitudes and eigenspace structures. Define $\kappa_x(m) = 2\pi m$, $\kappa_y(n) = 2\pi n$. For $0 \le m, n \le 2$, the eigenspaces are spanned by the basis functions as follows

- If $(m,n) = (0,0)$: 1
- If $m = 0$: $\cos(\kappa_y(n)y)$, $\sin(\kappa_y(n)y)$
- If $n = 0$: $\cos(\kappa_x(m)x)$, $\sin(\kappa_x(m)x)$

$m \backslash n$	0	1	2
0	0	$2\pi^2$	$8\pi^2$
1	$2\pi^2$	$4\pi^2$	$10\pi^2$
2	$8\pi^2$	$10\pi^2$	$16\pi^2$

Table 4.1: Continuum limiting eigenvalues for the square lattice in the square flat torus. We show $k^2 = \left((2\pi m)^2 + (2\pi n)^2\right)/2$ for $(m,n) \in \{0,1,2\}^2$.

- Otherwise:
$$\cos(\kappa_x(m)x)\cos(\kappa_y(n)y)\ ,\ \cos(\kappa_x(m)x)\sin(\kappa_y(n)y)\ ,$$
$$\sin(\kappa_x(m)x)\cos(\kappa_y(n)y)\ ,\ \sin(\kappa_x(m)x)\sin(\kappa_y(n)y)$$

There are 6 individual continuum eigenvalues, displayed in table 4.1. The square roots of these values range over $[0, 12.5664...]$. In the NEP, we make a refined search over an extended range $k \in (0, 14]$. We find a discrete set of eigenvalues and eigenfunctions. For example, for a 24×24 periodic square graph, the first several NEP modes are illustrated in figure 4.9. The question then becomes how to compare edgewise modes and PDE modes. For this, we need a method for comparing graph functions and continuum functions and a method for comparing eigenspaces. For the first task, there are two options. The first is to restrict the PDE eigenfunctions to the edgewise eigenfunctions by simply restricting their domain from the torus to the graph. The second is to interpolate the edgewise eigenfunctions with functions on the torus. We choose the former option as it is simpler conceptually and logistically. To compare the graph and PDE eigenfunctions, we then rank graph eigenfunctions by how well they project onto graph restricted PDE eigenbases. The expectation is then that if the PDE eigenspace has dimension M, there will be an obvious set of M graph eigenfunctions. In doing so, we note that while we can at least say that the resulting restrictions are square-integrable over the graph, they do not belong to the same subspace $\mathcal{D}_G$ as the edgewise eigenfunctions. Indeed, while they are continuous at the vertices, they do not generally satisfy Kirchoff's law.

We illustrate this procedure for the $k^2 = 8\pi^2$ eigenvalue corresponding to $(m,n) \in \{(2,0),(0,2)\}$ for the 24×24 periodic square graph. This has corresponding PDE eigenfunctions

$$\left\{\cos\left(2\sqrt{2}\pi x\right), \sin\left(2\sqrt{2}\pi x\right), \cos\left(2\sqrt{2}\pi y\right), \sin\left(2\sqrt{2}\pi y\right)\right\}. \tag{4.29}$$

Then, for each function f in figure 4.9, we construct the projection $P_M(f)$ onto this eigenbasis

$$\begin{aligned} P_M(f) \ = \ & \left\langle \cos\left(2\sqrt{2}\pi x\right)\ ,\ f\right\rangle_G \cos\left(2\sqrt{2}\pi x\right) + \left\langle \sin\left(2\sqrt{2}\pi x\right)\ ,\ f\right\rangle_G \sin(2\pi x) \\ & + \left\langle \cos\left(2\sqrt{2}\pi y\right)\ ,\ f\right\rangle_G \cos\left(2\sqrt{2}\pi y\right) + \left\langle \sin\left(2\sqrt{2}\pi y\right)\ ,\ f\right\rangle_G \sin\left(2\sqrt{2}\pi y\right) \end{aligned} \tag{4.30}$$

and calculate the residuals $\|P_M(f) - f\|_G$. We find these to be of the order of 10^{-2} for the four functions corresponding to the NEP eigenvalue $8.8344\ldots$ (second row), and

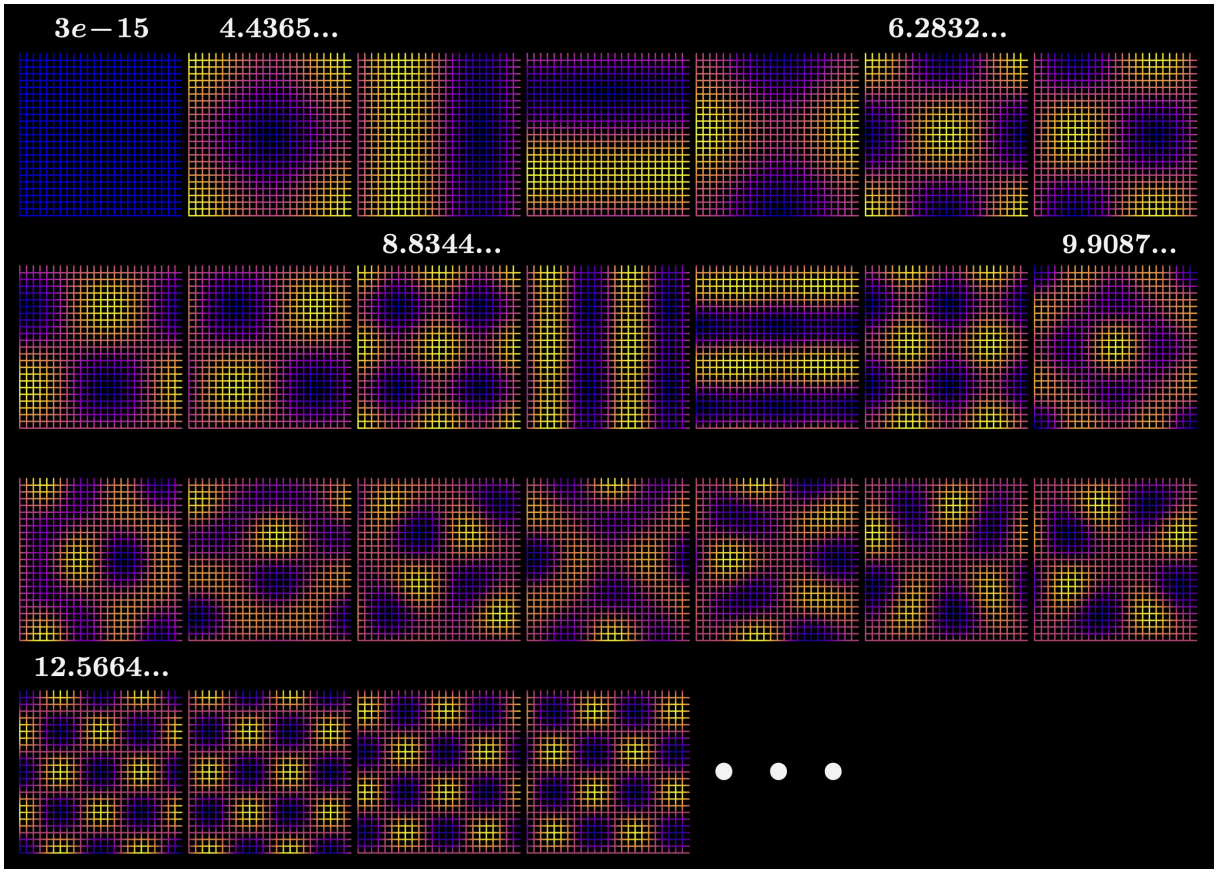

Figure 4.9: Numerical eigensolutions of the graph NEP for the square lattice in the flat square torus, for $0 < k < 13.5$. Eigenvalues are shown in increasing order (left $\rightarrow$ right and top $\rightarrow$ bottom), with corresponding eigenfunctions underneath. The number of eigenfunctions between eigenvalues corresponds to the eigenvalue's degeneracy.

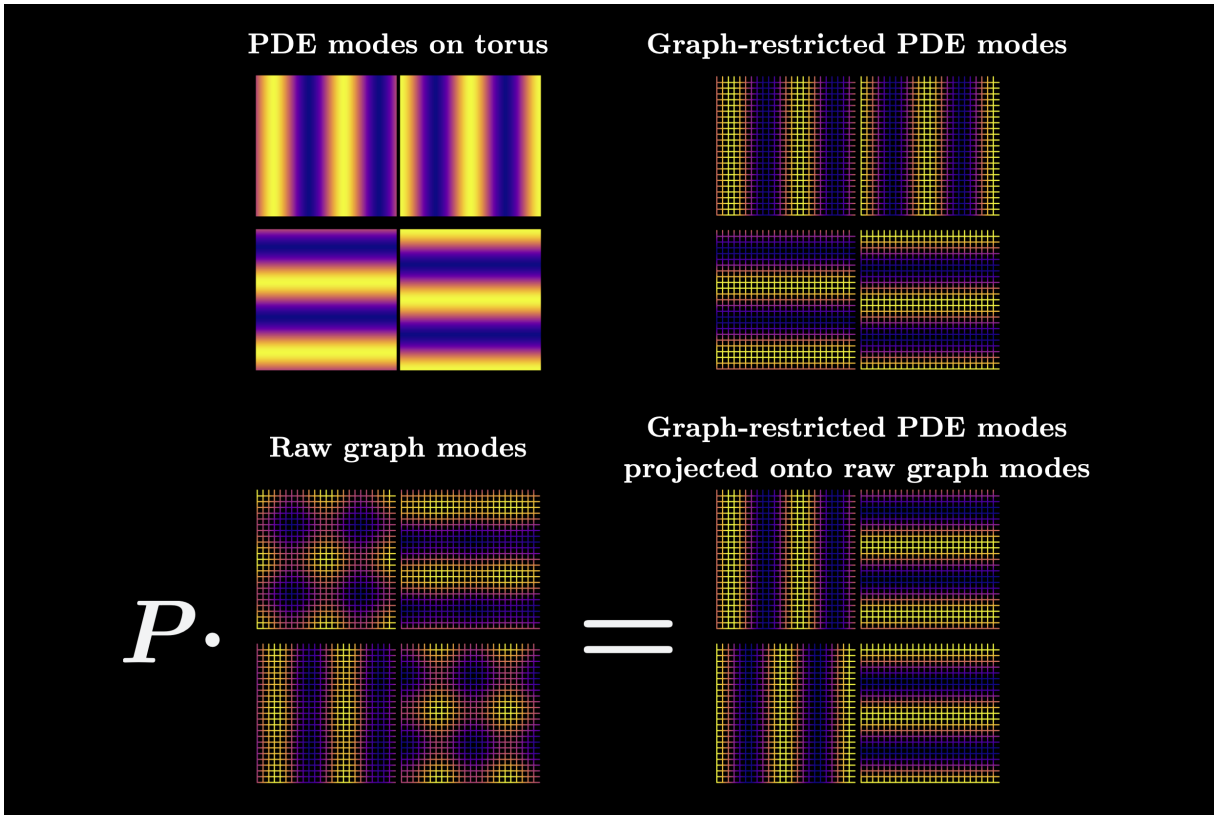

Figure 4.10: An illustration of mode comparison for the $(m, n) \in \{(2, 0), (0, 2)\}$ eigenspace. The four PDE eigenmodes from eq. (4.29) are in the top left. In the top right are those same modes restricted to the periodic square graph. The bottom equation is a visual illustration of eq. (4.31) for each $0 \leq i \leq 3$ The relative eigenfunction differences in figure 4.11 are the differences $\|P_G\left(f_i^M\right) - f_i^M\|_G$ between the respective functions in the top right and bottom right.

of the order of 10^{-1} for all others (note that all functions are normalised so that $0 \leq \|P_M(f) - f\|_G \leq 1$). Setting $k^M = 2\sqrt{2}\pi$ and $k^G = 8.8344\ldots$ for the manifold and graph eigenvalue parameters respectively, we now associate paired sets of eigensolutions $(k^M, \{f_i^M\}_{0\leq i\leq 3})$ and $(k^G, \{f_j^G\}_{0\leq j\leq 3})$. To visually and numerically compare the two, we construct the recognisable PDE eigenfunctions from the graph eigenfunctions:

$$P_G\left(f_i^M\right) \;=\; \sum_{j=0}^{3} \left\langle f_j^G \,,\, f_i^M \right\rangle_G f_j^G, \tag{4.31}$$

for each f_i^M in eq. (4.29). An illustration of this procedure is in figure 4.10. For the eigenfunctions, we calculate $\|P\left(f_i^M\right) - f_i^M\|_G$. For the eigenvalues, we calculate $|(k^G - k^M)/k^M|$. In figure 4.11, we present the convergence in these quantities for $(m, n) \in \{0, 1, 2\}^2$ for increasing graph densities. For degenerate eigenvalues, we take the mean eigenfunction residual $\|P\left(f_i^M\right) - f_i^M\|_G$. The convergence rates are $\mathcal{O}(|V|^{-1})$. Along a given axis, the edge length is inversely proportional to the number of vertices: $\ell = 1/N$. Therefore $\ell^2 = N^{-2} = |V|^{-1}$ and so the convergence rate is $\mathcal{O}(\ell^2)$ as expected. For $m = n$, the eigensolutions match the continuum eigensolutions exactly and independently of the

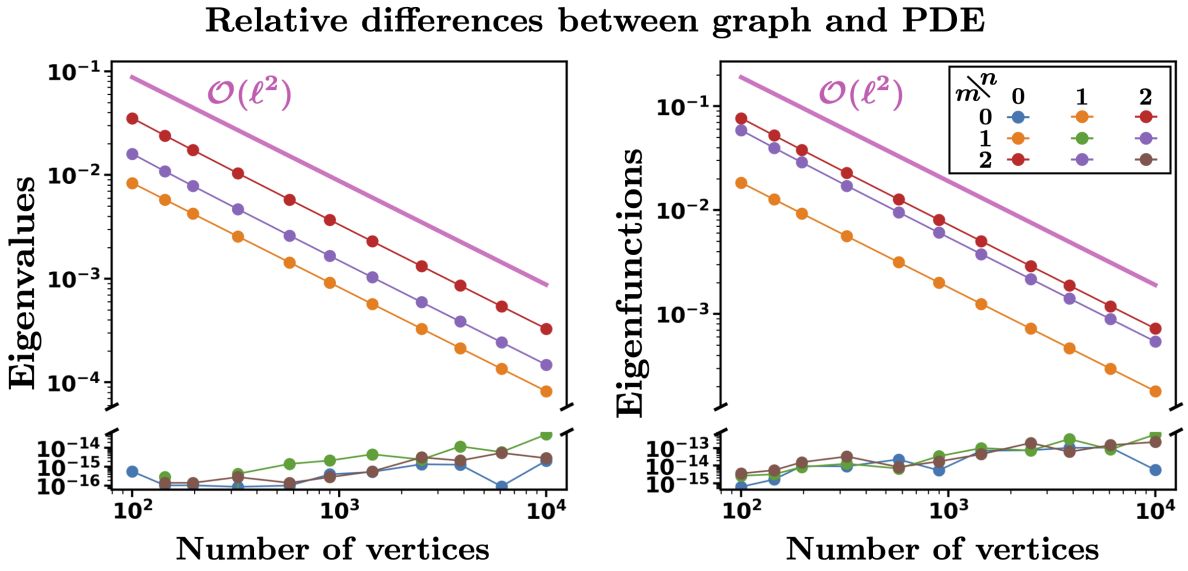

Figure 4.11: Convergence of NEP solutions to continuum limiting PDE solutions for periodic square graphs of increasing densities in the flat square torus.

vertex density. If we return to the explicit relation eq. (4.17), we notice that if $m = n$, then for $c = 0$, it simplifies to

$$k \;=\; 2\pi m, \tag{4.32}$$

which is indeed *independent* of ℓ. Another interesting note is that for $m \neq n$, we have

$$k \;=\; \sqrt{m^2+n^2}\left(\sqrt{2}\pi - \frac{\left(m^2-n^2\right)^2\pi^3}{6\sqrt{2(m^2+n^2)}}\ell^2 + \mathcal{O}\left(\ell^4\right)\right). \tag{4.33}$$

Higher-order terms are all even powers of ℓ whose coefficients up to and including $\mathcal{O}(\ell^6)$ are negative-valued functions of m, n. This explains why in the raw k data, we observed that eigenvalues converge to $\sqrt{m^2+n^2}\sqrt{2}\pi$ from below in figure 4.11. That is, we always saw $k^G < k^M$.

Additional considerations Finally, in practice, we find this eigenspace matching procedure to be reliable. However, certain exceptions may arise which require care. First, whether we have found all the NEP eigenvalues within a given interval is not always clear. As we will see for the random graphs, we may be looking for an 8-dimensional eigenspace split into eight different eigenspaces with eight different eigenvalues (this happens after adding a small amount of noise to the locations of the square lattice for $m = 1, n = 1$ for example). We need to ensure that our tolerances in the residual calculations don't allow for the case that if 7 of the eight eigenvalues are found, we sufficiently accurately project onto the seven corresponding edgewise eigenfunctions plus the next best. In addition, we need to ensure that the mapping between eigensolutions is bijective. That is, we want to ensure that a give graph mode is not double counted when projecting onto distinct PDE eigenspaces.

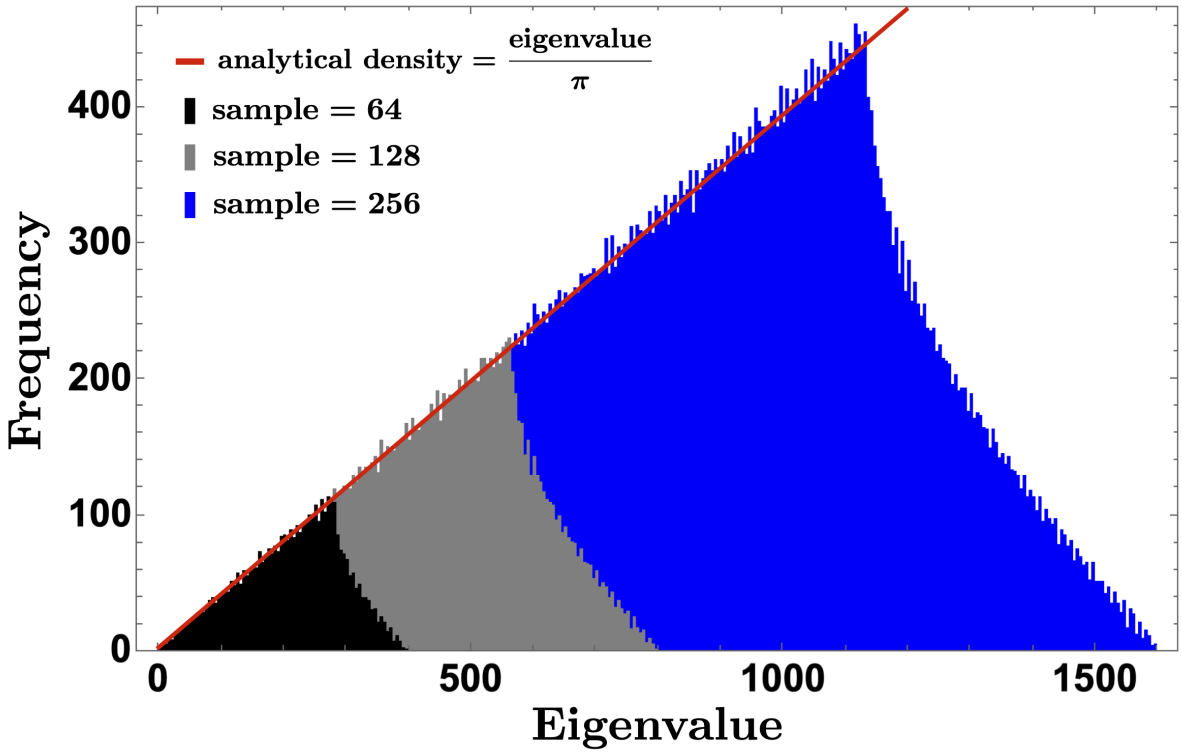

Figure 4.12: Convergence of spectral densities for the periodic square graph.

Convergence of spectral densities Figure 4.12 is a plot of the distribution of eigenvalues $k = \sqrt{2}\pi\sqrt{m^2+n^2}$. If $\{m,n\} \in [-M,M]^2$ is some finite sampling of the function k, then we see samplings of the distribution for $M = 64, 128, 256$ in figure 4.12. This counts the number of lattice points $\mathbb{Z}^2$ lying on the circle of radius $r = k/(\sqrt{2}\pi)$. If $N(r)$ is the number of lattice points (m,n) within a radius of r, then given that there is one lattice point per unit area on average, we have

$$N(r) \sim \pi r^2 \text{ as } r \to \infty. \tag{4.34}$$

This then means that for large r, we can make the approximation $dN \approx 2\pi r dr \approx \frac{k}{\pi} dk$. The cumulative distribution function $N(r)$ has corresponding distribution function k/π, a linear function which we can see (in red) in figure 4.12. In figure 4.13, we show the convergence of the graph spectral density to this continuum density for increasing graph densities. We see that they agree over increasing ranges of eigenvalues for increasing graph densities as expected. The shape of the graph spectral density is nonconstant but symmetric about $N\frac{\pi}{2}$. This is because in the $\frac{1}{\ell} \times \arccos$ relation, the mean argument of the arccosine is a symmetric, trigonometric distribution about 0.

4.3.2 Periodic rectangular graph in the square flat torus

We now consider a periodic graph constructed from a rectangular lattice. We place twice as many vertices in the horizontal direction and fill in the square flat torus T_2 with a rectangular lattice. We connect vertices in the orthogonal horizontal and vertical directions as in figure 4.14. This example illustrates how the graph problem relates to

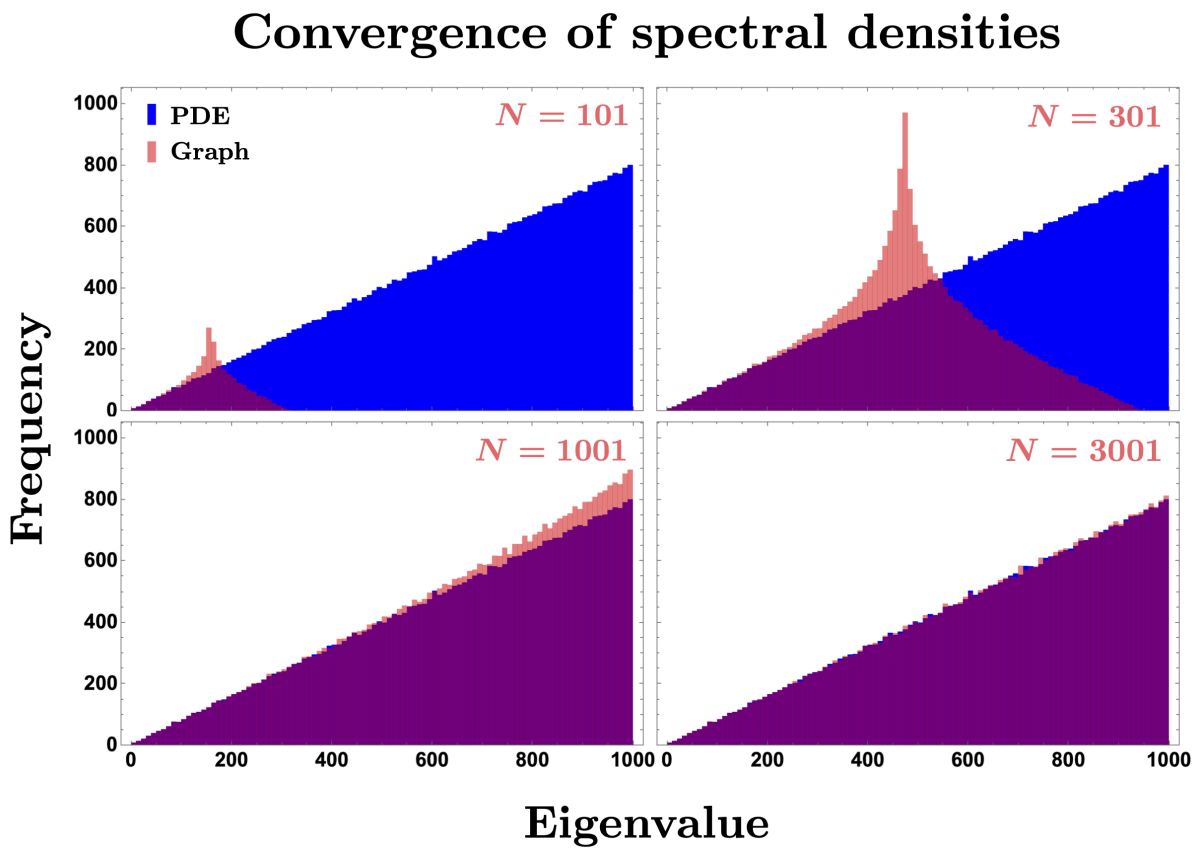

Figure 4.13: Convergence of spectral densities for the periodic square graph.

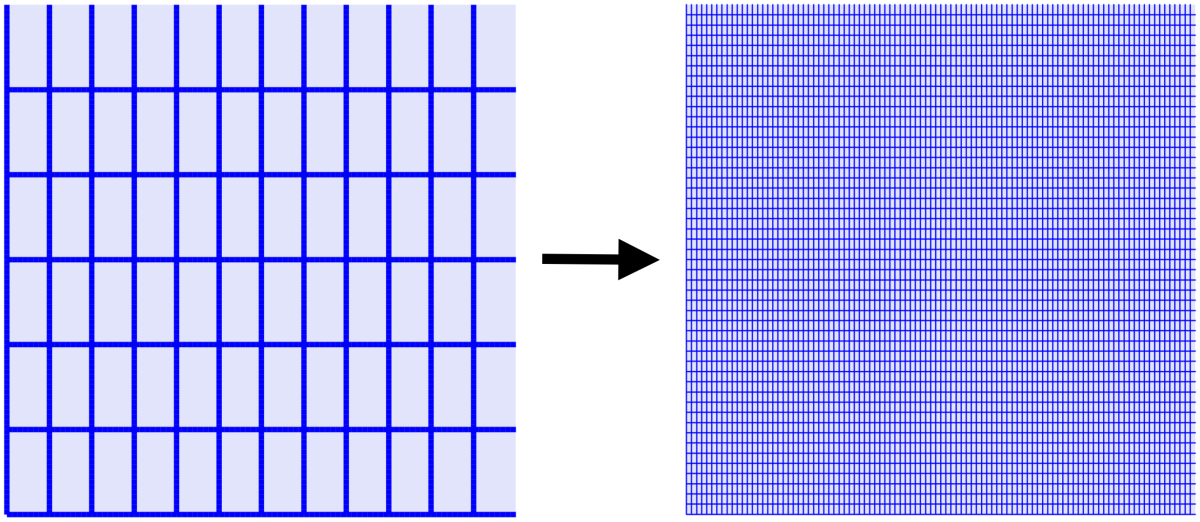

Figure 4.14: Illustration of the continuum limiting procedure for the periodic rectangular graph filling in the 1×1 square flat torus.

the continuum limit when there is a local anisotropy in the graph material. The graph has $2N$ vertices in the horizontal direction and N in the vertical direction for a total of $2N \times N$. The vertical edge length is $\ell = \frac{1}{N}$, and the horizontal edge length is $\frac{1}{2N} = \frac{\ell}{2}$.

Graph problem In this case, the lattice vectors are $e_1 = \frac{1}{2}\ell e_x$ and $e_2 = \ell e_y$. Consider plane wave solutions

$$f(v) \;=\; Ae^{i\kappa\cdot v} + \text{c.c.} \tag{4.35}$$

We express the wave vectors κ in the dual basis $a = q_1\tilde{e}_1 + q_2\tilde{e}_2$, where $\tilde{e}_1 = \frac{2}{\ell}e_x$, $\tilde{e}_2 = \frac{1}{\ell}e_y$. The periodic boundary conditions imply that

$$e^{i\kappa\cdot(v+2Ne_1)} \;=\; e^{i\kappa\cdot v}, \quad e^{i\kappa\cdot(v+Ne_2)} \;=\; e^{i\kappa\cdot v}. \tag{4.36}$$

Therefore

$$q_1 \;=\; \frac{\pi m}{N}, \quad q_2 \;=\; \frac{2\pi n}{N}, \quad 0 \le m, n \le N-1. \tag{4.37}$$

Setting $q_1 = \kappa_1\ell$, $q_2 = \kappa_2\ell$ for $\kappa_1 = \pi m$, $\kappa_2 = 2\pi n$, the vertex condition is

$$\begin{aligned} 2\left(\cot\left(\frac{k\ell}{2}\right) + \cot(k\ell)\right)e^{i\kappa\cdot v} \;&=\; \csc\left(\frac{k\ell}{2}\right)\left(e^{i\kappa\cdot(v+e_1)} + e^{i\kappa\cdot(v-e_1)}\right) \\ &\quad + \csc(k\ell)\left(e^{i\kappa\cdot(v+e_2)} + e^{i\kappa\cdot(v-e_2)}\right) \qquad (4.38) \\ \cot\left(\frac{k\ell}{2}\right) + \cot(k\ell) \;&=\; \csc\left(\frac{k\ell}{2}\right)\cos(\kappa_1\ell) + \csc(k\ell)\cos(\kappa_2\ell)\,. \qquad (4.39) \end{aligned}$$

$m \setminus n$	0	1	2
0	0	$\frac{8\pi^2}{3}$	$\frac{32\pi^2}{3}$
1	$\frac{4\pi^2}{3}$	$4\pi^2$	$12\pi^2$
2	$\frac{16\pi^2}{3}$	$8\pi^2$	$16\pi^2$
3	$12\pi^2$	X	X

Table 4.2: Continuum limiting eigenvalues for the rectangular lattice in the square flat torus. We show $k^2 = \frac{1}{3}(2\pi m)^2 + \frac{2}{3}(2\pi n)^2$ for $(m,n) \in \{0,1,2\}^2$. We include the $(3,0)$ eigenvalue because it coincides with the $(1,2)$ eigenvalue and both corresponding eigenfunctions are required to span their shared eigenspace.

To leading order, eq. (4.39) is

$$k^2 \;=\; \frac{1}{3}(2\kappa_1)^2 + \frac{2}{3}(\kappa_2)^2 + \mathcal{O}\big(\ell^2\big) \;=\; \frac{1}{3}(2\pi m)^2 + \frac{2}{3}(2\pi n)^2 + \mathcal{O}\big(\ell^2\big)\,. \tag{4.40}$$

This is confirmed in the derivation of the continuum limit.

Continuum limit In this case, we consider μ as still some constant. If vertical edges have length ℓ, then R is given by

$$R(v) \;=\; \frac{1}{2}\ell e_x \otimes e_x + \frac{1}{2}\ell(-e_x)\otimes(-e_x) + \ell e_y \otimes e_y + \ell(-e_y)\otimes(-e_y) \;=\; \ell\begin{pmatrix}1 & 0\\ 0 & 2\end{pmatrix}. \tag{4.41}$$

The continuum PDE then simplifies to

$$\left(\frac{1}{3}\frac{\partial^2}{\partial x^2} + \frac{2}{3}\frac{\partial^2}{\partial y^2}\right) f(x,y) \;=\; -k^2 f(x,y). \tag{4.42}$$

This again has solutions given by plane waves

$$f(x,y) \;=\; Ae^{i(\kappa_x x + \kappa_y y)} + \text{c.c.} \tag{4.43}$$

where $\kappa_x = 2\pi m$, $\kappa_y = 2\pi n$ for $m,n \in \mathbb{N}$ and

$$k^2 \;=\; \frac{1}{3}(2\pi m)^2 + \frac{2}{3}(2\pi n)^2\,. \tag{4.44}$$

Comparison between finite graph problem and continuum limit For comparison, we choose the eigenspaces corresponding to $(m,n) \in \{0,1,2\}^2$, as in table 4.2. This consists of 9 individual eigenvalues, with the $(1,2)$ eigenvalue coinciding with the $(3,0)$ eigenvalue. Define $\kappa_x(m) = 2\pi m$, $\kappa_y(n) = 2\pi n$. For $0 \le m,n \le 2$, the eigenspaces are

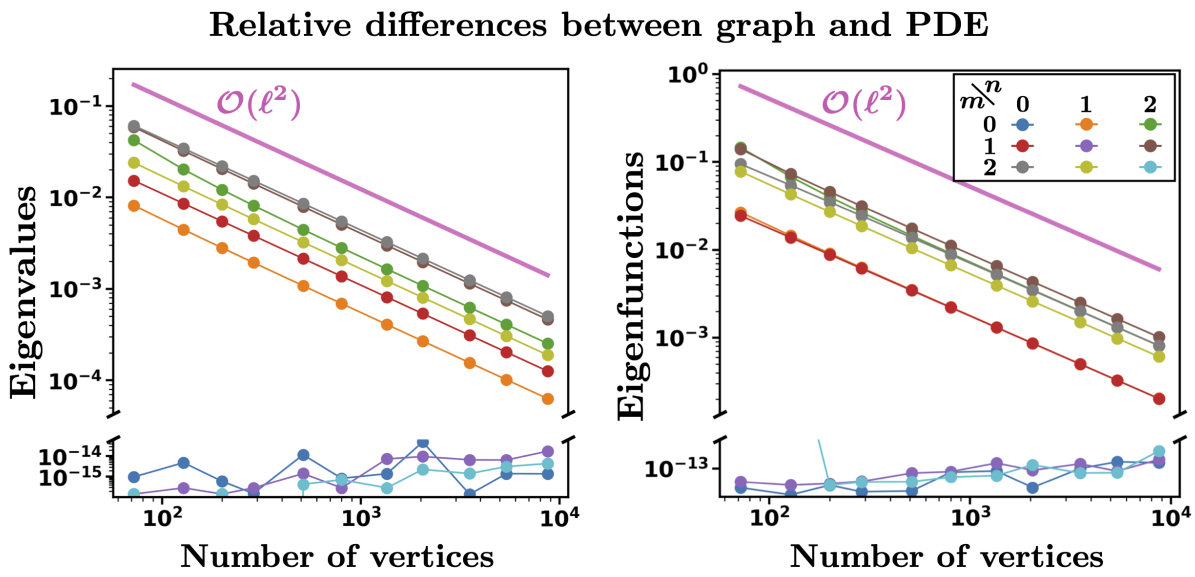

Figure 4.15: Convergence of NEP solutions to continuum limiting PDE solutions for periodic rectangular graphs of increasing densities in the flat square torus.

spanned by the basis functions as follows

- If $(m, n) = (0, 0)$: 1
- If $m = 0$: $\cos(\kappa_y(n)y)$, $\sin(\kappa_y(n)y)$
- If $n = 0$: $\cos(\kappa_x(m)x)$, $\sin(\kappa_x(m)x)$
- If $(m, n) = (1, 2)$:

$$\begin{aligned} \cos(\kappa_1(1)x)\cos(\kappa_y(2)y)\ ,\ \cos(\kappa_x(1)x)\sin(\kappa_y(2)y)\ , \\ \sin(\kappa_x(1)x)\cos(\kappa_y(2)y)\ ,\ \sin(\kappa_x(1)x)\sin(\kappa_y(2)y)\ , \\ \cos(\kappa_x(3)x)\ ,\ \sin(\kappa_y(3)y) \end{aligned}$$

- Otherwise:

$$\begin{aligned} \cos(\kappa_x(m)x)\cos(\kappa_y(n)y)\ ,\ \cos(\kappa_x(m)x)\sin(\kappa_y(n)y)\ , \\ \sin(\kappa_x(m)x)\cos(\kappa_y(n)y)\ ,\ \sin(\kappa_x(m)x)\sin(\kappa_y(n)y) \end{aligned}$$

Projecting onto the graph eigenspaces for each PDE eigenspace, we indeed find clear partitions of the graph eigenvalues and eigenfunctions and see convergence for increasing vertex densities, as shown in figure 4.15. Figure 4.16 visually compares the graph and PDE modes on a graph of size $|V| \approx 500$. For example, for the eigenvalue corresponding to $(m, n) = (1, 0)$, we project the corresponding PDE modes, *restricted to the graph*, onto the two closest matching graph modes. We obtain the two superpositions in the (left) graph column, second from the top. We see good agreement between the two sets of modes. Again, we see exact agreement for $m = n$, and $\mathcal{O}(\ell^2)$ convergence otherwise. The exact agreement again is explained by the dispersion relation from the vertex condition eq. (4.39), where $k = 2m\pi$ is required when $m = n$. Another observation is that this

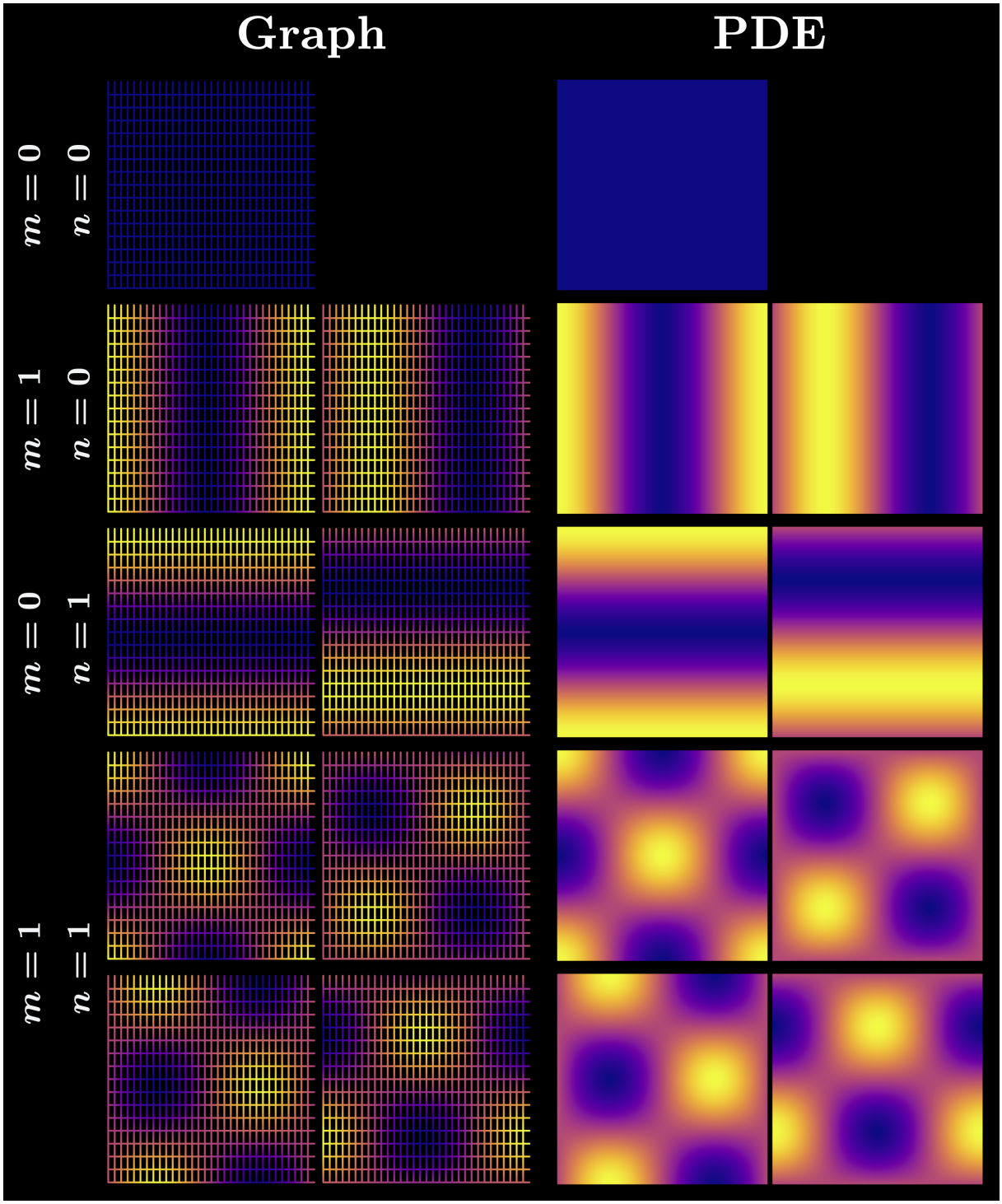

Figure 4.16: Visual comparison of the first several rectangular lattice graph and PDE modes in the flat square torus.

entire procedure generalises for a general ratio $\ell_x = \alpha\ell, \ell_y = \ell$. The corresponding PDE agrees with the limiting NEP,

$$\left(\frac{\alpha}{\alpha+1}\partial_x^2 + \frac{1}{\alpha+1}\partial_y^2\right) f \;=\; \lambda f, \tag{4.45}$$

which accords with [82], who model advection-diffusion on a rectangular grid. By approximating the concentration in the long time limit with a Gaussian diffusion kernel, they find an effective zero-advection diffusivity tensor, K, near the source ([82] eqs. (12-14))

$$K \;=\; \frac{R}{\mathrm{tr}(R)} \;=\; \frac{1}{\alpha+1}\begin{bmatrix}\alpha & 0\\ 0 & 1\end{bmatrix}. \tag{4.46}$$

They also find a medium-range diffusion kernel based on the squared Manhattan distance, $\|x\|_1$, rather than the rotationally invariant Euclidean metric, $||x||_2$. However, the general bound $||x||_1^2 \leq d\,||x||_2^2$ implies the results accord in the full continuum limit.

4.3.3 Periodic hexagonal graph in the rectangular flat torus

We now introduce a homogeneous and isotropic example requiring a more involved approach.

Graph construction To construct the vertices of the periodic hexagonal graph, we use the setup of the hexagonal multilattice in figure 4.2. For some distance ℓ, we set one basis vertex as a green (West) vertex $v_W = (-\ell/2, 0)$, another as a red (East) vertex $v_E = (\ell/2, 0)$, and we set the lattice vectors to be

$$e_1 \;=\; \frac{\ell}{2}(3, \sqrt{3}) \tag{4.47}$$

$$e_2 \;=\; \frac{\ell}{2}(3, -\sqrt{3}). \tag{4.48}$$

For some, as yet defined, finite set of integer linear combinations of the basis vertices, we generate two sets of vertices V_W, V_E, where $V = V_W \cup V_E$. Then, defining the edge function

$$r(j) \;=\; \ell\left(\cos\left(j\frac{\pi}{3}\right), \sin\left(j\frac{\pi}{3}\right)\right), \tag{4.49}$$

each $v_W \in V_W$ is connected to three neighbouring $v_E \in V_E$ by edge vectors $r(j)$ for $j = 0, 2, 4$. Likewise, each $v_E \in V_E$ is connected to three neighbouring $v_W \in V_W$ by edge vectors $r(j)$ for $j = 1, 3, 5$. The resulting metric graph structure is illustrated in figure 4.17 where each edge has length ℓ. Depending on the choice of unit cell and corresponding translation vectors, there are several ways of generating and studying hexagonal graphs. So that we can derive a simple, exactly solvable graph problem and corresponding continuum limit, we choose a method which fills in a flat rectangular torus. The method is illustrated and explained in figure 4.18. Starting with a unit cell whose bottom left corner is at $(0, 0)$, we tile a rectangular torus with N positive horizontal translations and N positive vertical translations. Rescaling so that the total horizontal length is 1, we obtain

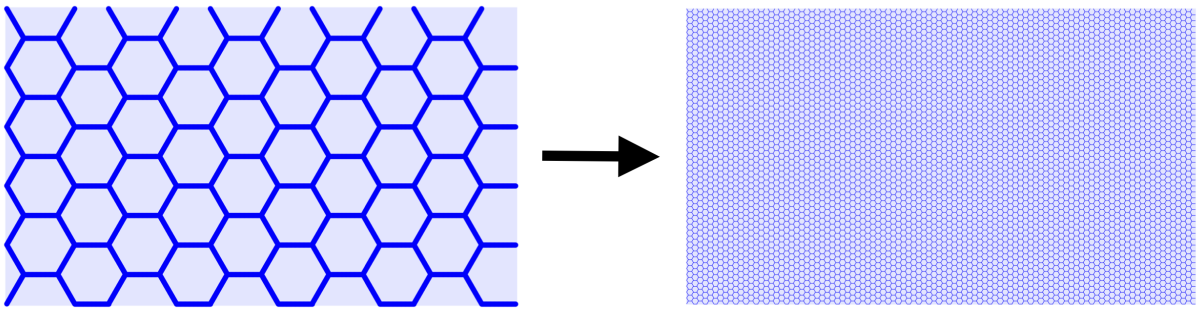

Figure 4.17: Illustration of the continuum limiting procedure for the periodic hexagonal graph filling in the $1 \times 1/\sqrt{3}$ rectangular flat torus.

a height of $1/\sqrt{3}$ (figure 4.17). The edge length ℓ and N are related by $N(3\ell e_x) = e_x$ and so $N = \frac{1}{3\ell}$. Vertices are naturally identified along the boundary.

Graph problem We posit one plane wave solution on each sublattice V_E, V_W:

$$f_W(v) \;=\; \hat{f}_W e^{i\kappa\cdot v} + \text{c.c.}, \quad f_E(v) \;=\; \hat{f}_E e^{i\kappa\cdot v} + \text{c.c.} \tag{4.50}$$

where $v = ae_1 + be_2$ is a vertex coordinate, and $\kappa = q_1\tilde{e}_1 + q_2\tilde{e}_2$ is expressed in the dual basis

$$\tilde{e}_1 \;=\; \frac{1}{3\ell}\left(1, \sqrt{3}\right) \tag{4.51}$$

$$\tilde{e}_2 \;=\; \frac{1}{3\ell}\left(1, -\sqrt{3}\right). \tag{4.52}$$

The components are quantized according to the graph density in the toroidal geometry. We require

$$e^{i\kappa\cdot(v+N3\ell e_x)} \;=\; e^{i\kappa\cdot v}, \quad e^{i\kappa\cdot(v+N\sqrt{3}\ell e_y)} \;=\; e^{i\kappa\cdot v}. \tag{4.53}$$

This gives

$$q_1 \;=\; \pi\frac{m+n}{N}, \quad q_2 \;=\; \pi\frac{m-n}{N} \tag{4.54}$$

for integers m, n where $0 \leq m \leq N-1$ and $0 \leq n \leq \min(m, N-1-m)$. Substituting in $\ell = \frac{1}{3N}$, we set $q_1 = \kappa_1\ell$, $q_2 = \kappa_2\ell$ for $\kappa_1 = 3(m+n)\pi$, $\kappa_2 = 3(m-n)\pi$. There are two different vertex conditions corresponding to each distinct neighbourhood in the multilattice structure, as illustrated in figure 4.19. We have

$$3\cos(k\ell)\, f_W(v_W) \;=\; f_E(v_E) + f_E(v_E - e_1) + f_E(v_E - e_2) \tag{4.55}$$

$$3\cos(k\ell)\, f_E(v_E) \;=\; f_W(v_W) + f_W(v_W + e_1) + f_W(v_W + e_2) \tag{4.56}$$

In matrix form

$$\begin{pmatrix} -3\cos(k\ell) & 1 + e^{-i\kappa\cdot e_1} + e^{-i\kappa\cdot e_2} \\ 1 + e^{i\kappa\cdot e_1} + e^{i\kappa\cdot e_2} & -3\cos(k\ell) \end{pmatrix} \begin{pmatrix} f_E(v_E) \\ f_W(v_W) \end{pmatrix} \;=\; 0. \tag{4.57}$$

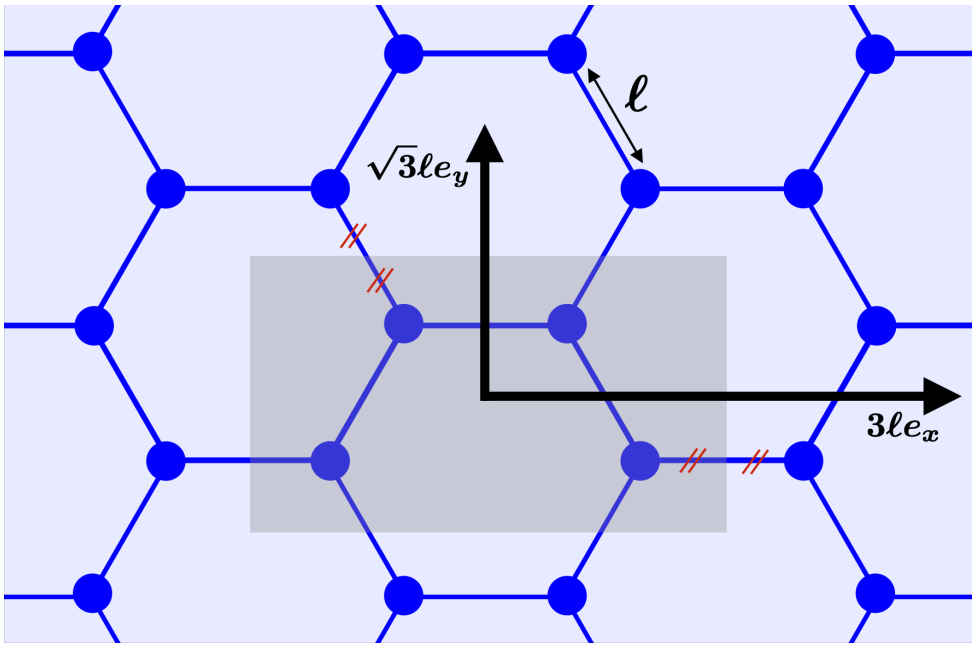

Figure 4.18: Illustration of the tiling procedure for the periodic hexagonal graph in the rectangular flat torus. The lattice spacing (distance between vertices) is a constant ℓ. The unit cell (in grey) is a $3\ell \times \sqrt{3}\ell$ rectangle, which is centred (indicated by the red dashes) at the top four vertices of a hexagon. It can then be translated horizontally and vertically by the vectors $3\ell e_x$ and $\sqrt{3}\ell e_y$ to obtain lattices such as those in figure 4.17.

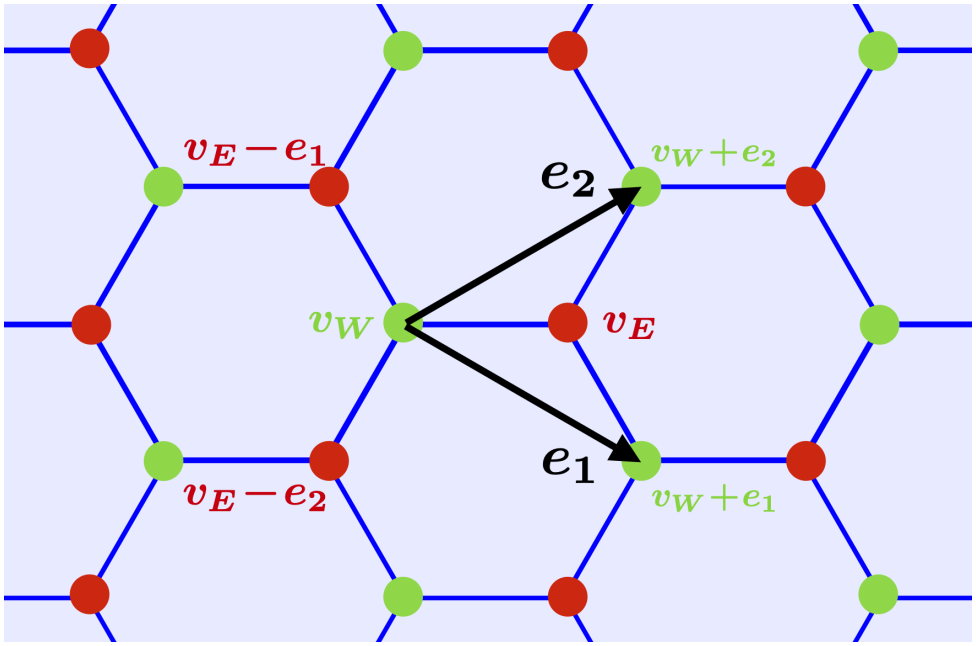

Figure 4.19: Illustration of the unit vertices of the hexagonal lattice. The unit vertices are v_E and v_W (East, West) The unit lattice vectors e_1, e_2 generate the lattice. If ℓ is the global edge length, then $e_1 = \ell((1,0) + (\cos(\pi/3), \sin(\pi/3)))$ and $e_2 = \ell((1,0) + (\cos(\pi/3), -\sin(\pi/3)))$.

The dispersion relation is given by setting the determinant to 0:

$$9\cos(k\ell)^2 \;=\; 3 + 2\left(\cos(\ell\kappa_1) + \cos(\ell(\kappa_1 - \kappa_2)) + \cos(\ell\kappa_2)\right). \tag{4.58}$$

To leading order,

$$\begin{aligned} k^2 &= \frac{1}{2}\kappa\cdot\kappa + \mathcal{O}\big(\ell^2\big) && (4.59)\\ &= \frac{1}{2}\left(\frac{4}{9}(\kappa_1^2 - \kappa_1\kappa_2 + \kappa_2^2)\right) + \mathcal{O}\big(\ell^2\big) && (4.60)\\ &= \frac{1}{2}\left((2\pi m)^2 + 3(2\pi n)^2\right) + \mathcal{O}\big(\ell^2\big), && (4.61) \end{aligned}$$

This is confirmed in the continuum limit.

Continuum limit The vertex density $\mu(v) = \mu$ is constant. Edges all have the same length ℓ. Edge vectors at v_W are $r_j = (\cos(j2\pi/3), \sin(j2\pi/3))$ for $j = 0, 1, 2$, and are $-r_j$ at v_E. Therefore, at any v,

$$R(v) \;=\; \ell(r_0\otimes r_0 + r_1\otimes r_1 + r_2\otimes r_2) \;=\; \frac{3}{2}\ell I. \tag{4.62}$$

The continuum PDE then simplifies to

$$\frac{1}{2}\left(\frac{\partial}{\partial x^2} + \frac{\partial}{\partial y^2}\right) f(x,y) \;=\; -k^2 f(x,y). \tag{4.63}$$

In the flat rectangular $1\times 1/\sqrt{3}$ torus, this has plane wave solutions

$$f(x,y) \;=\; Ae^{i(\kappa_x x + \kappa_y y)} + \text{c.c.} \tag{4.64}$$

where $\kappa_x = 2\pi m$, $\kappa_y = \sqrt{3}(2\pi n)$ for $m, n \in \mathbb{N}$ and if $\kappa = \kappa_x e_x + \kappa_y e_y$, then

$$k^2 \;=\; \frac{1}{2}\kappa\cdot\kappa \;=\; \frac{1}{2}\left((2\pi m)^2 + 3\,(2\pi n)^2\right). \tag{4.65}$$

Comparison between finite graph problem and continuum limit For comparison, we choose the eigenspaces corresponding to $(m,n) \in \{0,1,2\}^2$, as in table 4.2. Define $\kappa_x(m) = 2\pi m$, $\kappa_y(n) = \sqrt{3}(2\pi n)$. For $0 \le m, n \le 2$, the eigenspaces are spanned by the basis functions as follows

- If $(m,n) = (0,0)$: 1
- If $(m,n) = (0,1)$: $\cos(\kappa_y(n)y)$, $\sin(\kappa_y(n)y)$
- If $(m,n) = (0,2)$:

$$\begin{gathered} \cos(\kappa_y(2)y)\;,\;\; \sin(\kappa_y(2)y)\,,\\ \cos(\kappa_x(3)x)\cos(\kappa_y(1)y)\;,\;\; \cos(\kappa_x(3)x)\sin(\kappa_y(1)y)\,,\\ \sin(\kappa_x(3)x)\cos(\kappa_y(1)y)\;,\;\; \sin(\kappa_x(3)x)\sin(\kappa_y(1)y)\,, \end{gathered}$$

$m \setminus n$	0	1	2
0	0	$6\pi^2$	$24\pi^2$
1	$2\pi^2$	$8\pi^2$	$26\pi^2$
2	$8\pi^2$	$14\pi^2$	$32\pi^2$
3	$18\pi^2$	$24\pi^2$	
4	$32\pi^2$		

Table 4.3: Continuum limiting eigenvalues for the periodic hexagonal graph in the rectangular flat torus. We show $k^2 = \frac{1}{2}\left((2\pi m)^2 + 3\,(2\pi n)^2\right)$ for $(m,n) \in \{0,1,2\}^2$. We include any extra eigenvalues which coincide with those in the set.

- If $(m,n) = (1,0)$: $\cos(\kappa_y(1)x)$, $\sin(\kappa_y(1)x)$
- If $(m,n) = (1,1)$ or $(2,0)$:

$$\begin{aligned} \cos(\kappa_x(1)x)\cos(\kappa_y(1)y)\ ,\ \cos(\kappa_x(1)x)\sin(\kappa_y(1)y)\,,\\ \sin(\kappa_x(1)x)\cos(\kappa_y(1)y)\ ,\ \sin(\kappa_x(1)x)\sin(\kappa_y(1)y)\,,\\ \cos(\kappa_y(1)x)\ ,\ \sin(\kappa_y(1)x)\,, \end{aligned}$$

- If $(m,n) = (2,2)$:

$$\begin{aligned} \cos(\kappa_x(2)x)\cos(\kappa_y(2)y)\ ,\ \cos(\kappa_x(2)x)\sin(\kappa_y(2)y)\,,\\ \sin(\kappa_x(2)x)\cos(\kappa_y(2)y)\ ,\ \sin(\kappa_x(2)x)\sin(\kappa_y(2)y)\,,\\ \cos(\kappa_y(4)x)\ ,\ \sin(\kappa_y(4)x)\,, \end{aligned}$$

- Otherwise:

$$\begin{aligned} \cos(\kappa_x(m)x)\cos(\kappa_y(n)y)\ ,\ \cos(\kappa_x(m)x)\sin(\kappa_y(n)y)\,,\\ \sin(\kappa_x(m)x)\cos(\kappa_y(n)y)\ ,\ \sin(\kappa_x(m)x)\sin(\kappa_y(n)y) \end{aligned}$$

Projecting onto the graph eigenspaces for each PDE eigenspace, we indeed find clear partitions of the graph eigenvalues and eigenfunctions and see convergence for increasing vertex densities, as shown in figure 4.20. Figure 4.21 is a visual comparison of the graph and PDE modes on a graph of size $|V| \approx 500$. For example, for the eigenvalue corresponding to $(m,n) = (1,0)$, we project the corresponding PDE modes, *restricted to the graph*, onto the two closest matching graph modes. We obtain the two superpositions in the (left) graph column, second from the top. We see good agreement between the two sets of modes.

4.3.4 Square lattice in the unit square with clamped boundaries

In this example we demonstrate the effect of boundary conditions. We fill in the 1×1 unit square M with the periodic square graph (figure 4.22). The boundary $\partial G \subset G$ is the

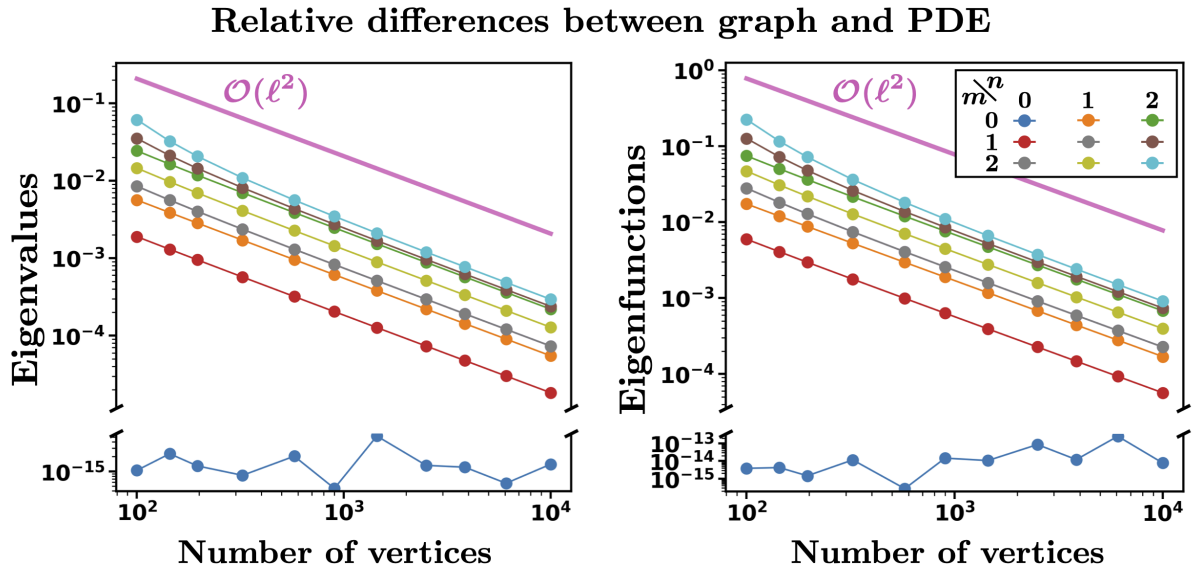

Figure 4.20: Convergence of NEP solutions to continuum limiting PDE solutions for periodic hexagonal graphs of increasing densities in the flat rectangular torus.

subset of the graph coinciding with the boundary of M. We apply clamped (0 Dirichlet) boundary conditions $f(\partial G) = 0$.

Graph problem This time, we assume sinusoidal plane wave solutions

$$f(v) \;=\; A\sin(\kappa \cdot v)\,, \tag{4.66}$$

where v and κ are expressed in the lattice and dual basis vectors as before. The vertex condition is then

$$\begin{aligned} 4\cos(k\ell)\sin(\kappa\cdot v) \;=\; &\sin(\kappa\cdot(v+e_1)) + \sin(\kappa\cdot(v-e_1)) \\ &+ \sin(\kappa\cdot(v+e_2)) + \sin(\kappa\cdot(v-e_2)) \end{aligned} \tag{4.67}$$

giving the dispersion relation

$$2\cos(k\ell) \;=\; \cos(\kappa_1\ell) + \cos(\kappa_2\ell)\,, \tag{4.68}$$

as expected. This time, the global boundary condition means that

$$\kappa_1 \;=\; m\pi, \quad \kappa_2 \;=\; n\pi, \quad 0 < m, n \leq N-1. \tag{4.69}$$

To leading order

$$k^2 \;=\; \frac{1}{2}\kappa\cdot\kappa + \mathcal{O}\big(\ell^2\big)\,. \;=\; \frac{1}{2}((m\pi)^2 + (n\pi)^2) + \mathcal{O}\big(\ell^2\big)\,. \tag{4.70}$$

This is confirmed in the continuum limit.

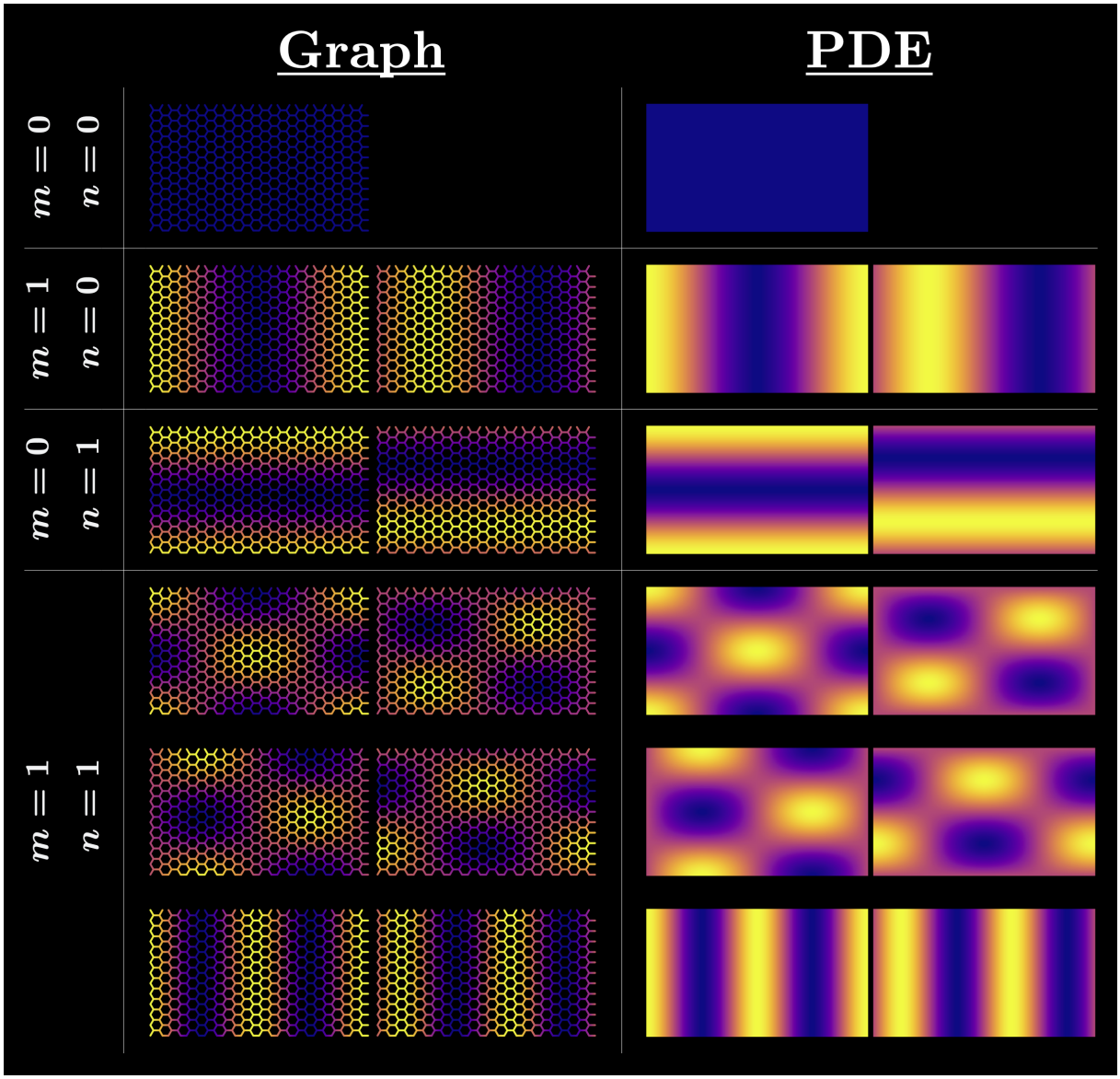

Figure 4.21: Visual comparison of the first several periodic hexagonal graph and PDE modes in the flat rectangular torus.

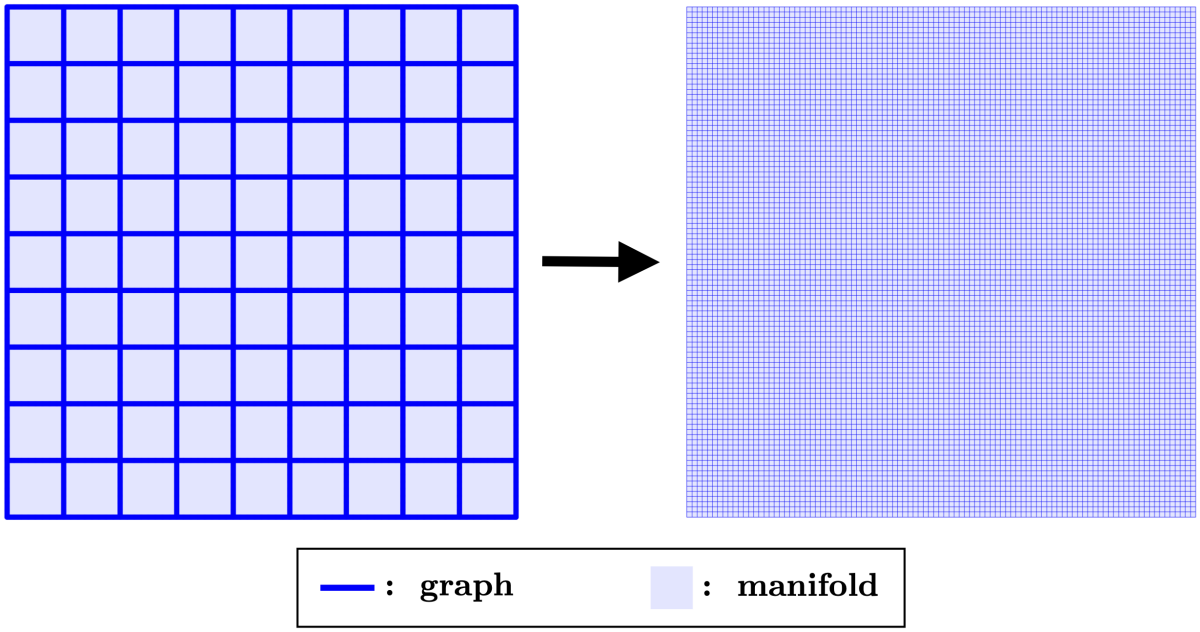

Figure 4.22: Illustration of the continuum limiting procedure for the periodic square graph filling in the unit square.

$m \backslash n$	1	2	3
1	π^2	$\frac{5}{2}\pi^2$	$5\pi^2$
2	$\frac{5}{2}\pi^2$	$4\pi^2$	$\frac{13}{2}\pi^2$
3	$5\pi^2$	$\frac{13}{2}\pi^2$	$9\pi^2$

Table 4.4: Continuum limiting eigenvalues for the periodic square graph in the square with clamped (0 Dirichlet) boundaries. We show $k^2 = \frac{1}{2}\left((\pi m)^2 + (\pi n)^2\right)$ for $(m, n) \in \{1, 2, 3\}^2$.

Continuum limit With $R(v) = 2\ell I$ and $\mu(v) = \mu$ some constant, we again have at all (interior) vertices

$$\frac{1}{2}\left(\frac{\partial^2}{\partial x^2} + \frac{\partial^2}{\partial y^2}\right) f(x, y) \;=\; -k^2 f(x, y). \tag{4.71}$$

Along the boundaries, we simply have $f(x, y) = 0$. This has sine series solutions

$$f(x, y) \;=\; A \sin(\kappa \cdot (x, y)) \tag{4.72}$$

where $\kappa = \pi(me_x + ne_y)$ for $m, n \in \mathbb{N}_{>0}$ and

$$k^2 \;=\; \frac{1}{2}((m\pi)^2 + (n\pi)^2). \tag{4.73}$$

Comparison between finite graph problem and continuum limit For comparison, we choose the eigenspaces corresponding to $m, n \in \{1, 2, 3\}^2$, as in table 4.4. Define

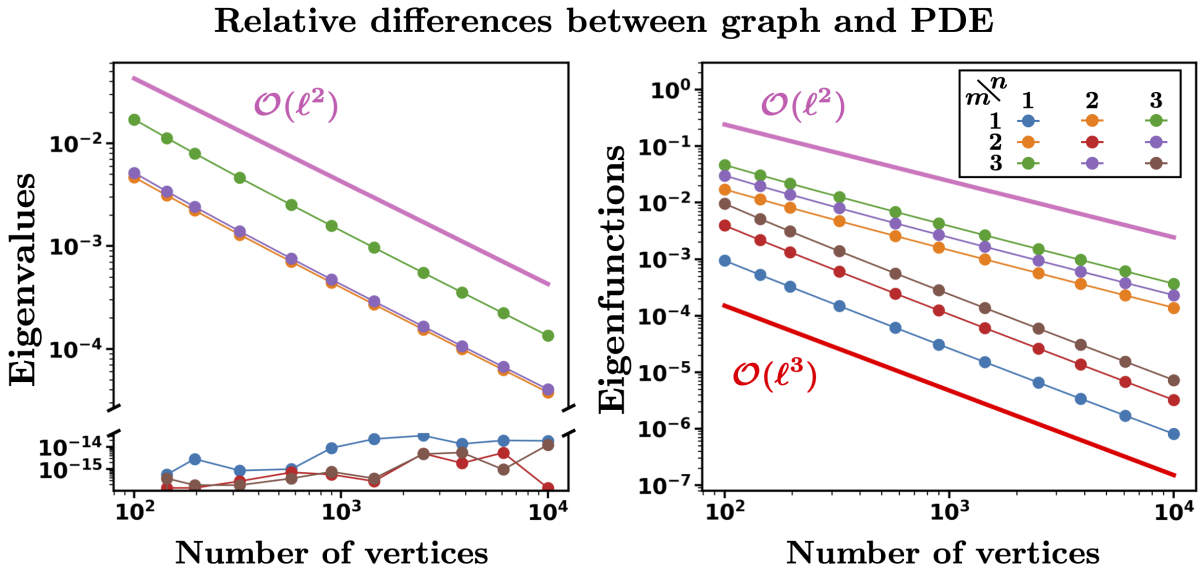

Figure 4.23: Convergence of NEP solutions to continuum limiting PDE solutions for periodic square graphs of increasing densities in the square.

$\kappa_x(m) = \pi m$, $\kappa_y(n) = \pi n$. For $1 \leq m, n \leq 3$, the eigenspaces are spanned by the basis functions as follows

- If $n = m$: $\sin(\kappa_x(m)x)\sin(\kappa_y(m)y)$
- Otherwise: $\sin(\kappa_x(m)x)\sin(\kappa_y(n)y)\,, \sin(\kappa_x(n)x)\sin(\kappa_y(m)y)$.

Projecting onto the graph eigenspaces for each PDE eigenspace, we find clear partitions of the graph eigenvalues and eigenfunctions and see convergence for increasing vertex densities, as shown in figure 4.23. We see $\mathcal{O}(\ell^2)$ convergence everywhere except for the $m = n$ modes. For the eigenvalues, we see again from the dispersion relation (eq. 4.68) that if $m = n$, then

$$k \;=\; \frac{1}{\ell}\arccos\left(\frac{1}{2}\left(\cos(m\pi\ell) + \cos(m\pi\ell)\right)\right) \;=\; m\pi. \tag{4.74}$$

This is independent of the vertex density. For the eigenmodes, it is unclear why there is $\mathcal{O}(\ell^3)$ convergence instead of exact agreement. Figure 4.24 is a visual comparison of the graph and PDE modes on a graph of size $|V| \approx 500$.

4.4 In three dimensions

Here, we present a three-dimensional continuum limit constructed from a three-dimensional cubic lattice as in figure 4.25. In this case, we evenly stack periodic square graphs (figure 4.22) in a third dimension. We fill in the unit cube given by $0 \leq x, y, z \leq 1$ with N vertices in each dimension for a total of $|V| = N^3$. We set clamped boundary conditions at $x, y, z \in \{0, 1\}$. The lattice spacing (global edge length) is ℓ, and if $e_1, e_2, e_3 = \ell e_x, \ell e_y, \ell e_z$

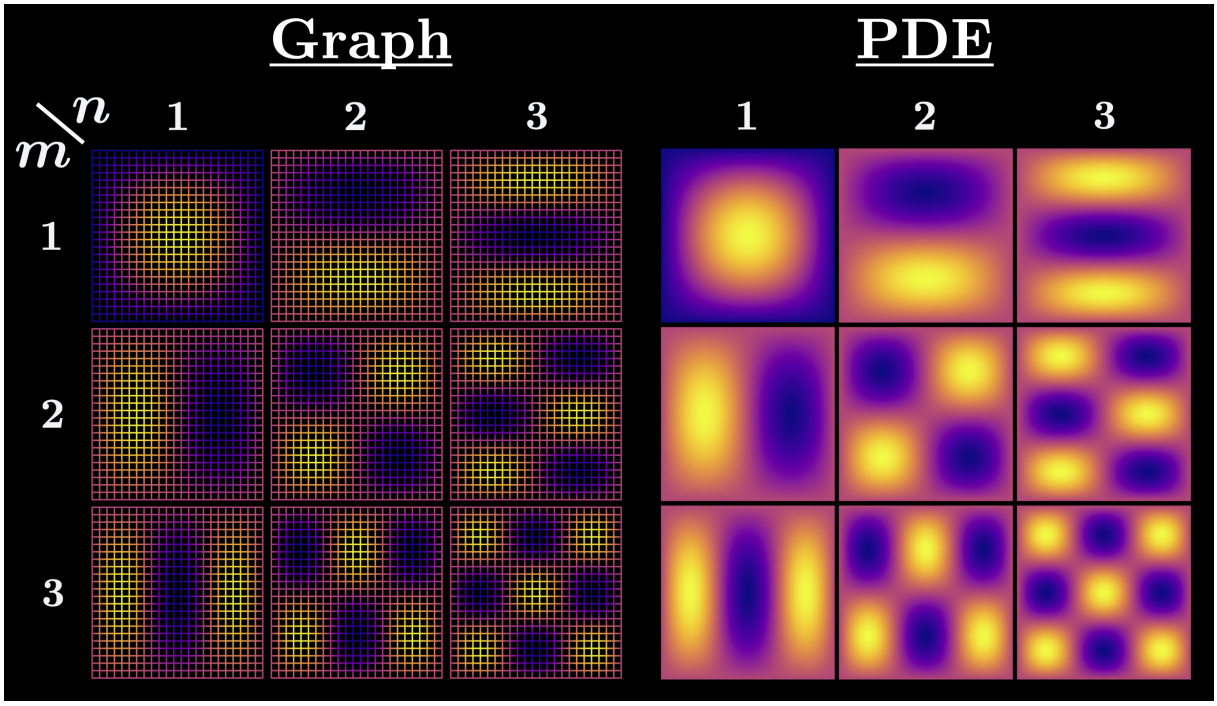

Figure 4.24: Visual comparison of the graph and PDE modes for the square lattice in the square with clamped boundaries. The PDE modes (right) are the standard $\sin(m\pi x)\sin(n\pi y)$ functions, here represented on the square. The left is a grid of PDE-restricted modes projected onto graph modes. We see good agreement between the two sets. Data corresponding to the fifth graph size in figure 4.23 confirms this.

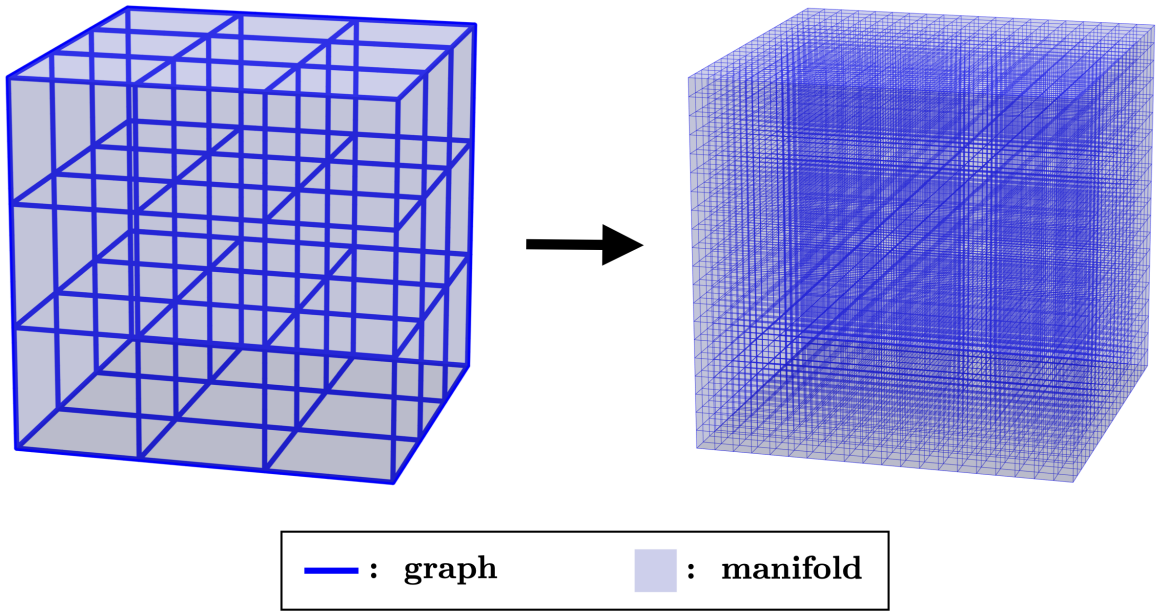

Figure 4.25: Illustration of the continuum limiting procedure for the periodic cubic graph in the cube.

are lattice vectors, then the vertex condition for plane wave solutions $A\sin(\kappa\cdot(x,y,z))$ is

$$\cos(k\ell) \;=\; \frac{1}{3}\left(\cos(\kappa_1\ell)+\cos(\kappa_2)+\cos(\kappa_3\ell)\right) \tag{4.75}$$

The clamped boundary condition implies $\kappa_i = m_i\pi$ for $0 < m_i \leq N-1$, and so to leading order

$$k^2 \;=\; \frac{1}{3}\kappa\cdot\kappa+\mathcal{O}\big(\ell^2\big) \;=\; \frac{1}{3}(m_1^2+m_2^2+m_3^2)\pi^2+\mathcal{O}\big(\ell^2\big)\,. \tag{4.76}$$

The factor $1/3$, as before, corresponds to a rescale by the dimension $d=3$ of the embedding space.

For the continuum limit, the vertex density is constant, and the edge tensor is simply $R(v) = 2\ell I$, where here, I is of course the three-dimensional identity. Therefore, we obtain,

$$\frac{1}{3}\left(\frac{\partial^2}{\partial x^2}+\frac{\partial^2}{\partial y^2}+\frac{\partial^2}{\partial z^2}\right)f(x,y,z) \;=\; -k^2 f(x,y,z). \tag{4.77}$$

Along the boundaries, we simply have $f(x,y,z)=0$. This has sine series solutions

$$f(x,y,z) \;=\; A\sin(\kappa\cdot(x,y,z)) \tag{4.78}$$

where $\kappa = \pi(m_x e_x + m_y e_y + m_z z)$ for $m_x, m_y, m_z \in \mathbb{N}_{>0}$ and

$$k^2 \;=\; \frac{1}{2}((m_x\pi)^2+(m_y\pi)^2+(m_z\pi)^2). \tag{4.79}$$

We present a comparison of graph and continuum solutions in figure 4.26. We present the eigenspaces for m_x, m_y, m_z taking (all permutations of) values $(1,1,1)$, $(1,1,2)$ and $(1,2,2)$.

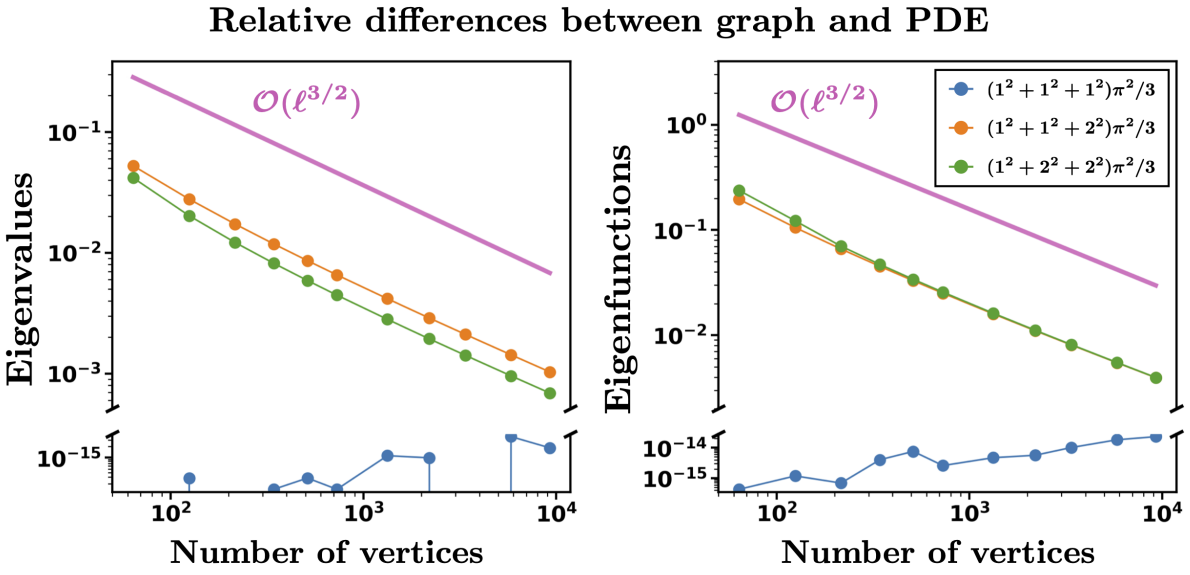

Figure 4.26: Convergence of NEP solutions to continuum limiting PDE solutions for periodic cubic graphs of increasing densities in the cube.

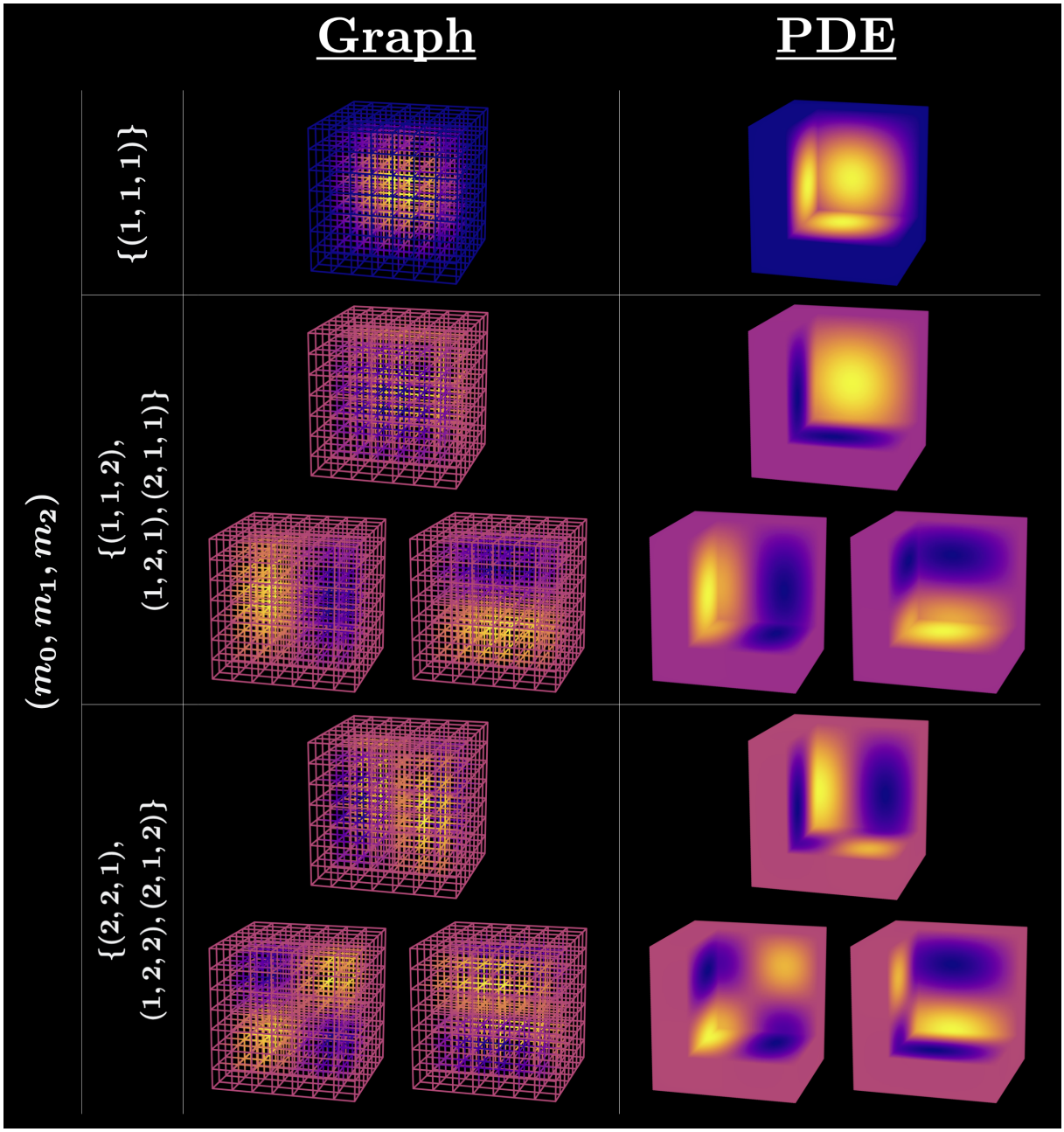

Figure 4.27: Comparison of modes of the periodic cubic graph in the cube.

Chapter 5

Semi-analytical examples in flat and curved space

This chapter tests the continuum model on several inhomogeneous graphs where solutions can be found, at least partially, in closed form. These examples are inspired by networks arising in nature. The humble spiderweb (figure 5.1) is the canonical example. We model this as periodic in the angular domain, allowing for a separation into Fourier modes in the angular direction, and radial modes of an ODE depending on the distribution of radial vertices. We see that certain radial distributions allow for closed-form Bessel-like solutions. The second example comes from the sequence of Goldberg/geodesic polyhedra. These networks produce some of the most uniform tilings of the 2-sphere and, therefore, arise ubiquitously in nature as the minimizing structures of many energy functionals [124, 125]. Notable examples are the heads (capsids) of tailed bacteriophages (figure 5.1). These tailed bacteriophages ("bacteria" + "phageia" meaning devour) infect and replicate inside bacteria, and make up an estimated 96% [126] of the 10^{31} bacteriophages on the planet [127, 128]. Outnumbering every other organism on Earth combined, one could be

Figure 5.1: Naturally occurring highly structured networks. A spiderweb [122] and the polyhedral head of a T4 bacteriophage [123] (with icosahedral symmetry).

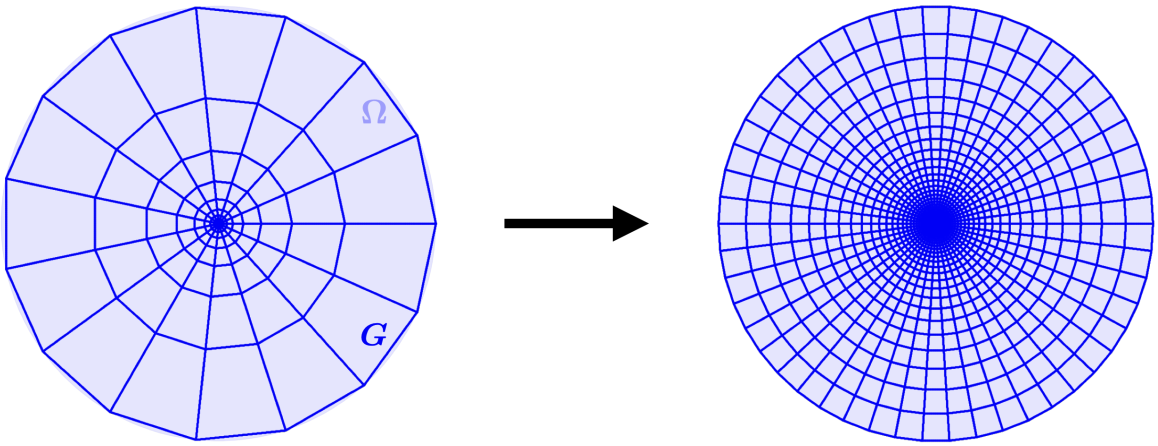

Figure 5.2: Illustration of the continuum limiting procedure for the spiderweb within the unit disc.

forgiven for thinking that icosahedral symmetry is crucial for life as we know it. Other notable polyhedra are the fullerenes–meshes of carbon atoms–such as the famous carbon C_{60} a.k.a. Buckminsterfullerene, a.k.a. soccer ball.

5.1 Spiderweb

Construction An axisymmetric "spiderweb" (figure 5.2) filling in the unit disc provides a straightforward inhomogeneous anisotropic semi-analytic example. Periodicity in the angular direction allows for the decoupling of functions into angular Fourier modes, and radial functions depend on the distribution of vertices in the radial direction. The spiderweb has local vertex spacings $\mathrm{d}r$, $\mathrm{d}\theta$ in each polar coordinate direction r, θ. It has a central vertex at the origin, boundary vertices on the unit circle, and interior vertices otherwise. In total, there are $|V| = (N_r - 1)N_\theta + 1$ vertices, where N_r, N_θ are the numbers of vertices in the radial and angular directions respectively. An interior vertex $v = r(\cos(\theta), \sin(\theta))$ has neighbours

$$\begin{aligned} w_N &= (r + \mathrm{d}r)(\cos(\theta), \sin(\theta)) \\ w_S &= (r - \mathrm{d}r)(\cos(\theta), \sin(\theta)) \\ w_E &= r(\cos(\theta + \mathrm{d}\theta), \sin(\theta + \mathrm{d}\theta)) \\ w_W &= (r + \mathrm{d}r)(\cos(\theta - \mathrm{d}\theta), \sin(\theta - \mathrm{d}\theta)) \end{aligned}$$

The central vertex v_c has neighbours

$$w_n = \mathrm{d}r \left(\cos\left(2\pi \frac{n}{N_\theta}\right), \sin\left(2\pi \frac{n}{N_\theta}\right) \right), \quad \text{for} \quad 0 \le n < N_\theta. \tag{5.1}$$

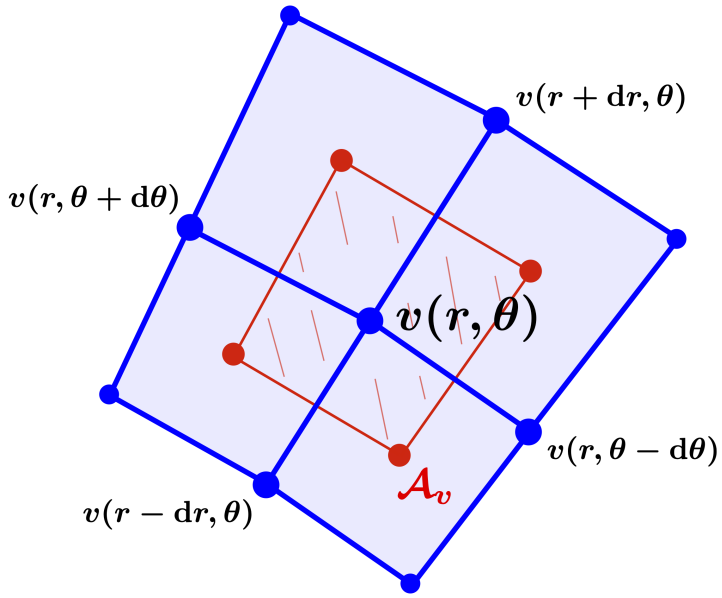

Figure 5.3: Illustration of the neighbourhood of an interior vertex of the spiderweb. The Voronoi cell area is given by $\mathcal{A}_v$.

The boundary vertices $v_{\partial G}$ at $r = 1$ have neighbours

$$w_S = (1 - \mathrm{d}r)(\cos(\theta), \sin(\theta)) \tag{5.2}$$
$$w_E = (\cos(\theta + \mathrm{d}\theta), \sin(\theta + \mathrm{d}\theta)) \tag{5.3}$$
$$w_W = (\cos(\theta - \mathrm{d}\theta), \sin(\theta - \mathrm{d}\theta)) \tag{5.4}$$

Continuum limit The angular spacing is constant for a given graph $\mathrm{d}\theta = 2\pi/N_\theta$. We choose the radial spacing to depend smoothly on r such that $\mathrm{d}r = \rho(r)\mathrm{d}\theta$. In the polar basis, the R tensor at interior vertices is then

$$R(r) = R_{rr}\,\hat{e}_r \otimes \hat{e}_r + R_{\theta\theta}\,\hat{e}_\theta \otimes \hat{e}_\theta, \tag{5.5}$$

where,

$$R_{rr} = 2\rho(r)\mathrm{d}\theta + 4\,r\sin^3\left(\frac{\mathrm{d}\theta}{2}\right), \tag{5.6}$$
$$R_{\theta\theta} = \frac{r\sin^2(\mathrm{d}\theta)}{\sin\left(\frac{\mathrm{d}\theta}{2}\right)}. \tag{5.7}$$

For $\mathrm{d}\theta \to 0$,

$$R_{rr} \sim 2\rho(r)\mathrm{d}\theta, \quad R_{\theta\theta} \sim 2\,r\mathrm{d}\theta. \tag{5.8}$$

For the vertex density, we use the primitive cell area introduced for the lattices. We construct the cell by connecting the centres of tiles adjacent to v. This is illustrated in figure 5.3. This is an approximation of the Voronoi cell whose sides are given by connecting perpendicular bisectors of each edge adjacent to v. The shoelace formula for the area of

any planar polygon with vertices v_i (ordered by polar angle) is

$$A \;=\; \frac{1}{2}\sum_i \left|v_i \wedge v_{i+1}\right| \tag{5.9}$$

where $\wedge$ is the exterior product. Applying this to the Voronoi cell with vertices in red, we have for $\mathrm{d}\theta \to 0$

$$\mathcal{A}_v \;=\; \frac{1}{2} r\rho(r)\mathrm{d}\theta(1+\cos(\mathrm{d}\theta))\sin(\mathrm{d}\theta) \;\sim\; r\rho(r)\mathrm{d}\theta^2. \tag{5.10}$$

The vertex density is then $\mu(v) = 1/\mathcal{A}_v$. To leading order, the continuum PDE eq. (2.42) is

$$\frac{1}{r(r+\rho(r))}\left(r\rho(r)\frac{\partial^2}{\partial r^2} + \frac{\partial^2}{\partial\theta^2}\right) f(r,\theta) \;=\; -k^2 f(r,\theta). \tag{5.11}$$

Angular symmetry allows Fourier solutions $f(r,\theta) = f_m(r)e^{im\theta} + \text{c.c.}$. The PDE then reduces to a one-dimensional radial ODE

$$r\rho(r)f_m''(r) + (r(r+\rho(r))k^2 - m^2)f_m(r) \;=\; 0. \tag{5.12}$$

As a reference, the standard two-dimensional Laplace operator in polar coordinates is

$$\frac{\partial^2}{\partial r^2} + \frac{1}{r}\frac{\partial}{\partial r} + \frac{1}{r^2}\frac{\partial^2}{\partial\theta^2} \tag{5.13}$$

No choice of the radial density $\rho(r)$ converts eq. (5.11) into this standard form. Only certain functional forms produce solutions in closed-form. Before providing an example, we first specify conditions at the the central and boundary vertices. For the central vertex, we examine the PDE within an ε-ball B_ε of the origin. The "free" boundary condition eq. (2.43) from the original bilinear form is

$$\hat{n}(v)\cdot\mu(v)R(v)\cdot\nabla f(v) \;=\; 0 \tag{5.14}$$

$$\hat{e}_r\cdot\left(\frac{1}{r\rho(r)\mathrm{d}\theta^2}\left(2\rho(r)\mathrm{d}\theta\hat{e}_r\otimes\hat{e}_r + 2r\mathrm{d}\theta\hat{e}_\theta\otimes\hat{e}_\theta\right)\right)\cdot\nabla f(v) \;=\; 0 \tag{5.15}$$

$$\frac{2}{r\mathrm{d}\theta}\partial_r f(r,\theta) \;=\; 0. \tag{5.16}$$

We can approximate the PDE at the origin by taking the average value of this condition around the boundary of B_ε and taking the limit $\varepsilon \to 0$,

$$\lim_{\varepsilon\to 0}\frac{1}{\pi\varepsilon^2\mathrm{d}\theta}\int_0^{2\pi}\partial_r f(r,\theta)|_{r=\varepsilon}d\theta \;=\; 0. \tag{5.17}$$

Therefore, we impose $\partial_r f(r,\theta)|_{r=0} = 0$ at the origin. At boundary vertices of the full graph, we impose the clamped condition $f(1,\theta) = 0$.

Bessel-like solutions One option for the radial distribution of vertices which produces "recognisable" solutions is $\rho(r) = r/\gamma$ for some real, positive scalar γ. In this case,

$$r^2 f''(r) + ((1+\gamma)k^2 r^2 - \gamma m^2) f(r) \;=\; 0. \tag{5.18}$$

For $m \neq 0$, this has solutions

$$f_m(r) \;=\; \sqrt{r} J_{\frac{1}{2}\sqrt{1+4m^2\gamma}} \left(k\sqrt{1+\gamma} r\right) \tag{5.19}$$

where $J_\nu(r)$ is the non-integer order Bessel function of the first kind with zeros $\alpha_{\nu,n}$, and the clamped boundary condition requires $k = \alpha_{\nu,n}/\sqrt{1+\gamma}$. We exclude the second kind solutions Y because for $r \to 0$, $\sqrt{r} Y_{\frac{1}{2}\sqrt{1+4m^2\gamma}} \left(k\sqrt{1+\gamma} r\right) = \Theta\left(r^{\frac{1}{2}\left(1-\sqrt{1+4m^2\gamma}\right)}\right)$ which blows up at $r = 0$ for $m > 0$. For $m = 0$,

$$f_0(r) \;=\; \cos(\sqrt{1+\gamma}\, kr) \;\text{ where }\; k \;=\; \frac{(n+\frac{1}{2})\pi}{\sqrt{1+\gamma}}. \tag{5.20}$$

The central vertex condition $f'_m(r)|_{r=0} = 0$ is naturally satisfied for all m. In figure 5.4, we show convergence of graph solutions to these continuum solutions for $\gamma = 1$. Figures 5.4a-b show the convergence of the numerical graph solutions $(k,\, f)$ to the analytic PDE solutions $(\tilde{k},\, \tilde{f})$ for increasing N_r. Both cases are very efficient given the Fourier decomposition into one-dimensional radial modes. Figures 5.4c-d show visual comparisons between the graph and (graph-restricted) PDE modes, respectively.

Constructing a graph satisfying $\mathrm{d}r = r\mathrm{d}\theta$ is nontrivial. The relationship requires a recurrence relation for constructing the radial distribution of vertices with coordinates $r \in \{r_{V_r-1} = 0,\; \ldots\; , r_0 = 1\}$. Starting from the boundary vertex, we have

$$r_n \;=\; r_0(1 - \mathrm{d}\theta)^n. \tag{5.21}$$

For some fixed $\mathrm{d}\theta = 2\pi/V_\theta$, we have $r_{V_r-1} \neq 0$. We therefore calculate up to r_{V_r-2} and simply fix the final vertex at the origin. We can pick the ratio of the number of radial to angular vertices $V_r = \alpha V_\theta = \alpha M$ to approximate the theoretical limiting structure. Then

$$\lim_{M\to\infty} v_M \;=\; \lim_{M\to\infty} v_0 \left(1 - \frac{2\pi}{M}\right)^{\alpha M} \tag{5.22}$$

$$\;=\; e^{-2\pi\alpha}. \tag{5.23}$$

Setting $\alpha = 2$, then as $M \to \infty$

$$\mathrm{d}r_{\text{last}} \;=\; e^{-4\pi} \tag{5.24}$$

$$\mathrm{d}r_{\text{2nd last}} \;\sim\; \frac{4\pi}{M}\mathrm{d}r_{\text{last}} + \mathcal{O}(M^{-2}). \tag{5.25}$$

The jump to the origin is nonzero in the limit, while the second last $\mathrm{d}r$ does limit to 0. However, this setup sufficiently resolves the issue.

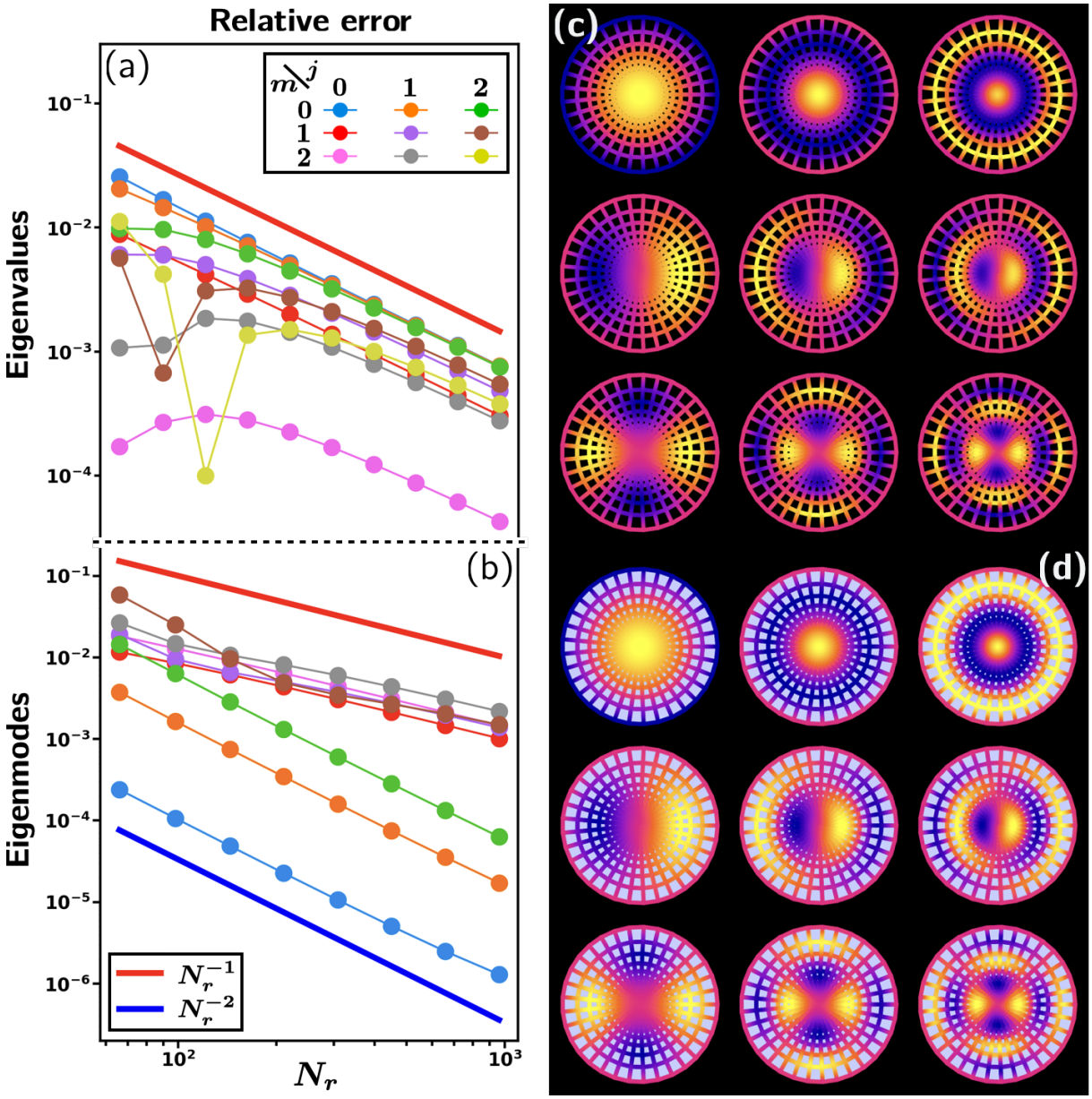

Figure 5.4: Continuum behaviour for dense spiderwebs — (a) & (b) Graph eigenvalues/eigenmodes converging to the PDE values (eqs. (5.19)–(5.20)) for increasing numbers N_r of radial vertices. (c) & (d) graph eigenmodes & graph-restricted PDE eigenmodes respectively for (m, j) as per the legend of (a) for $|V| \approx 500$; both cases only show the angular cosine (and not sine) modes.

Radial graph problem For the lattices of chapter 4, we could solve the graph NEP with plane wave solutions explicitly. For the spiderweb, we can partially solve the graph NEP by expressing f as

$$f(r,\theta) \;=\; f_m(r)e^{im\theta}. \tag{5.26}$$

At a vertex $v(r,\theta)$, edges to neighbours toward and away from the central vertex have lengths $\mathrm{d}r_-(r)$ and a $\mathrm{d}r_+(r)$ respectively. The vertex condition at an interior vertex is then

$$\begin{aligned}\frac{f_m(r+\mathrm{d}r_+)+f_m(r-\mathrm{d}r_-)}{2\sin(k\mathrm{d}r)}+\Bigg[\frac{\cos(m\mathrm{d}\theta)}{\sin(kr\mathrm{d}\sigma)}-\cot(kr\mathrm{d}\sigma)\\ -\frac{\cot(k\mathrm{d}r_+)+\cot(k\mathrm{d}r_-)}{2}\Bigg]f_m(r) \;=\; 0\end{aligned} \tag{5.27}$$

where $\mathrm{d}\sigma = 2\sin(\mathrm{d}\theta/2)$ and $|m| \le M = 2\pi/\mathrm{d}\theta$. As $\mathrm{d}r, \mathrm{d}\theta \to 0$ with $\rho = \mathrm{d}r/\mathrm{d}\theta \sim \mathcal{O}(1)$ eq. (5.27) reduces exactly to eq. (5.12) at leading order. The vertex (with M neighbours) at the origin requires special care. For the discrete case,

$$f_m(0)\cos(k\mathrm{d}r) - f_m(\mathrm{d}r)\,\delta_{m,0} \;=\; 0, \tag{5.28}$$

with Kronecker-$\delta_{m,0}$. As $\mathrm{d}r \to 0$, the centre conditions are

$$\begin{aligned} f_m(0) &= 0 \quad \text{if} \quad m \neq 0,\\ f_0'(0) &= 0 \quad \text{if} \quad m = 0.\end{aligned}$$

5.2 Truncated icosahedron

We demonstrate the continuum limit for curved surfaces with a truncated icosahedron (a.k.a. soccer ball or buckminsterfullerene) embedded within the unit 2-sphere, S^2 (figure 5.5). There are no procedures for discretizing S^2 into identical shapes of increasing density. This would provide the simplest toy model. In fact, the dodecahedron ($|V| = 20$) is the largest uniform tessellation of S^2. We examine the soccer ball which represents a simple enough intermediate case to provide analytical intuition. In this section, we interpolate its edge tensor and vertex density with spherical harmonics in order to provide a continuum limit which we then directly solve by numerical spectral discretization. There is no sense of taking increasing graph density, just as there would not be for some arbitrary network appearing in nature, for example. We see that even relatively low-density metric graphs display continuum behaviour for low-degree eigenmodes.

Construction Embedded in $\mathbb{R}^3$, the truncated icosahedron (soccer ball) has three primary vertices

$$v_0 \;=\; (0,\,1,\,3\varphi) \tag{5.29}$$
$$v_1 \;=\; (1,\,2+\varphi,\,2\varphi) \tag{5.30}$$
$$v_2 \;=\; (\varphi,\,2,\,2\varphi+1), \tag{5.31}$$

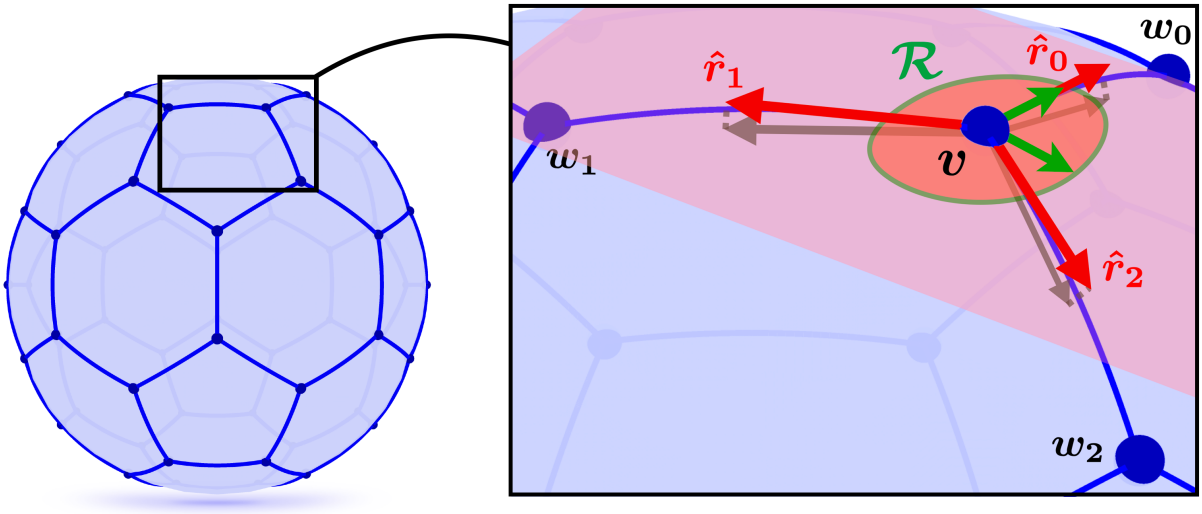

Figure 5.5: The truncated icosahedron (bottom left) is embedded within the 2-sphere S^2. The edge tensor R acts on the tangent space of S^2, with the principle eigenvector (green) along the edge (red) opposite the local pentagonal face.

where φ is the golden ratio $\varphi = (1+\sqrt{5})/2$. These vertices are all a distance from the origin $|v| = \sqrt{10+9\varphi}$. We eventually work with all vertices embedded in the unit sphere, but the non-normalised versions simplify the presentation until that point. Eventually, we envisage the edges embedded as segments of great circles within the unit sphere. The other vertices (60 in total) generate from the primary three by all combinations of cyclically permuting the coordinates, $\varpi : (x,y,z) \to (z,x,y)$, and reflecting the set across all coordinate planes $\rho_x : x \to -x$ with $\rho_y = \varpi\rho_x\varpi^2$, $\rho_z = \varpi^2\rho_x\varpi$. All vertices are connected by edges with three-dimensional Euclidean length $= 2$. Therefore $v_i \sim w_{i,j}$ where

$$v_0 \sim \{\rho_y v_0,\ \rho_x v_2,\ v_2\} \tag{5.32}$$
$$v_1 \sim \{\varpi^2 v_2,\ v_2,\ \rho_x v_1\} \tag{5.33}$$
$$v_2 \sim \{\varpi v_1,\ v_0,\ v_1\}. \tag{5.34}$$

Each vertex connects to three faces: two regular hexagons and one regular pentagon. For each vertex, v_i, the sets of neighbouring vertices are ordered such that the edge along $w_{i,0} - v_i$ is opposite the pentagonal face, and for $j = 1,2$, $w_{i,j} - v_i$ is opposite a hexagonal face. That is, the angle between the $j = 1,2$ edges is 108° and the angles between $j = 0$ and $j = 1,2$ are both 120°. Moreover, the $j = 1,2$ edges are ordered so that for the matrix formed by the columns $E_i = [w_{i,0} - v_i, w_{i,1} - v_i, w_{i,2} - v_i]$, $\det(E_i) = 4$ for all i.

Graph problem Because of the global edge length, the vertex condition at any vertex $v \sim \{w_1, w_2, w_3\}$ is simply

$$3\cos(k\ell)\, f(v) - (f(w_1) + f(w_2) + f(w_3)) \ = \ 0. \tag{5.35}$$

Therefore, if A is the adjacency matrix of the graph, then we can express the NEP $L(k)f(V) = 0$ as

$$(A - \lambda I)f(V) \;=\; 0 \tag{5.36}$$

where $\lambda = 3\cos(k\ell)$. The soccer ball has a manageable total adjacency structure. The characteristic polynomial of A is

$$\begin{aligned}\det(A - \lambda\, I) \;=\;& (\lambda - 3)(\lambda - 1)^9(\lambda + 2)^4 \\ & \times \left(\lambda^2 - \lambda - 3\right)^5 \left(\lambda^2 + \lambda - 4\right)^4 \\ & \times \left(\lambda^2 + \lambda - 1\right)^5 \left(\lambda^2 + 3\lambda + 1\right)^3 \\ & \times \left(\lambda^2 - (1+\varphi)\,\lambda - 2 + \varphi\right)^3 \\ & \times \left(\lambda^2 - (2-\varphi)\,\lambda - 1 - \varphi\right)^3 .\end{aligned} \tag{5.37}$$

If our continuum approximation is close to sensible, we should expect a rough correspondence for *low-degree modes* to the spherical harmonic eigenvalues rescaled inversely by the dimension

$$k^2 \;=\; \frac{\arccos(\frac{\lambda}{3})^2}{\ell^2} \;\approx\; \frac{j(j+1)}{2}, \tag{5.38}$$

with approximate multiplicities, $2j + 1$.

Continuum limit Here we construct the continuum limit by expressing approximations of the edge tensor and vertex density in closed forms in terms of spherical harmonics. Considering now all vertices and edges as embedded in the unit two-sphere, the connected vertices have the same mutual angle within $\mathbb{R}^3$. Therefore, the edge length is

$$\begin{aligned}\ell \;&=\; \arccos\left(\tfrac{w_{i,j}\cdot v_i}{|v|^2}\right) \\ &=\; \arccos(\tfrac{71+18\varphi}{109}) \;\approx\; 0.406338.\end{aligned} \tag{5.39}$$

If we had considered the edges as straight lines in $\mathbb{R}^3$, we would have instead $\ell = 2/|v| \approx 0.403548$, with a difference of less than 1%. Embedding the edges within the unit $2-$sphere amounts to projecting the vectors pointing between vertices into the local tangent plane at a point

$$\hat{r}_{i,j} \;=\; \csc(\ell)\,\hat{w}_{i,j} - \cot(\ell)\,\hat{v}_i, \tag{5.40}$$

where $\hat{v}_i = v_i/|v|$ and $\hat{w}_{i,j} = w_{i,j}/|v|$. The edge vector has both properties that $\hat{r}_{i,j}\cdot\hat{v}_i = 0$ and $\hat{r}_{i,j}\cdot\hat{r}_{i,j} = 1$. At vertex v_i

$$\hat{R}(\hat{v}_i) \;=\; \frac{1}{3}\sum_j \hat{r}_{i,j}\otimes\hat{r}_{i,j}, \tag{5.41}$$

where without loss of generality $\mathrm{tr}(\hat{R}(v_i)) = 1$. We can divide the trace out of the problem because it is constant at all vertices (*i.e.*, 3ℓ). At each vertex, by definition

$$\hat{R}(\hat{v}_i) \cdot \hat{v}_i \;=\; 0. \tag{5.42}$$

Also, by construction, we order the set of neighbouring vertices so that $\hat{r}_{i,0}$ is opposite from the pentagon face so that

$$\hat{R}(\hat{v}_i) \cdot \hat{r}_{i,0} \;=\; \frac{1+\varepsilon}{2}\,\hat{r}_{i,0}, \tag{5.43}$$

where

$$\varepsilon \;=\; \frac{17-9\varphi}{27} \;\approx\; 0.090285. \tag{5.44}$$

Finally, we have

$$\hat{R}(\hat{v}_i) \cdot (\hat{v}_i \times \hat{r}_{i,0}) \;=\; \frac{1-\varepsilon}{2}\,(\hat{v}_i \times \hat{r}_{i,0}). \tag{5.45}$$

The eigenvalues of $\hat{R}$ are uniform at all vertices; only the eigenvectors (aligned with $w_{i,0} - v_i$) rotate from vertex to vertex. Therefore, restricting exclusively to the tangent space at a vertex

$$\hat{R}(\hat{v}) \;=\; \frac{1}{2}(I + \varepsilon\, S(\hat{v})), \tag{5.46}$$

where I is the two-dimensional identity operator and $S(\hat{v})$ has eigenvalues ± 1 at the vertices. Amusingly, $\hat{R}(\hat{v})$ has exactly the same form as a spin-1/2 quantum density matrix at each of the vertices. Locally,

$$S(\hat{v}_i) \;=\; \hat{r}_{i,0} \otimes \hat{r}_{i,0} - (\hat{v}_i \times \hat{r}_{i,0}) \otimes (\hat{v}_i \times \hat{r}_{i,0}). \tag{5.47}$$

Because $S(\hat{v})$ is traceless and symmetric, it contains only spin-(± 2) components

$$S(\hat{v}) \;=\; S_{++}(\theta,\phi)\, e_+ \otimes e_+ + \text{c.c.}, \tag{5.48}$$

where $e_+ = (e_\theta - i e_\phi)/\sqrt{2}$. We can fit $S_{++}(\theta,\phi)$ to a series of spin-2 spherical harmonics. Given that any number of spherical harmonic series will vanish at 60 given vertices, the result is far from unique. We pick the solution having the minimum square integral that exactly reproduces the known vertex values (figure 5.6(a)). A spherical harmonic degree $j = 6$ solution exists with a series of even values of $|m| \le 6$. In standard spherical coordinates (θ,ϕ),

$$S \;=\; S_{\theta\theta}\,(e_\theta \otimes e_\theta - e_\phi \otimes e_\phi) + S_{\theta\phi}\,(e_\theta \otimes e_\phi + e_\phi \otimes e_\theta). \tag{5.49}$$

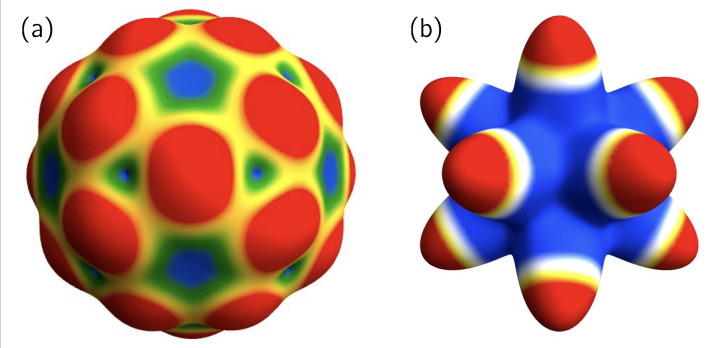

Figure 5.6: Soccer ball edge tensor and vertex density interpolations. (a) Surface showing the largest local eigenvalue of R, *i.e.*, $1 + \varepsilon\sqrt{\mathrm{tr}(S^2)\,/2}$. (b) Surface illustrating the μ_6 vertex density truncation.

Define $z = \cos(\theta)$, then

$$S_{\theta\theta} = \sum_{k=0}^{3} a_k\, P_{k,0}(z)\cos(2k\phi), \tag{5.50}$$

$$S_{\theta\phi} = \sum_{k=1}^{3} a_k\, P_{k,1}(z)\sin(2k\phi). \tag{5.51}$$

By definition $S_{\phi\phi} = -S_{\theta\theta}$ and $S_{\phi\theta} = S_{\theta\phi}$. The polynomials P are

$$P_{0,0}(z) = \frac{15}{16}\left(1-z^2\right)\left(1-18z^2+33z^4\right), \tag{5.52}$$

$$P_{1,0}(z) = \frac{1}{16}\left(-17+289z^2-735z^4+495z^6\right), \tag{5.53}$$

$$P_{2,0}(z) = \frac{1}{2}\left(1-z^2\right)\left(1-10z^2+33z^4\right), \tag{5.54}$$

$$P_{3,0}(z) = \left(1-z^2\right)\left(1-z^4\right). \tag{5.55}$$

$$P_{1,1}(z) = -\frac{z}{8}\left(37-186z^2+165z^4\right), \tag{5.56}$$

$$P_{2,1}(z) = 2z\left(1-z^2\right)\left(5-11z^2\right), \tag{5.57}$$

$$P_{3,1}(z) = -2z\left(1-z^2\right)^2. \tag{5.58}$$

The coefficients are

$$\begin{aligned} a_0 &= \tfrac{-1363+\ 332\,\varphi}{3840} &&\approx -0.215055,\\ a_1 &= \tfrac{2027-2394\,\varphi}{2560} &&\approx -0.721318,\\ a_2 &= \tfrac{1363-\ 332\,\varphi}{2048} &&\approx\ \ 0.403229,\\ a_3 &= \tfrac{-6081+7182\,\varphi}{8192} &&\approx\ \ 0.676235. \end{aligned} \tag{5.59}$$

The polynomials are the even/odd components of the scaled standard Jacobi polynomials,

$$P_{k,0}(z) \;=\; \frac{\mathcal{P}_k(z)+\mathcal{P}_k(-z)}{2}, \tag{5.60}$$

$$P_{k,1}(z) \;=\; \frac{\mathcal{P}_k(z)-\mathcal{P}_k(-z)}{2}, \tag{5.61}$$

where

$$\mathcal{P}_k(z) = (1-z)^{\alpha}(1-z)^{\beta}P_{2n}^{(2\alpha,2\beta)}(z), \tag{5.62}$$

where $n = \min(3-k,2)$, $\alpha = |k+1|$, $\beta = |k-1|$.

For the vertex density, we start with the formal empirical measure,

$$\mu(\hat{x}) \;=\; \sum_{\hat{v}\in V}\delta(\hat{x}-\hat{v}) \tag{5.63}$$

From the completeness of the spherical harmonic basis,

$$\delta(\hat{x}-\hat{v}) \;=\; \sum_{j\geq 0}\sum_{|m|\leq j} Y_{j,m}(\hat{x})Y_{j,m}(\hat{v}). \tag{5.64}$$

Therefore, we can define a smooth truncated measure,

$$\mu_J(\hat{x}) \;=\; \sum_{j=0}^{J}\sum_{|m|\leq j} Y_{j,m}(\hat{x})\sum_{\hat{v}\in V} Y_{j,m}(\hat{v}), \tag{5.65}$$

We do not have $\mu_J(\hat{x}) \geq 0$ for all J sufficiently large. Pragmatically, we choose J where the measures agree well enough, and both are positive. Given the purely $j=6$ nature of the $S(\hat{x})$ interpolation, we accordingly use a $J=6$ truncation of the vertex density measure. This approximation will not give accurate results for high-degree PDE modes but will capture reasonable behaviour as a proof of concept for PDE eigenmodes $j \leq 3$. It also happens that $j=6$ is the simplest non-trivial density given the coefficients

$$\sum_{\hat{v}\in V} Y_{j,m}(\hat{v}) \;=\; 0 \qquad 1\leq j\leq 5. \tag{5.66}$$

Therefore, given the global average density $|V|/(4\pi) = 15/\pi$,

$$\mu_6 \;=\; \frac{15}{\pi}\left(1+\sum_{k=0}^{3} b_k\, Q_k(z)\,\cos(2k\phi)\right), \tag{5.67}$$

as illustrated in figure 5.6(b), where

$$\begin{aligned} b_0 &= -\tfrac{143(-77431+60480\,\varphi)}{20720464} \approx -0.140979, \\ b_1 &= -\tfrac{1001(198391-94382\,\varphi)}{207204640} \approx -0.721318, \\ b_2 &= \tfrac{1001(-77431+60480\,\varphi)}{165763712} \approx 0.123357, \\ b_3 &= \tfrac{3003(198391-94382\,\varphi)}{663054848} \approx 0.206876, \end{aligned} \tag{5.68}$$

and

$$Q_0(z) = \frac{1}{16}\left(-5+105z^2-315z^4+231z^6\right), \tag{5.69}$$

$$Q_1(z) = \frac{15}{16}\left(1-z^2\right)\left(1-18z^2+33z^4\right), \tag{5.70}$$

$$Q_2(z) = \frac{3}{2}\left(1-z^2\right)^2\left(-1+11z^2\right), \tag{5.71}$$

$$Q_3(z) = \left(1-z^2\right)^3. \tag{5.72}$$

With the expansions of the edge tensor eq. (5.46) and vertex density eq. (5.67) in hand, we compute the spectrum for the continuum limit using spin-weighted spherical harmonics [129]. The eventual spectral discretization of the continuum limit eq. (2.42) is eq. (5.82). We first expand the solution in terms of a traditional scalar series,

$$f(\theta,\phi) = \sum_{|m|\le L_{\max}} Y_m^0(\theta,\phi)\cdot F_m. \tag{5.73}$$

For each m, we encapsulate the full range of spherical harmonic degrees as row vectors,

$$Y_m^s = \left[Y^s_{|m|\wedge|s|,m},\,\ldots,\,Y^s_{L_{\max},m}\right], \tag{5.74}$$

For each m, F_m is a column vector representing the expansion coefficients. The gradient decomposes in terms of spin-(±1) series',

$$\nabla f = \sum_{|m|\le L_{\max}} e_+\, Y_m^+\cdot\mathcal{D}_0^+\cdot F_m + \sum_{|m|\le L_{\max}} e_-\, Y_m^-\cdot\mathcal{D}_0^-\cdot F_m. \tag{5.75}$$

The perturbation to the graph matrix is degree-6 spin-(±2) series,

$$S = \sum_{|n|\le 6} e^{in\phi}\, S_n(\theta)\, e_+\otimes e_+ + \sum_{|n|\le 6} e^{in\phi}\, S_{-n}(\theta)\, e_-\otimes e_-, \tag{5.76}$$

where the terms vanish. We promote the non-constant coefficient terms to matrix operators by the intertwining conditions,

$$S_n(\theta)e^{in\phi}\,Y_m^-(\theta,\phi) = Y_{m+n}^+(\theta,\phi)\cdot\mathcal{S}^{+2}_{n,m} \tag{5.77}$$

$$S_{-n}(\theta)e^{in\phi}\,Y_m^+(\theta,\phi) = Y_{m+n}^-(\theta,\phi)\cdot\mathcal{S}^{-2}_{-n,m}. \tag{5.78}$$

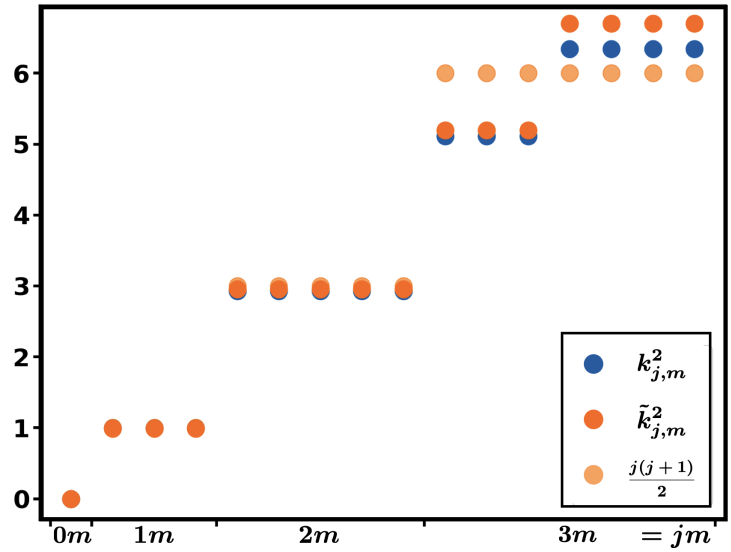

Figure 5.7: The graph eigenvalues $k^2_{j,m}$ track the PDE eigenvalues $\tilde{k}_{j,m}$, including splittings and multiplicities, even when discreteness effects are far from negligible.

Finally, for a term such as

$$\nabla \cdot (S \cdot \nabla f) = \sum_{|n| \leq 6, m} Y^0_{m+n} \cdot \mathrm{S}_{n,m} \cdot F_m, \tag{5.79}$$

where,

$$\mathrm{S}_{n,m} \;=\; \mathcal{D}^-_+ \cdot \mathcal{S}^{+2}_{n,m} \cdot \mathcal{D}^-_0 + \mathcal{D}^+_- \cdot \mathcal{S}^{-2}_{-n,m} \cdot \mathcal{D}^+_0 . \tag{5.80}$$

Matrices of this form compose the block elements of a larger system that gives a total matrix for computing numerical eigenvalues. Action by μ_6 happens similarly,

$$M_n(\theta) e^{in\phi}\, Y^0_m(\theta, \phi) \;=\; Y^0_{m+n}(\theta, \phi) \cdot \mathcal{M}_{n,m} \tag{5.81}$$

Overall, we solve the system as a generalised eigenvalue problem

$$\nabla \cdot (\mu_6\, R \cdot \nabla f) \;=\; -k^2\, \mu_6\, f, \tag{5.82}$$

where $\mathrm{tr}(R) = 1$ globally. We solve the PDE model with an updated version of the low-level spectral libraries of the Dedalus framework [129–131]. We test convergence as a function of the total spherical harmonic degree, $L_{\max} = 10, 20, 30$, finding convergence to at least six decimal digits for up to 60 eigenvalues. Table 5.1 shows the numerical values of the exact graph eigenvalues and the closest corresponding homogeneous sphere modes and their degeneracies. It is clear that there is rough agreement for modes with $j \leq 4$; much less so for the rest of the spectrum. Figure 5.7 shows the eigenvalue results for $j \leq 3$. As a benchmark, the eigenvalues of the leading-order homogeneous approximation are $\lambda_{j,m} = j(j+1)/2$ with $2j+1$ multiplicity. The truncated icosahedron allows exact eigenvalue solutions derived from eq. (2.16)–the equal edge lengths reduce the condition on the system over V to a simple requirement on the adjacency matrix of the graph, analogous to the condition for protonated methane in [12]. The PDE eigenvalues $\tilde{k}_{j,m}$

j	$2j+1$	$\frac{j(j+1)}{2}$	(graph k^2 : multiplicity)	(PDE k^2 : multiplicity)
0	1	0	$(0:1)$	$(0:1)$
1	3	1	$(0.996368:3)$	$(0.991754:3)$
2	5	3	$(2.93154:5)$	$(2.95478:5)$
3	7	6	$(5.11325:3)$, $(6.34256:4)$	$(5.19583:3)$, $(6.69731:4)$
4	9	10	$(9.17726:9)$	$(9.79458:5)$, $(10.5638:4)$
5	11	15	$(11.2566:5)$, $(15.8360:3)$, $(17.4718:3)$	$(14.7910:3)$, $(15.0616:5)$, $(15.5677:3)$
6	13	21	$(24.7134:5)$, $(25.9717:3)$, $(27.7484:5)$	$(20.7003:3)$, $(21.1952:4)$, $(21.2481:5)$ $(21.4194:1)$
7	15	28	$(32.0538:4)$, $(40.7578:4)$, $(41.939:3)$, $(80.765:3)$, $(82.424:1)$	$(27.9324:5)$, $(28.0045:4)$, $(28.2498:2)$

Table 5.1: a summary of (60 total) graph and PDE eigenvalues with their closest corresponding homogeneous spherical analogues. Figure 5.7 shows a comparison plot for $j \leq 3$.

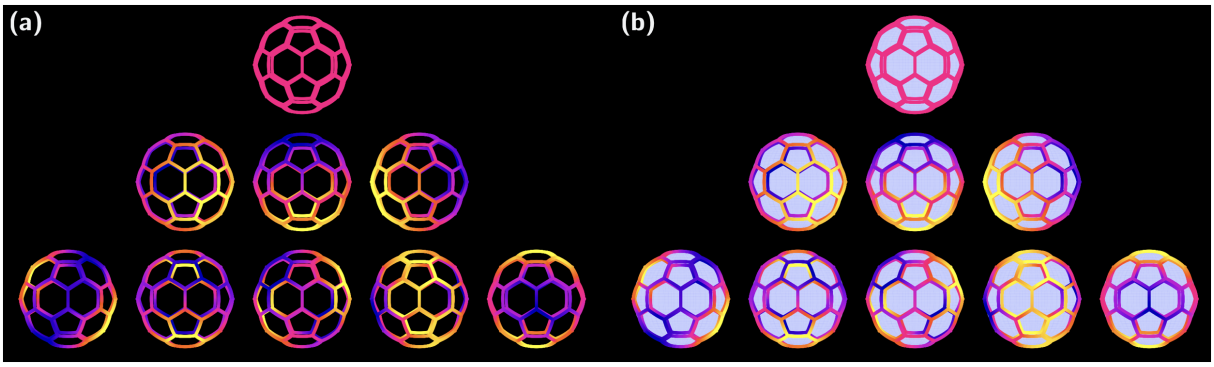

Figure 5.8: (a) graph eigenmodes & graph-restricted PDE eigenmodes respectively with rows $= j$, columns $= m$ for $|m| \leq j \leq 2$.

track the $2j + 1$ groupings of graph eigenvalues. Figures 5.8a-b show visual comparisons between the graph and (graph-restricted) PDE modes.

In summary, we have given

Chapter 6

Homogenization of local breakdown of the continuum limit: periodic graphs

So far, the graphs we have studied have had smoothly interpolable edge tensors and vertex densities, oscillating only over large scales. The lattices in the introductory examples had constant graph quantities, and the semi-analytical examples of the previous chapter had closed forms or rapidly converging series approximations. However, many real-world networks of interest contain not only noise, but deterministic variations in structure at the scale of our limiting approximations. Fluctuations of $\mathcal{O}(\ell^2)$ in μ and/or $\mathcal{O}(\ell)$ in R at the scale of edge lengths cause a break down in the PDE.

6.1 Motivating example

Figure 6.1 shows the periodic hexagonal graph from figure 4.17, and a periodic truncated square graph (so named because the octagonal faces are squares with "truncated" corners). Despite having two sets of non-identical neighbourhoods in V_W and V_E, the periodic hexagonal graph has a constant edge tensor $R = 3\ell I$. This is not so for the truncated square (figure 6.1b). Its vertices are generated from four basis vertices v_N, v_S, v_E, v_W and lattice vectors $e_1 = (1+\sqrt{2})\ell e_x$ and $e_2 = (1+\sqrt{2})\ell e_y$. The basis vertices are arranged in a diamond shape and connected so that each has degree 3, and all edges have length ℓ. For the R tensor, define $r(j) = (\cos j\pi/4, \sin j\pi/4)$. Then at each basis vertex we have:

$$R(v_N) = \frac{1}{\ell}\left(r(2)\otimes r(2) + r(5)\otimes r(5) + r(7)\otimes r(7)\right) = \ell\begin{pmatrix}1 & 0\\ 0 & 2\end{pmatrix} \tag{6.1}$$

$$R(v_S) = \frac{1}{\ell}\left(r(1)\otimes r(1) + r(3)\otimes r(3) + r(6)\otimes r(6)\right) = \ell\begin{pmatrix}1 & 0\\ 0 & 2\end{pmatrix} \tag{6.2}$$

$$R(v_E) = \frac{1}{\ell}\left(r(0)\otimes r(0) + r(3)\otimes r(3) + r(5)\otimes r(5)\right) = \ell\begin{pmatrix}2 & 0\\ 0 & 1\end{pmatrix} \tag{6.3}$$

$$R(v_W) = \frac{1}{\ell}\left(r(1)\otimes r(1) + r(4)\otimes r(4) + r(7)\otimes r(7)\right) = \ell\begin{pmatrix}2 & 0\\ 0 & 1\end{pmatrix} \tag{6.4}$$

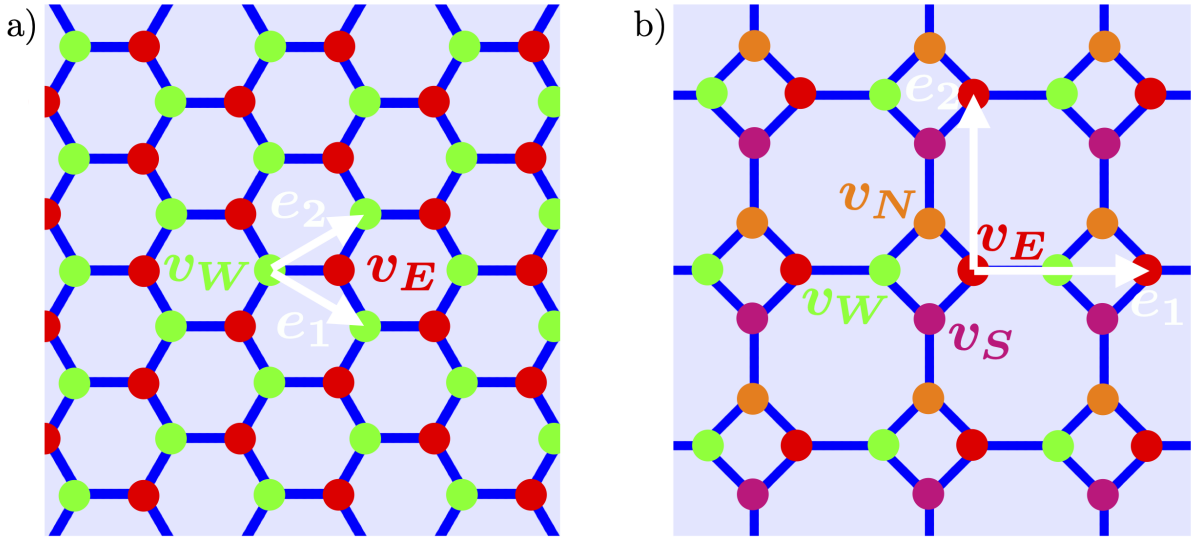

Figure 6.1: The periodic hexagonal (a) and truncated square (b) graphs are constructed both have multiple types of vertex neighbourhoods. While the hexagonal lattice has a constant R tensor, the truncated square graph's R tensor fluctuates to order ℓ between neighbouring vertices.

Therefore, R takes two distinct values

$$R(v_N) \;=\; R(v_S) \;=\; \ell \begin{pmatrix} 1 & 0 \\ 0 & 2 \end{pmatrix} \qquad , \qquad R(v_E) \;=\; R(v_W) \;=\; \ell \begin{pmatrix} 2 & 0 \\ 0 & 1 \end{pmatrix} . \tag{6.5}$$

This is an $\mathcal{O}(\ell)$ oscillation in R at the scale of vertex neighbours. Even if one were to determine a differentiable interpolation of this at some finite graph density, it would make solving the problem, even numerically, prohibitively inefficient. Furthermore, as we are about to determine, R does not simply average out, for example, to

$$R(v) \;=\; \ell \begin{pmatrix} \frac{3}{2} & 0 \\ 0 & \frac{3}{2} \end{pmatrix} \pm \ell \begin{pmatrix} \frac{1}{2} & 0 \\ 0 & -\frac{1}{2} \end{pmatrix} \;\to\; \ell \begin{pmatrix} \frac{3}{2} & 0 \\ 0 & \frac{3}{2} \end{pmatrix} . \tag{6.6}$$

The explicit NEP solution demonstrates that this averaging is incorrect. As with the introductory examples, consider plane wave solutions of the NEP

$$f(v) \;=\; A e^{i\kappa\cdot v} + \text{c.c.} \tag{6.7}$$

where $v = ae_1 + be_2$ for integers a, b and $\kappa = \kappa_1 \tilde{e}_1 + \kappa_2 \tilde{e}_2$ for $e_i \cdot \tilde{e}_j = \|e_i\| \delta_{ij} = (1+\sqrt{2})\ell\delta_{ij}$. Then proceeding exactly as for the hexagonal graph in eq. (4.57), the vertex condition at each basis vertex forms the system

$$\begin{pmatrix} -3\cos(k\ell) & e^{i(1+\sqrt{2})\ell\kappa_2} & 1 & 1 \\ e^{-i(1+\sqrt{2})\ell\kappa_2} & -3\cos(k\ell) & 1 & 1 \\ 1 & 1 & -3\cos(k\ell) & e^{i(1+\sqrt{2})\ell\kappa_1} \\ 1 & 1 & e^{-i(1+\sqrt{2})\ell\kappa_1} & -3\cos(k\ell) \end{pmatrix} \begin{pmatrix} f_N \\ f_S \\ f_E \\ f_W \end{pmatrix} \;=\; 0. \tag{6.8}$$

Setting the determinant to 0 we obtain the dispersion relation

$$\frac{35}{8}+\frac{27}{2}\cos(2k\ell)+\frac{81}{8}\cos(4k\ell)-12\cos(k\ell)(\cos(\kappa_1\ell)+\cos(\kappa_2\ell))-4\cos(\kappa_1\ell)\cos(\kappa_2\ell) \;=\; 0. \tag{6.9}$$

To leading order as $\ell \to 0$, this becomes

$$k^2 \;=\; \frac{(1+\sqrt{2})^2}{6}\left(\frac{1}{2}(\kappa_1^2+\kappa_2^2)\right)+\mathcal{O}\big(\ell^2\big)\,. \tag{6.10}$$

This is the dispersion relation of the homogeneous periodic graphs in the introductory examples (chapter 4), with an anomalous factor of $\frac{(1+\sqrt{2})^2}{6} \approx 0.9714$. This factor represents the effect of the periodic, small-scale fluctuations of the graph structure on the macroscale continuum limit.

6.1.1 Perturbation of NEP

While we cannot solve for the continuum limit with our PDE in its current form, we can get a sense of how homogenization works in a special case by solving eq. (6.8) perturbatively before taking the direct determinant. Expressing it as $Lf(V) = 0$, then we formally expand L as

$$L = L_0 + \ell\, L_1 + \ell^2\, L_2 + \mathcal{O}(\ell^3), \tag{6.11}$$

where

$$L_0 = \begin{pmatrix} -3 & 1 & 1 & 1 \\ 1 & -3 & 1 & 1 \\ 1 & 1 & -3 & 1 \\ 1 & 1 & 1 & -3 \end{pmatrix}, \tag{6.12}$$

$$L_1 = i\begin{pmatrix} 0 & \kappa_2 & 0 & 0 \\ -\kappa_2 & 0 & 0 & 0 \\ 0 & 0 & 0 & \kappa_1 \\ 0 & 0 & -\kappa_1 & 0 \end{pmatrix}, \tag{6.13}$$

$$L_2 = \tfrac{1}{2}\begin{pmatrix} 3k^2 & -\kappa_2^2 & 0 & 0 \\ -\kappa_2^2 & 3k^2 & 0 & 0 \\ 0 & 0 & 3k^2 & -\kappa_1^2 \\ 0 & 0 & -\kappa_1^2 & 3k^2 \end{pmatrix}. \tag{6.14}$$

For each of the $j \in \{N, S, E, W\}$ elements,

$$f_j = f_j^{(0)} + \ell\, f_j^{(1)} + \ell^2\, f_j^{(2)} + \mathcal{O}(\ell^3). \tag{6.15}$$

For the leading order, L_0 is a proper discrete Laplacian with $L_0 f^{(0)} = 0$. The Laplacian has a constant null vector. Therefore, for $j \in \{N, S, E, W\}$, $f_j^{(0)} = \hat{F}$ for an arbitary

amplitude, $\hat{F}$. All $NSEW$ components are equal to leading order. At the next order,

$$L_0 \cdot f^{(1)} + L_1 \cdot f^{(0)} = 0. \tag{6.16}$$

The system is solvable because $f^{(0)} \cdot L_1 \cdot f^{(0)} = 0$, but not uniquely. The solution with $f^{(1)} \cdot f^{(0)} = 0$,

$$f^{(1)} = \frac{i\hat{F}}{4} \begin{pmatrix} +\kappa_2 \\ -\kappa_2 \\ +\kappa_1 \\ -\kappa_1 \end{pmatrix}. \tag{6.17}$$

Finally,

$$L_0 \cdot f^{(2)} + L_1 \cdot f^{(1)} + L_2 \cdot f^{(0)} = 0. \tag{6.18}$$

The solvability conditon results in

$$f^{(0)} \cdot \left(L_1 \cdot f^{(1)} + L_2 \cdot f^{(0)}\right) = 0, \tag{6.19}$$

$$k^2 = \frac{\gamma^2}{12}(\kappa_x^2 + \kappa_y^2) \tag{6.20}$$

as expected.

Altogether, this exercise suggests a particular strategy for the periodic homogenization for metric graphs in the next section. The expression we find for each entry $f_j^{(1)}$ of $f^{(1)}$ is of the form

$$f_j^{(1)} \approx \alpha_j \cdot \nabla f_j^{(0)}, \tag{6.21}$$

suggesting an initial expansion for each component f_j in eq. (6.15) as

$$f_j = f_j^{(0)} + \ell \alpha_j \cdot \nabla f_j^{(0)} + \mathcal{O}\left(\ell^2\right). \tag{6.22}$$

Solving eq. (6.16) is then a matter of performing least squares with respect to the α's, either in the form of this equation, or at the level of its corresponding bilinear form.

6.2 Periodic homogenization

Here we present the standard homogenization procedure (c.f. [132]) for the following Sturm-Liouville problem on some bounded domain $M \subset \mathbb{R}^d$:

$$\nabla \cdot (K(x/\epsilon) \cdot \nabla u(x)) = \lambda u(x), \quad u = 0 \text{ on } \partial M. \tag{6.23}$$

This models steady heat conduction in a material with periodic microstructure with period $0 < \epsilon \ll 1$, assumed to be small with respect to the overall size of the domain. The macroscale variable is $x \in M$, while the microscale variable is $\xi = \frac{x}{\epsilon}$. The weight matrix (or thermal conductivity tensor) $K : T^d \to \mathbb{R}^{d \times d}$ is periodic in ξ (T^d is the torus). We

reflect the scale separation in the asymptotic expansion

$$u(x) = u_0(x,\xi) + \epsilon u_1(x,\xi) + \epsilon^2 u_2(x,\xi)\dots \tag{6.24}$$

where the $u_i : M \times T^d \to \mathbb{R}$ are also periodic in ξ. Define the multiple scales derivative

$$\nabla \;:=\; \nabla_x + \frac{1}{\epsilon}\nabla_\xi. \tag{6.25}$$

To leading order $\mathcal{O}(\epsilon^{-2})$ in eq. (6.23), we have

$$\nabla_\xi \cdot (K(\xi) \cdot \nabla_\xi u_0(x,\xi)) \;=\; 0, \tag{6.26}$$

and so

$$u_0(x,\xi) \;=\; u_0(x). \tag{6.27}$$

Applying this at $\mathcal{O}(\epsilon^{-1})$, we have

$$\nabla_\xi \cdot \Big(K(\xi) \cdot (\nabla_\xi u_1(x,\xi) + \nabla_x u_0(x))\Big) \;=\; 0. \tag{6.28}$$

Based on the linear dependence of u_1 on $\nabla_x u_0$, and that u_0 depends only on the macroscale variable x, we make the following ansatz

$$u_1(x,\xi) \;=\; \phi(\xi) \cdot \nabla_x u_0(x) \;=\; \sum_{i=1}^{d} \phi_i(\xi)\partial_i u_0(x). \tag{6.29}$$

for periodic ϕ. Substituing this back into eq. (6.28),

$$\sum_{i=1}^{d} \partial_{x_i} u_0(x)\Big(\nabla_\xi \cdot (K(\xi) \cdot (\nabla_\xi \phi_i(\xi) + e_i))\Big) \;=\; 0. \tag{6.30}$$

We obtain an equation for each component ϕ_i

$$\nabla_\xi \cdot (K(\xi) \cdot (\nabla_\xi \phi_i(\xi) + e_i)) \;=\; 0. \tag{6.31}$$

This is known as the *corrector equation* or *cell problem*, where the components ϕ_i are *homogenization correctors*. In general, these do not have explicit closed forms, and must be computed numerically. The $\mathcal{O}(1)$ problem is

$$\begin{aligned}&\nabla_\xi \cdot \Big(K(\xi) \cdot (\nabla_\xi u_2(x,\xi) + \nabla_x u_1(x,\xi))\Big) \\ &+ \nabla_x \cdot \Big(K(\xi) \cdot (\nabla_\xi u_1(x,\xi) + \nabla_x u_0(x))\Big) \;=\; \lambda u_0(x).\end{aligned} \tag{6.32}$$

The solvability condition comes from averaging over T^d. The first divergence term vanishes because it is periodic over T^d:

$$\begin{aligned}\int_{T^d} \nabla_\xi \cdot \Big(K(\xi) \cdot (\nabla_\xi u_2(x,\xi) + \nabla_x u_1(x,\xi))\Big) d\xi \\ = \int_{\partial T^d} \Big(K(\xi) \cdot (\nabla_\xi u_2(x,\xi) + \nabla_x u_1(x,\xi))\Big) \cdot \hat{n}(y) d\xi \\ = 0. \end{aligned} \tag{6.33}$$

The remaining terms in eq. (6.32) give for each ϕ_i

$$\nabla_x \cdot \Big(\langle K(\xi) \cdot (\nabla_\xi \phi_i(\xi) + e_i)\rangle \partial_{x_i} u_0(x)\Big) \;=\; \lambda u_0(x). \tag{6.34}$$

Now define the homogenized, constant $\overline{K}$ as

$$\overline{K} e_i \;=\; \langle K(\xi) \cdot (\nabla_\xi \phi_i(\xi) + e_i)\rangle \tag{6.35}$$

so that

$$\overline{K}_{ji} \;=\; \langle K(\xi) \cdot (\nabla_\xi \phi_i(\xi) + e_i)\rangle \cdot e_j. \tag{6.36}$$

Altogether

$$\nabla \cdot (\overline{K} \cdot \nabla u_0(x)) \;=\; \lambda u_0(x)\ , \quad u_0 = 0 \text{ on } \partial M. \tag{6.37}$$

This is the homogenized form of eq. (6.23). In multiple dimensions eq. (6.31) has no exact solutions in general. In one dimension we can integrate this equation and we explicitly get the harmonic mean of the tensor.

6.3 Metric graph homogenization

6.3.1 Homogenization procedure

In the above, we introduced homogenization for microscale, periodic structure in the form of a pre-defined tensor K. Here, we homogenize microscale, periodic graph structure in the construction of our R tensor from the standpoint of the bilinear (weak) form. That is, in general, we smoothly interpolate our R tensor Without loss of generality, we assumed toroidal periodicity at the microscale. Here, we generalise this to arbitrary cells in Euclidean space, as defined in chapter 4. For periodic graphs, we consider the partition of the vertex set $V = \bigcup_j V_j$ into subsets of connected basis vertices V_j. For the hexagonal and truncated square graphs above, the V_j are the subsets $\{v_E, v_W\}$ and $\{v_E, v_W, v_N, v_S\}$ respectively, along with their translations. In the bilinear form, we now consider a sum over every subset V_j, and every vertex $v \in V_j$. The double sum then becomes

$$\sum_{v\in V}\sum_{w\in V} \;=\; \sum_{V_i\subset V}\sum_{V_j\subset V}\sum_{v\in V_i}\sum_{w\in V_j}. \tag{6.38}$$

That is,

$$Q(f) \;=\; \sum_{V_i \subset V} \sum_{V_j \subset V} \sum_{v \in V_i} \sum_{w \in V_j} \frac{1}{\ell_{vw}} \left(f(v) - f(w)\right)^2 - k^2 \ell_{vw} f(v) f(w). \tag{6.39}$$

To separate scales, we express $f(v)$ as some function F of the centre x_i of the corresponding periodic Voronoi cell, displaced by some vector α_v to be determined:

$$f(v) \;=\; F(x_i + \alpha_v). \tag{6.40}$$

To first order,

$$F(x_i + \alpha_v) \;=\; F(x_i) + \alpha_v \cdot DF(x_i) + \mathcal{O}\left(\|\alpha_v\|^2\right), \tag{6.41}$$

for a macroscale gradient D. Therefore, in the bilinear form, we make the substitution

$$f(v) \;=\; F(x_i) + \alpha_v \cdot DF(x_i) \tag{6.42}$$

In the homogenization of eq. (6.23), we assumed

$$u(x) \;=\; u_0(x) + \epsilon \phi(\xi) \cdot \nabla_x u_0(x). \tag{6.43}$$

There is a natural correspondence between the vertex displacements α_v and the homogenization correctors ϕ. ϕ comes from solving eq. (6.31):

$$\nabla_\xi \cdot \left(K(\xi) \cdot \left(\nabla_\xi \phi_i(\xi) + e_i\right)\right) \;=\; 0. \tag{6.44}$$

In our problem, we construct a similar equation for the α components eqs. (6.57)–(6.58). First, substituting into the bilinear form, the difference term then becomes

$$f(v) - f(w) \;=\; F(x_i) + \alpha_v \cdot DF(x_i) - \left(F(x_j) + \alpha_w \cdot DF(x_j)\right). \tag{6.45}$$

We can express this purely in terms of $DF(x_i)$ by making the substitutions

$$F(x_j) \;=\; F(x_i) + r_{ij} \cdot DF(x_i) + \mathcal{O}\left(\|r_{ij}\|^2\right) \tag{6.46}$$

$$DF(x_j) \;=\; DF(x_i) + r_{ij} \cdot D^2 F(x_i) + \mathcal{O}\left(\|r_{ij}\|^2\right) \tag{6.47}$$

where $r_{ij} = x_j - x_i$. These r_{ij} are integer linear combinations of the lattice vectors of the periodic graph. Further, in our examples they are only sums because vertices are only connected to vertices within one translation in each direction. Assuming that $\|r_{ij}\| = \mathcal{O}\left(\|\alpha_v\|\right)$, then to leading order we have

$$f(v) - f(w) \;=\; \left(\alpha_v - \left(\alpha_w + r_{ij}\right)\right) \cdot DF(x_i) \tag{6.48}$$

The right-hand term in eq. (6.39) to leading order is

$$f(v) f(w) \;=\; F(x_i)^2. \tag{6.49}$$

Altogether

$$Q(f) \;=\; \sum_{V_i\subset V}\sum_{V_j\subset V}\sum_{v\in V_i}\sum_{w\in V_j}\frac{1}{\ell_{vw}}\left((\alpha_v-(\alpha_w+r_{ij}))\cdot DF(x_i)\right)^2 - k^2\ell_{vw}F(x_i)^2. \tag{6.50}$$

We now extremize with respect to each component $\alpha_v^{(n)}$ of the α_v vectors for each v and i. The dependent terms are

$$\left((\alpha_v-(\alpha_w+r_{ij}))\cdot DF(x_i)\right)^2 \;=\; DF(x_i)\cdot A_{ijvw}\cdot DF(x_i), \tag{6.51}$$

where $A_{ijvw} = a_{ijvw}\otimes a_{ijvw}$ and $a_{ijvw} = \alpha_v-(\alpha_w+r_{ij})$. In two dimensions, taking derivatives of A_{ijvw} w.r.t. the components $\alpha_v^{(1)}$ and $\alpha_v^{(2)}$, we obtain

$$\frac{\partial A_{ijvw}}{\partial\alpha_v^{(1)}} \;=\; \begin{pmatrix} 2a_{ijvw}^{(1)} & a_{ijvw}^{(2)} \\ a_{ijvw}^{(2)} & 0\end{pmatrix}, \quad \frac{\partial A_{ijvw}}{\partial\alpha_v^{(2)}} \;=\; \begin{pmatrix} 0 & a_{ijvw}^{(1)} \\ a_{ijvw}^{(1)} & 2a_{ijvw}^{(2)}\end{pmatrix} \tag{6.52}$$

where $a_{ijvw}^{(n)}$ is the nth component of a_{ijvw}. Contracting on both sides with $DF(x_i)$ and summing over all v,w, we obtain two independent conditions:

$$\frac{\partial Q(f)}{\partial\alpha_v^{(1)}} \;=\; 0 \qquad\Longrightarrow\qquad \sum_{w\sim v}\frac{1}{\ell_{vw}}a_{ijvw}^{(1)} \;=\; 0 \tag{6.53}$$

$$\frac{\partial Q(f)}{\partial\alpha_v^{(2)}} \;=\; 0 \qquad\Longrightarrow\qquad \sum_{w\sim v}\frac{1}{\ell_{vw}}a_{ijvw}^{(2)} \;=\; 0. \tag{6.54}$$

An important note is that we have only considered the explicit functions of the $\alpha_v^{(n)}$ components in the functional form of eq. (6.50). However, one vertex's w is another one's v. That is, for each edge e_{vw}, there are two terms in the bilinear form. However $A_{jiwv} = (-a_{ijvw})\otimes(-a_{ijvw}) = A_{ijvw}$. The two terms $DF(x_i)\cdot A_{ijvw}\cdot DF(x_i)$ and $DF(x_j)\cdot A_{ijvw}\cdot DF(x_j)$ we consider the same by making the leading order approximation $DF(x_j) = DF(x_i)+\mathcal{O}(\|r_{ij}\|)$. As a result, extremizing Q with respect to the α components only gives twice the sums eqs. (6.53)–(6.54). Explicitly, these give

$$\sum_{w\sim v}\frac{1}{\ell_{vw}}\left(\alpha_v^{(1)}-\alpha_w^{(1)}\right) \;=\; \sum_{w\sim v}\frac{1}{\ell_{vw}}r_{ij}^{(1)} \tag{6.55}$$

$$\sum_{w\sim v}\frac{1}{\ell_{vw}}\left(\alpha_v^{(2)}-\alpha_w^{(2)}\right) \;=\; \sum_{w\sim v}\frac{1}{\ell_{vw}}r_{ij}^{(2)} \tag{6.56}$$

and in matrix form over the whole graph

$$L\alpha^{(1)} \;=\; r^{(1)} \tag{6.57}$$

$$L\alpha^{(2)} \;=\; r^{(2)} \tag{6.58}$$

where $\alpha^{(1)}, \alpha^{(2)}$ are the vectors of components of the α_v's, $r^{(1)}, r^{(2)}$ are the vectors of the sums of components of each r_{ij}, and L is the $1/\ell_{vw}$-weighted graph Laplacian,

$$L_{vw} = \begin{cases} \sum_{w \sim v} \frac{1}{\ell_{vw}} & , \text{ if } w = v \\ -\frac{1}{\ell_{vw}} & , \text{ if } w \sim v \\ 0 & , \text{ otherwise,} \end{cases} \tag{6.59}$$

Equations (6.57)–(6.58) we refer to as the *graph* correction problem, by analogy with eq. (6.31) from standard homogenization theory. Laplacian matrices have a nullspace with dimension equal to the number of connected components of the graph. Indeed, for some connected component with vertices V, then the zero vector with ones at entries corresponding to each $v \in V$ spans the corresponding one-dimensional nullspace of L because $\sum_w L_{vw} = 0$ for each $v \in V$. In our case of a single connected component, the length $|V|$ vector $\mathbf{1}$ of ones is such that $L\mathbf{1} = 0$. On the RHS's of eqs. (6.57)–(6.58), each of $r^{(1)}, r^{(2)}$ are orthogonal to $\mathbf{1}$:

$$r^{(n)} \cdot \mathbf{1} = \sum_v \sum_{w \sim v} \frac{1}{\ell_{vw}} r_{ij}^{(n)} = 0. \tag{6.60}$$

As a result, we need an extra condition to fully specify the two systems for $\alpha^{(1)}, \alpha^{(2)}$. We choose the equilibrium condition (comprising one for each component)

$$\sum_v \alpha_v = 0. \tag{6.61}$$

In total, the homogenization of the bilinear form eq. (6.39) is

$$Q(F) = \sum_{V_i} \sum_{V_j} DF(x_i) \cdot \mathcal{R}(x_i) \cdot DF(x_i) - k^2 \mathcal{T}(x_i) F(x_i)^2 \tag{6.62}$$

where

$$\mathcal{R}(x_i) = \sum_{v \in V_i} \sum_{w \sim v} \frac{(\alpha_v - (\alpha_w + r_{ij})) \otimes (\alpha_v - (\alpha_w + r_{ij}))}{\ell_{vw}} \tag{6.63}$$

and

$$\mathcal{T}(x_i) = \sum_{v \in V_i} \sum_{w \sim v} \ell_{vw}. \tag{6.64}$$

6.4 Periodic hexagonal graph

We first apply homogenization to the periodic hexagonal graph (figure 6.1a)). Even though homogenization is not required in this case, it is an instructive first example of the procedure. We homogenize the R tensor within the unit cell of the vertex basis $V_i = \{v_W, v_E\}$. Assign the macroscale unit cell coordinate to be x_i. The relevant difference

terms in the bilinear form eq. (6.50) are

$$\begin{aligned} f(v_E) - f(v_W) &= (\alpha_W - \alpha_E) \cdot DF(x_i) && (6.65)\\ f(v_E) - f(v_W + e_1) &= (e_1 + \alpha_W - \alpha_E) \cdot DF(x_i) && (6.66)\\ f(v_E) - f(v_W + e_2) &= (e_2 + \alpha_W - \alpha_E) \cdot DF(x_i) && (6.67) \end{aligned}$$

and

$$\begin{aligned} f(v_W) - f(v_E) &= (\alpha_E - \alpha_W) \cdot DF(x_i) && (6.68)\\ f(v_W) - f(v_E - e_1) &= (-e_1 + \alpha_E - \alpha_W) \cdot DF(x_i) && (6.69)\\ f(v_W) - f(v_E - e_2) &= (-e_2 + \alpha_E - \alpha_W) \cdot DF(x_i). && (6.70) \end{aligned}$$

The bilinear form simplifies to

$$\begin{aligned} Q = 2 \sum_{V_i \subset V} \frac{1}{\ell} \Big[&((\alpha_W - \alpha_E) \cdot DF(x_i))^2 + ((e_1 + \alpha_W - \alpha_E) \cdot DF(x_i))^2 + ((e_2 + \alpha_W - \alpha_E) \cdot DF(x_i))^2 \\ &+ ((\alpha_E - \alpha_W) \cdot DF(x_i))^2 + ((-e_1 + \alpha_E - \alpha_W) \cdot DF(x_i))^2 + ((-e_2 + \alpha_E - \alpha_W) \cdot DF(x_i))^2 \Big] + k^2 \ell F(x_i)^2 \end{aligned} \tag{6.71}$$

where the sum is over all horizontally adjacent pairs West-East pairs in V. Solving for each α_j in the graph correction eqs. (6.57)–(6.58) gives

$$\alpha_W = \begin{pmatrix} -\frac{1}{2}\ell \\ 0 \end{pmatrix}, \quad \alpha_E = \begin{pmatrix} 0 \\ \frac{1}{2}\ell \end{pmatrix}. \tag{6.72}$$

In total, this gives

$$Q = 2 \sum_{V_i \subset V} DF(x_i) \cdot (3\ell I) \cdot DF(x_i) + k^2 \mathrm{tr}(3\ell I)\, F(x_i). \tag{6.73}$$

We therefore obtain $R = 3\ell I$, twice the $R = \frac{3}{2}\ell I$ we get from computing R directly (as in eq. (4.62)). Interestingly, the coefficients in eq. (6.72) place x_i at the centre of the edge connecting v_W and v_E, and the bilinear form eq. (6.73) is the bilinear form of the triangular graph–the dual of the hexagonal graph–where every vertex in figure 4.1 is connected to its six closest surrounding vertices. Overall, the factor of two is inconsequential, and the "homogenized" R tensor for the hexagonal lattice correctly produces the exact same eventual continuum limiting PDE.

6.5 Periodic truncated square graph

At the start of this chapter, we found that our PDE formulation was insufficient to capture the small-scale fluctuations (eq. (6.5)) in the R tensor of truncated square graph (figure 6.1b)). We solved the NEP to find an intruiging leading order dispersion relation

for $\ell \to 0$

$$k^2 \;=\; \frac{\gamma^2}{6}\left(\frac{1}{2}(\kappa_1^2+\kappa_2^2)\right). \tag{6.74}$$

where $\gamma = 1+\sqrt{2}$. Here, we homogenize the R tensor to produce the same result. Setting up the graph correction eqs. (6.57)–(6.58), we have

$$L \;=\; \frac{1}{\ell}\begin{pmatrix} 3 & -1 & -1 & -1 \\ -1 & 3 & -1 & -1 \\ -1 & -1 & 3 & -1 \\ -1 & -1 & -1 & 3 \end{pmatrix} \quad ; \quad r \;=\; \frac{1}{\ell}\begin{pmatrix} e_2^T \\ -e_2^T \\ e_1^T \\ -e_1^T \end{pmatrix}. \tag{6.75}$$

Therefore,

$$\begin{pmatrix} L \\ \mathbf{1}^T \end{pmatrix}\alpha \;=\; \begin{pmatrix} r \\ \mathbf{0}^T \end{pmatrix} \quad\Longrightarrow\quad \alpha \;=\; \frac{1}{4}\ell r \tag{6.76}$$

where the last row corresponds to the balance condition $\sum_{X\in\{N,S,E,W\}}\alpha(v_X)=0$. Substituting this into the bilinear form, we obtain

$$Q \;=\; 2\sum_{V_i\subset V} DF(x_i)\cdot\Big((1+\sqrt{2})^2\ell I\Big)\cdot DF(x_i) + 12\ell k^2 F(x_i)^2, \tag{6.77}$$

correctly resulting in

$$\frac{(1+\sqrt{2})^2}{6}\left(\frac{1}{2}\left(\frac{\partial^2}{\partial x^2}+\frac{\partial^2}{\partial y^2}\right)\right) f(x,y) \;=\; -k^2 f(x,y). \tag{6.78}$$

Numerical comparison between NEP and PDE Here we numerically verify eq. (6.78) as a continuum limit of the graph problem for increasing graph sizes. We embed the periodic truncated square graph in the square flat torus as in figure 6.2. In both the horizontal and vertical directions, we translate N copies of the square $\gamma\times\gamma$ Voronoi cell centered at the four basis vertices. Therefore $1 = N\gamma\ell$. For the NEP in 6.9, this quantizes the wave vector components via the relations

$$e^{i\kappa\cdot(v+Ne_1)} \;=\; e^{i\kappa\cdot v} \quad , \quad e^{i\kappa\cdot(v+Ne_2)} \;=\; e^{i\kappa\cdot v} \tag{6.79}$$

and so

$$N\kappa_1\gamma\ell \;=\; 2m\pi \;\Rightarrow\; \kappa_1 \;=\; 2m\pi \tag{6.80}$$

$$N\kappa_2\gamma\ell \;=\; 2n\pi \;\Rightarrow\; \kappa_2 \;=\; 2n\pi \tag{6.81}$$

for $0\le m,n\le N-1$. For the PDE eq. (6.78), we have standard plane wave solutions

$$F(x) \;=\; Ae^{i(\kappa_x x+\kappa_y y)} + \text{c.c.} \tag{6.82}$$

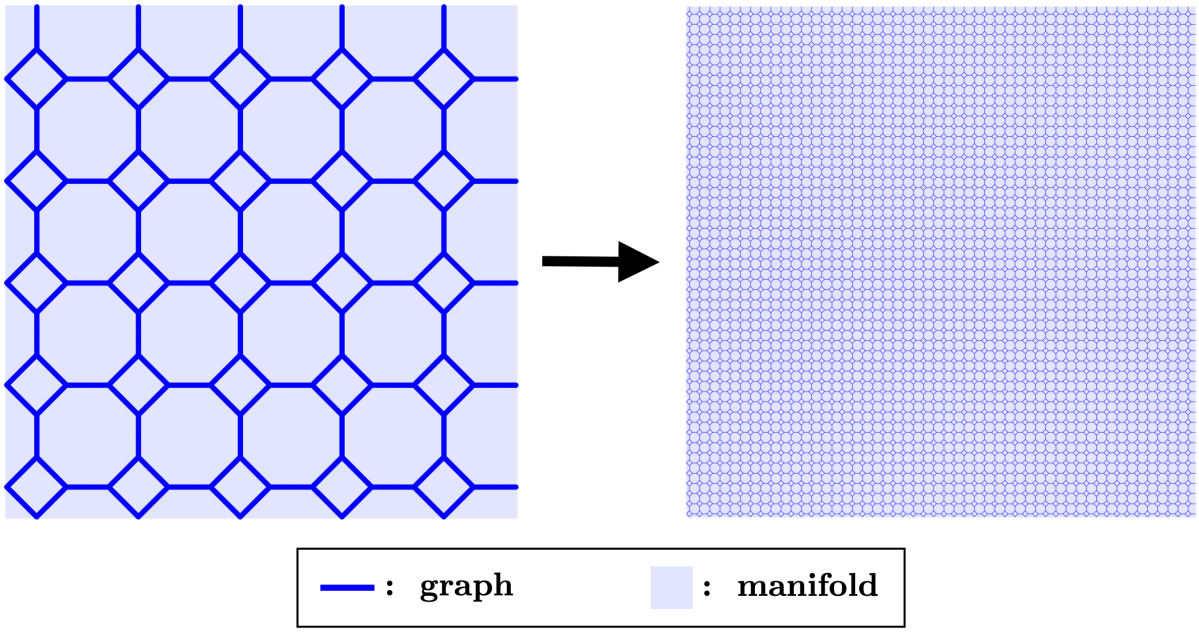

Figure 6.2: Illustration of the continuum limiting procedure for the periodic truncated square graph in the square flat torus.

for $\kappa_x = 2m\pi$, $\kappa_y = 2n\pi$ and $m, n \in \mathbb{N}$. The eigenvalues are

$$-k^2 \;=\; -\frac{(1+\sqrt{2})^2}{6}\left(\frac{1}{2}\left((2\pi m)^2 + (2\pi n)^2\right)\right). \tag{6.83}$$

As in the toroidal introductory examples, we compare solutions for $m, n \in \{0, 1, 2\}$. This has the same eigenfunction solutions as for the original square graph in the flat square torus on page 51. The eigenvalues are also those of table 4.1, rescaled by the factor $\gamma^2/6$. In figure 6.3 we show convergence of the graph to PDE eigensolutions for increasing graph densities. These results are as expected, except for the $\mathcal{O}(\ell)$ convergence in the eigenfunctions. We do not yet have an explanation for this convergence rate. An illustration of several graph and PDE eigenmodes is in figure 6.4.

6.6 Truncated trihexagonal graph

Here we present a more involved example of homogenization of a periodic graph. The purpose of this example is to give more intuition behind the homogenization process.

Setup The truncated trihexagonal graph is illustrated in figure 6.5. It presents a more involved example of a periodic graph requiring homogenization. Its vertices are those of the truncated trihexagonal lattice. As illustrated in figure 6.8, the truncated trihexagonal lattice is a multilattice consisting of the 12 vertices of a dodecagon (with side length ℓ)

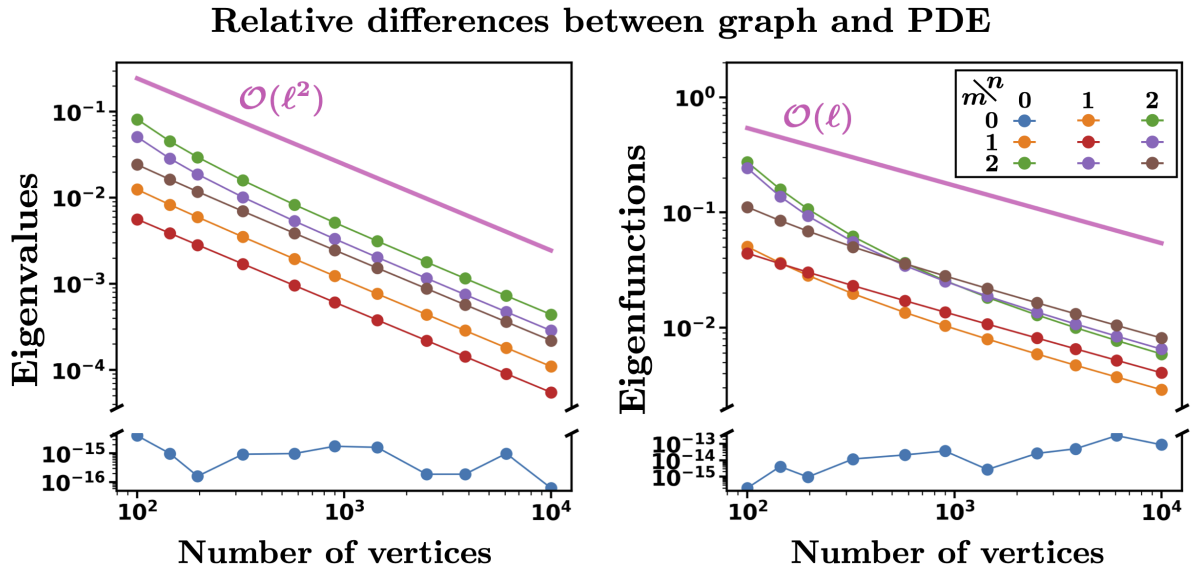

Figure 6.3: Convergence of NEP solutions to continuum limiting PDE solutions for periodic truncated square graphs of increasing densities in the flat square torus.

translated by the lattice vectors

$$e_1 = \ell\left(\frac{3}{2}\left(\sqrt{3}+1\right), \frac{1}{2}\left(\sqrt{3}+3\right)\right) \tag{6.84}$$

$$e_2 = \ell\left(\frac{3}{2}\left(\sqrt{3}+1\right), -\frac{1}{2}\left(\sqrt{3}+3\right)\right). \tag{6.85}$$

We construct the graph by connecting all vertices within a distance ℓ, resulting in all vertices having degree 3.

Graph problem To fill in the rectangular torus, we employ a similar procedure as for the hexagonal lattice. We choose a subset of vertices which can be translated periodically in orthogonal directions. In figure 6.7, we illustrate this procedure. We set up the graph problem as before for plave wave solutions $f_i(v) = A_i e^{i\kappa\cdot v} + \text{c.c.}$. Making the associations as in figure 6.6, we end up with the system:

$$\begin{pmatrix}
-\gamma & 1 & 0 & 0 & 0 & 0 & 0 & e^{i\kappa_1\ell} & 0 & 0 & 0 & 1 \\
1 & -\gamma & 1 & 0 & 0 & 0 & e^{i\kappa_1\ell} & 0 & 0 & 0 & 0 & 0 \\
0 & 1 & -\gamma & 1 & 0 & 0 & 0 & 0 & 0 & e^{i\ell(\kappa_1-\kappa_2)} & 0 & 0 \\
0 & 0 & 1 & -\gamma & 1 & 0 & 0 & 0 & e^{i\ell(\kappa_1-\kappa_2)} & 0 & 0 & 0 \\
0 & 0 & 0 & 1 & -\gamma & 1 & 0 & 0 & 0 & 0 & 0 & e^{-i\kappa_2\ell} \\
0 & 0 & 0 & 0 & 1 & -\gamma & 1 & 0 & 0 & 0 & e^{-i\kappa_2\ell} & 0 \\
0 & e^{-i\kappa_1\ell} & 0 & 0 & 0 & 1 & -\gamma & 1 & 0 & 0 & 0 & 0 \\
e^{-i\kappa_1\ell} & 0 & 0 & 0 & 0 & 0 & 1 & -\gamma & 1 & 0 & 0 & 0 \\
0 & 0 & 0 & e^{-i\ell(\kappa_1-\kappa_2)} & 0 & 0 & 0 & 1 & -\gamma & 1 & 0 & 0 \\
0 & 0 & e^{-i\ell(\kappa_1-\kappa_2)} & 0 & 0 & 0 & 0 & 0 & 1 & -\gamma & 1 & 0 \\
0 & 0 & 0 & 0 & 0 & e^{i\kappa_2\ell} & 0 & 0 & 0 & 1 & -\gamma & 1 \\
1 & 0 & 0 & 0 & e^{i\kappa_2\ell} & 0 & 0 & 0 & 0 & 0 & 1 & -\gamma
\end{pmatrix}
\begin{pmatrix} f_0 \\ f_1 \\ f_2 \\ f_3 \\ f_4 \\ f_5 \\ f_6 \\ f_7 \\ f_8 \\ f_9 \\ f_{10} \\ f_{11} \end{pmatrix} = 0$$

where $\gamma = 3\cos(k\ell)$. Setting the determinant to 0 gives the dispersion relation,

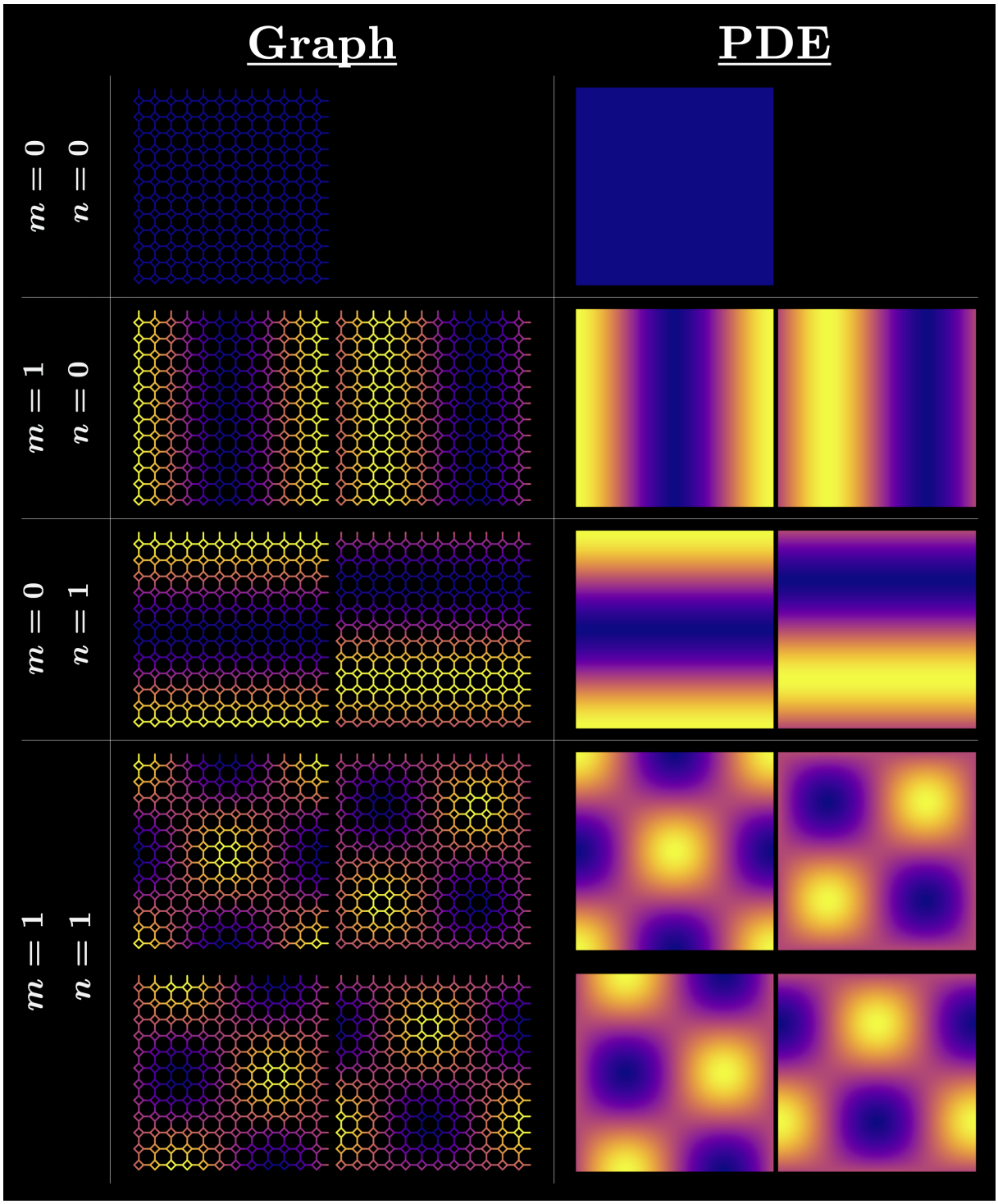

Figure 6.4: Visual comparison of eigenmodes of the NEP and PDE for the periodic truncated square graph in the flat square torus.

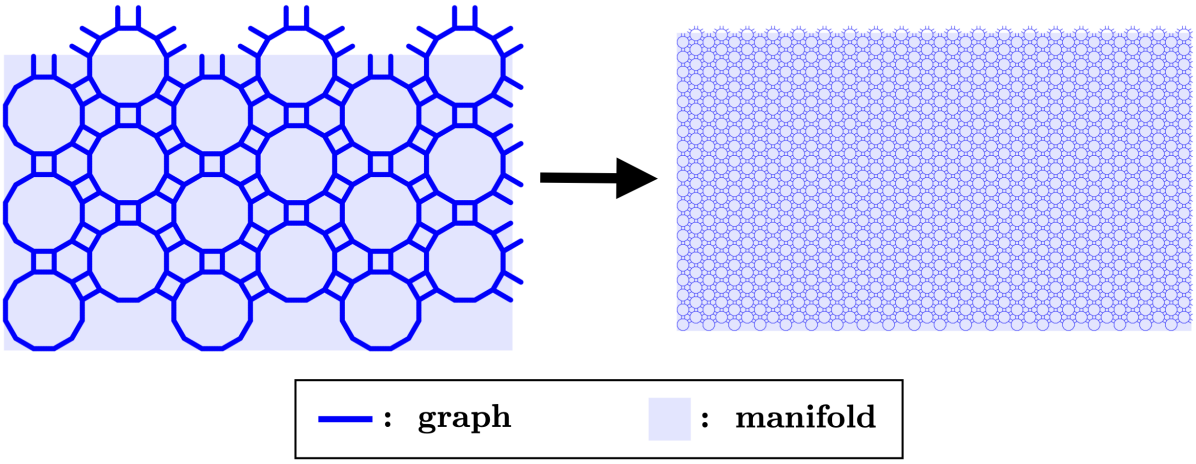

Figure 6.5: Illustration of the continuum limiting procedure for the truncated trihexagonal lattice in the $1 \times 1/\sqrt{3}$ rectangular flat torus.

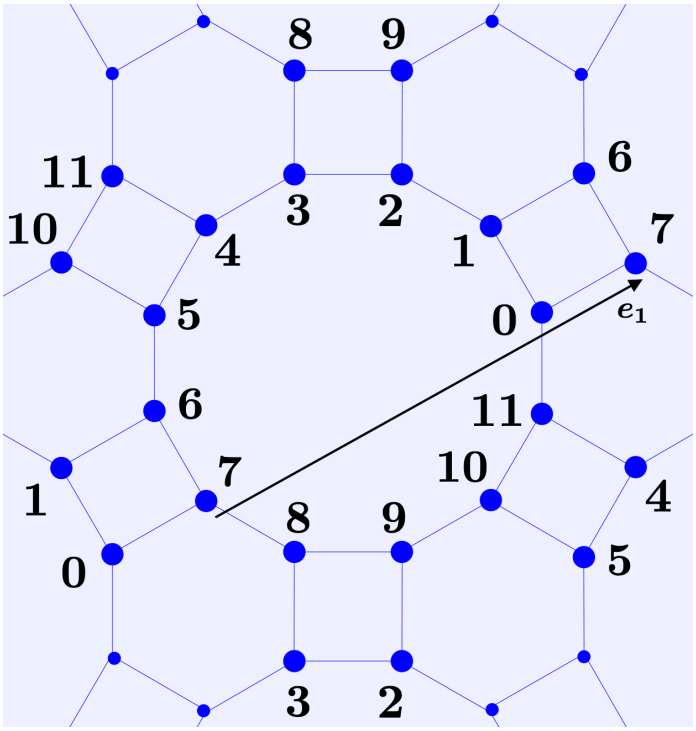

Figure 6.6: Vertex types of the truncated trihexagonal graph are defined by their sublattice membership. Vertices have one of types 0 through 11. We label the vertices of the dodecagon v_i for $i \in [0, 11]$. We then see that, for example, v_0 is connected to v_1 (of type 1), v_{11} (of type 11), and $v_7 + e_1$ (of type 7).

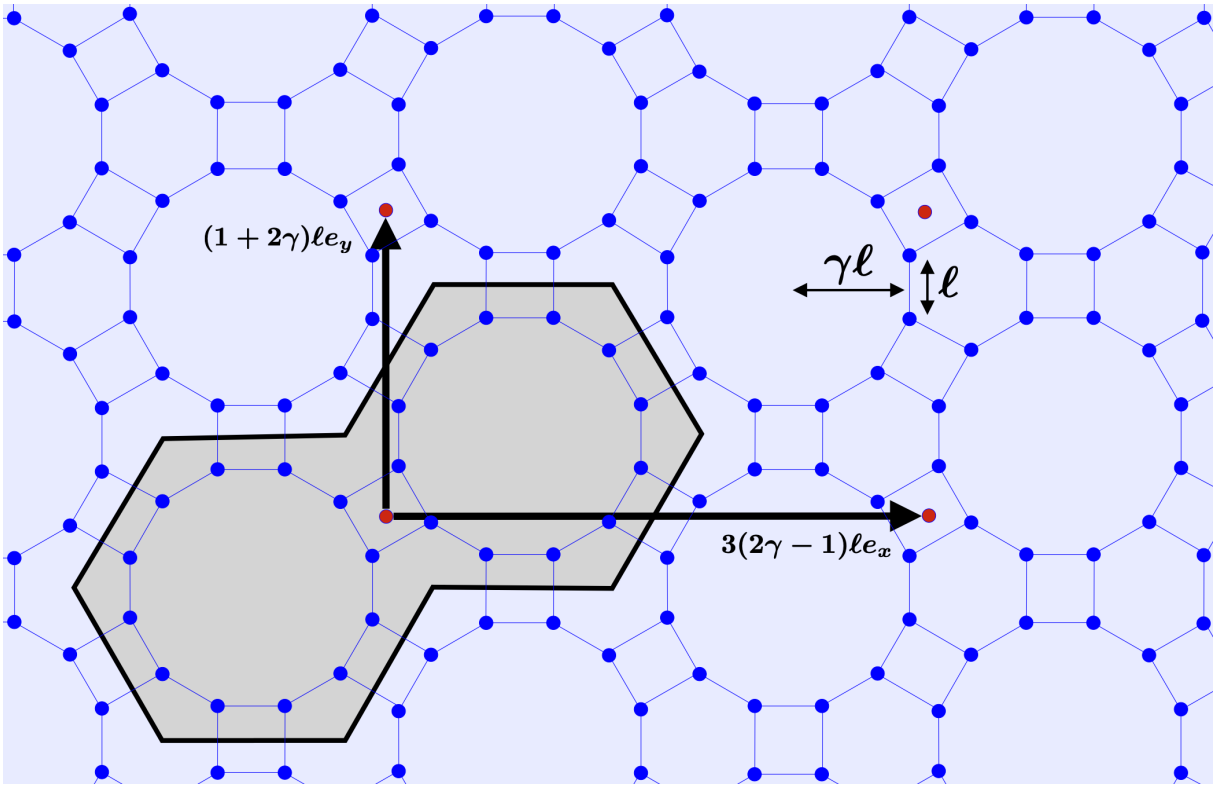

Figure 6.7: Illustration of the tiling procedure for the truncated trihexagonal graph. We tile the rectangular flat torus with orthogonal translations of the Vonoroi cell (in gray). This Voronoi cell is the union of the 24 Voronoi cells corresponding to the two copies of the 12 basis vertices of the dodecagon. The global edge length is ℓ, and the in-circle radius of the dodecagon is $\gamma\ell = (1+\sqrt{3}/2)\ell$. Therefore, the horizontal translation is $3(2\gamma-1)\ell e_x$ and the vertical translation is $(1+2\gamma)\ell e_y$.

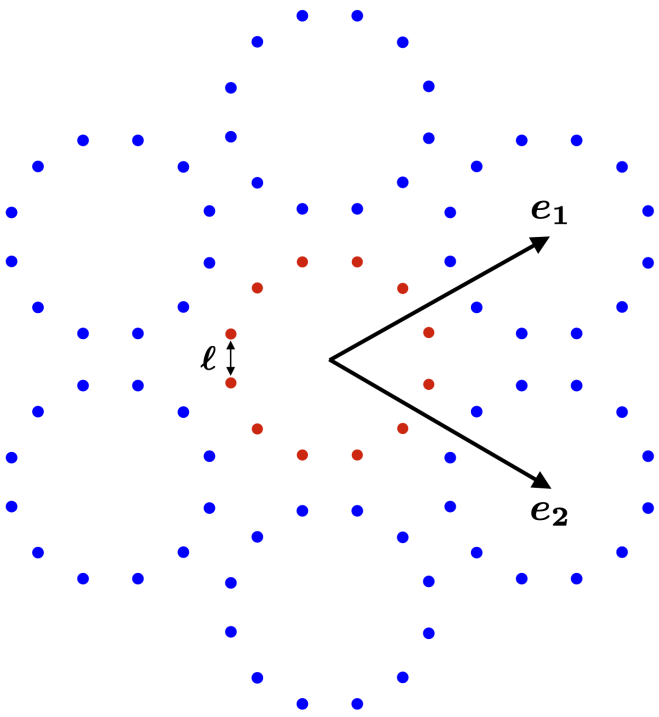

Figure 6.8: Illustration of the generating procedure of the periodic truncated trihexagonal graph. A basis of 12 vertices of the dodecagon (here in red) are translated by lattice vectors e_1, e_2 (c.f. eqs. (6.84)–(6.85)). We display the subset of the lattice generated by translations $ae_1 + be_2$ for $a, b \in \{-1, 0, 1\}$.

$$\sum_{j=0}^{6}(-9)^j\, D_{2j}\cos^{2j}(k\ell) \;=\; 0, \tag{6.86}$$

where

$$\begin{aligned} D_0 &= (2\chi_1+3)^2 && (6.87)\\ D_2 &= 2\,(30\,\chi_1+4\,\chi_2+51) && (6.88)\\ D_4 &= 60\,\chi_1+267 && (6.89)\\ D_6 &= 4\,(3\,\chi_1+70) && (6.90)\\ D_8 &= 111 && (6.91)\\ D_{10} &= 18 && (6.92)\\ D_{12} &= 1, && (6.93) \end{aligned}$$

where

$$\begin{aligned} \chi_1 &= \cos(\kappa_1\ell)+\cos(\kappa_1\ell-\kappa_2\ell)+\cos(\kappa_2\ell) && (6.94)\\ \chi_2 &= \cos(\kappa_1\ell-2\kappa_2\ell)+\cos(\kappa_1\ell+\kappa_2\ell)+\cos(2\kappa_1\ell-\kappa_2\ell) && (6.95) \end{aligned}$$

The dimensions of the $1\times 1/\sqrt{3}$ torus embedding are the same as for the hexagonal lattice. We also require for all plane wave solutions that

$$e^{i(\kappa\cdot(v+(1,0)))} \;=\; e^{i\kappa\cdot v}, \quad e^{i\left(\kappa\cdot(v+(0,1/\sqrt{3}))\right)} \;=\; e^{i\kappa\cdot v}. \tag{6.96}$$

Therefore

$$\kappa_1 \;=\; 3(1+\sqrt{3})(m+n)\pi, \quad \kappa_2 \;=\; 3(1+\sqrt{3})(m-n)\pi, \tag{6.97}$$

for integers m,n where $0\le m\le N-1$ and $0\le n\le \min(m,N-1-m)$. To leading order, eq. (6.86) simplifies to

$$k^2 \;=\; \frac{2+\sqrt{3}}{4}\left[\frac{1}{2}\left((2m\pi)^2+(2n\sqrt{3}\pi)^2\right)\right]+\mathcal{O}\left(\ell^2\right) \tag{6.98}$$

Again, we have a nontrivial factor of $\frac{2+\sqrt{3}}{4}\approx 0.9330...$ multiplying the trace factor of $1/d=1/2$. This is confirmed in the continuum limit.

Continuum limit In the continuum limit, we solve the metric graph corrector equations eqs. (6.57)–(6.58) on a single dodecagon. We obtain

$$\frac{2+\sqrt{3}}{4}\left(\frac{1}{2}\left(\frac{\partial^2}{\partial x^2}+\frac{\partial^2}{\partial y^2}\right)\right)f(x,y) \;=\; -k^2 f(x,y). \tag{6.99}$$

Comparison between finite graph problem and continuum limit In figure figure 6.9 we present convergence of the graph solutions to the continuum limiting solutions eq. (6.99) for increasing graph densities. In figure 6.10 we show a visual comparison of modes.

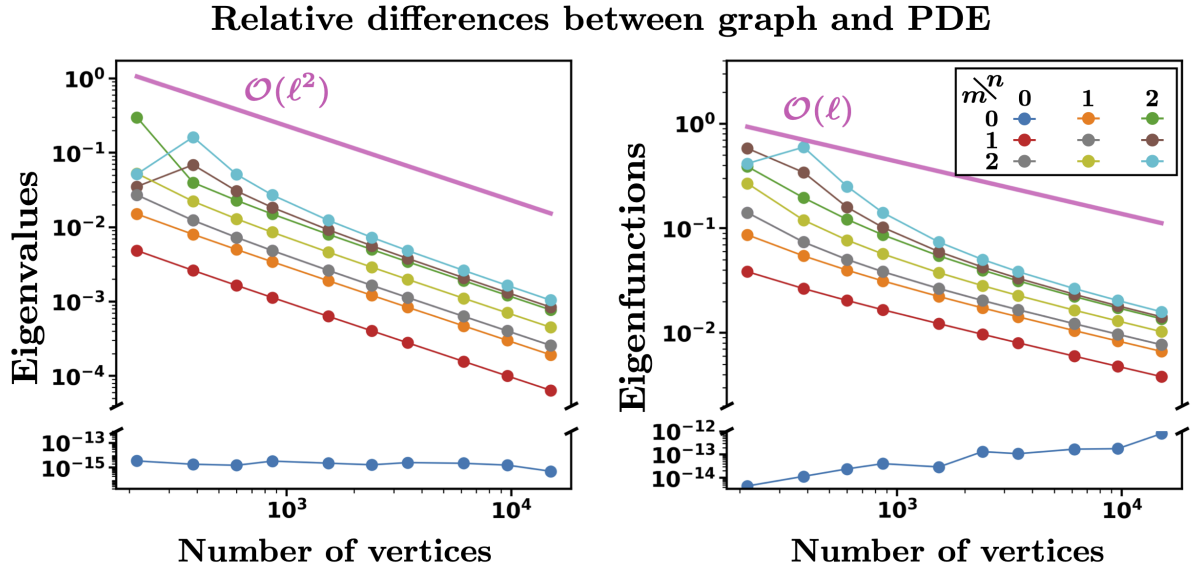

Figure 6.9: Convergence of eigensolutions to the continuum limit for the truncated trihexagonal lattice in the flat rectangular torus.

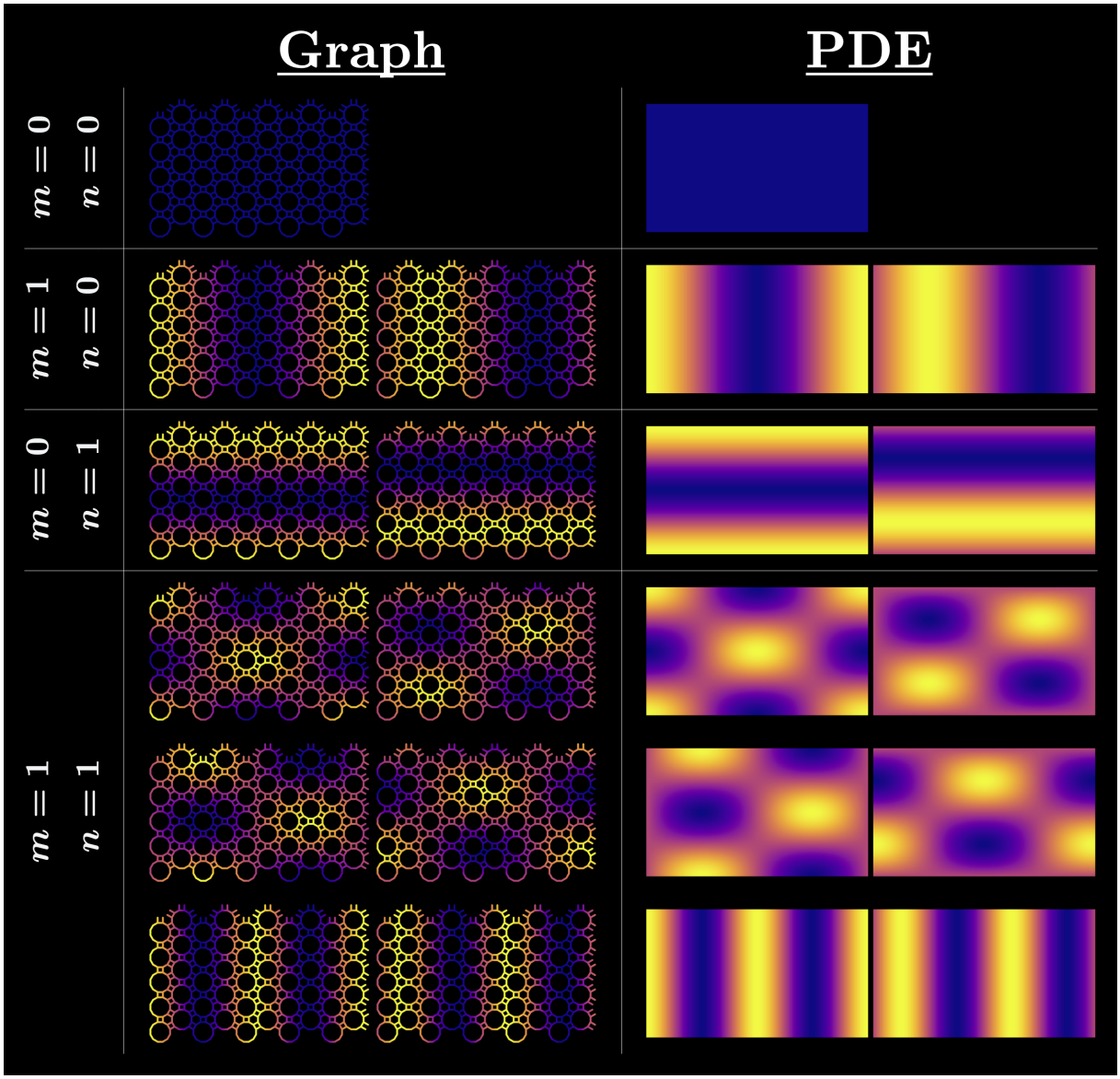

Figure 6.10: Visual comparison of eigenmodes of the NEP and PDE for the periodic truncated trihexagonal graph in the flat rectangular torus.

Chapter 7

Homogenizing local breakdown of the continuum limit: random graphs

The first objective of this PhD was to discover *any* continuum limit of the edgewise Laplace operator. In what turned out to be a rather overly ambitious first attempt, we started with a uniformly random Delaunay triangulation of the unit disc (figure 7.1a)). We noticed that in refining the graph, the eigenvalues did indeed converge. Figure 7.1b) shows the convergence of the first (NEP) eigenvalue, to what we would later find out is close but not equal to $\frac{\alpha_{0,1}}{\sqrt{2}}$: the first eigenvalue of the drum (first zero of the Bessel function of the first kind) rescaled by the square root of the dimension 2 of the disc. This is close to what we would expect from an exactly homogeneous graph such as in section 4.3.1. As we did originally, one might expect that the noise in a uniformly random graph would average out or become negligible in the continuum limit. We now know that the "close to" can be resolved by homogenizing the R tensor to find an empirical coefficient for the dimension scaled Laplacian.

7.1 Uniformly random Delaunay triangulation of the flat torus

Here, we homogenize the R tensor corresponding to a uniformly random Delaunay triangulation of the flat square torus. The objective is to determine an effective Delaunay coefficient c in the limit as the density increases. This can then be used for uniformly random Delaunay triangulations in arbitrary embedding spaces. That is,

$$c\frac{1}{d}\Delta f(x) \;=\; -k^2 f(x), \tag{7.1}$$

where d is the dimension of the embedding space. For the homogeneous and isotropic lattices of the introductory examples, we found a baseline scaling of $\frac{1}{d}$ with $c = 1$. For the truncated square and truncated trihexagonal graphs of the previous chapter, we found $c = \frac{(1+\sqrt{2})^2}{6} \approx 0.971$ and $(2+\sqrt{3})/4 \approx 0.933$ respectively. For the uniformly random Delaunay triangulation, as we will see, we obtain roughly $c = 0.961$. For any other examples which we have tried (uniformly random geometric graphs, quasicrystals,...) we obtain $c \leq 1$, suggesting a possible fundamental upper bound on the ability of a metric graph

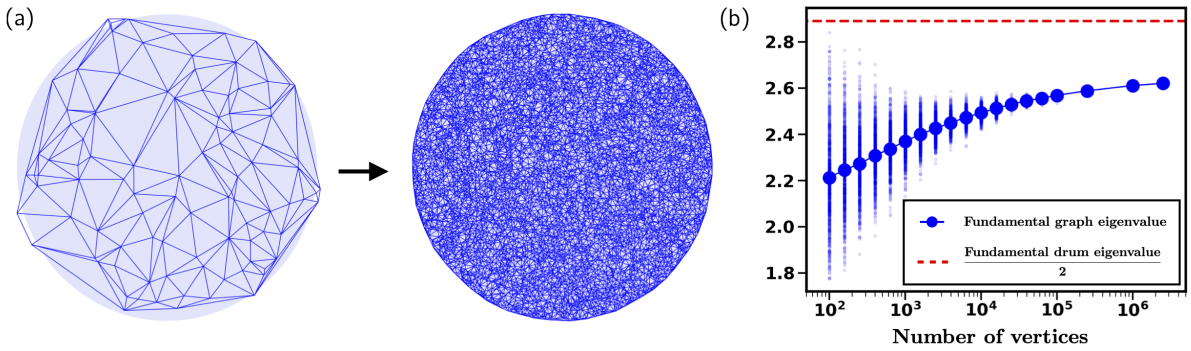

Figure 7.1: (a) Graph refinement for the uniformly random Delaunay triangulation in the unit disc. (b) Ensemble averages of fundamental eigenvalues of increasingly high density random Delaunay triangulations of the disc. We originally expected that this would converge to $\alpha_{0,1}^2/2$: the fundamental manifold (drum) eigenvalue divided by the dimension = 2, as was the case for the periodic graphs in chapter 4. But the Delaunay triangulation is only statistically homogeneous, and we now know that the microstructure produces an effective diffusivity which produces the discrepancy between the continuum limit (dashed red) and the (almost) converged eigenvalue of approximately 2.6. This chapter homogenises the continuum limiting PDE so as to calculate this discrepancy c (figure 7.4). Here, we have made calculations on graphs of up to 2.5e6 vertices, two orders of magnitude higher than any other examples.

to conduct information. The continuum limiting construction triangulates increasingly large samples of the unit square, as illustrated in figure 7.2. For each realization and at each graph size, we determine a homogenized R tensor. The variance in the distribution of the homogenized R tensors decreases as a function of the graph size. We determine the mean value to several orders of magnitude. Overall, we end up with an expected value of the homogenized R tensor for uniformly random Delaunay triangulations at given graph densities.

7.1.1 Construction

To construct a random Delaunay triangulation of the flat torus, we first uniformly sample x, y from $U([0,1)])$ to construct V. We then translate the points by all combinations of left, right, up and down– that is, by $\alpha e_x + \beta e_y$ for $(\alpha, \beta) \in [-1, 0, 1]^2$. We then construct a Delaunay triangulation of the resulting set. We keep only the original vertices V, the edges amongst these vertices, and the "periodic" edges connecting vertices in V with vertices in the translated copies of V, keeping track of the mappings between V and its copies. This is illustrated in figure 7.3.

7.1.2 Coefficient estimation

As defined in detail in [133], we assume that R is a stationary random field–its statistics are translation invariant. We solve the corrector equations eqs. (6.57)–(6.58) for entire triangulations of the torus for increasing densities. We take averages over ensembles at different densities and determine a homogenized tensor $R \approx cI$. In figure 7.4, we show

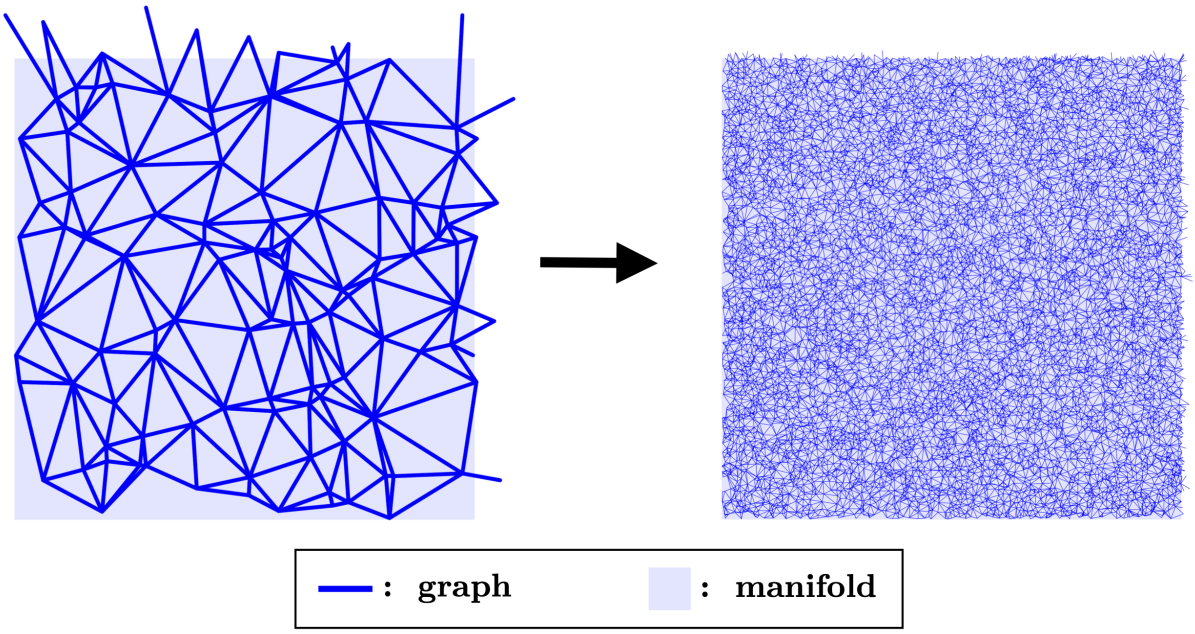

Figure 7.2: Illustration of the continuum limiting procedure for the uniformly random Delaunay triangulation filling in the flat square torus.

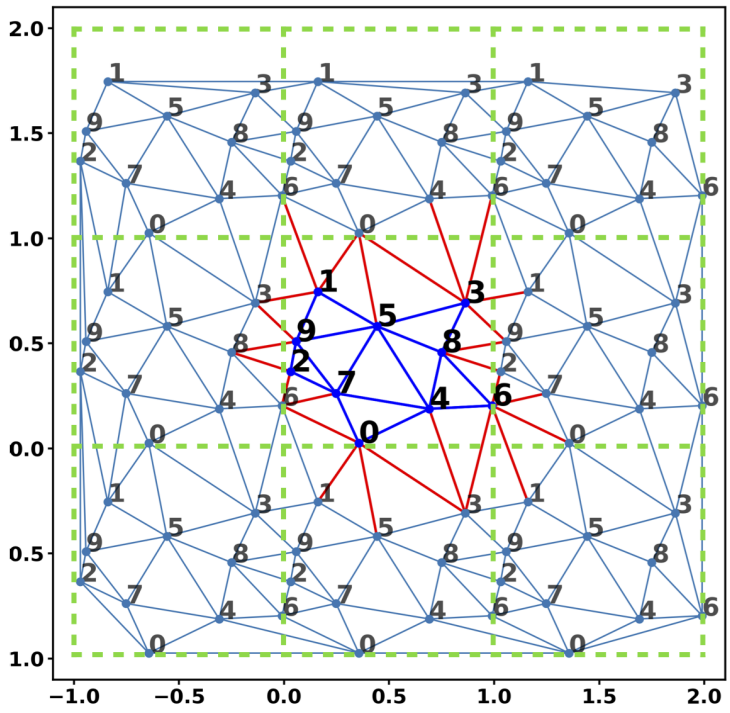

Figure 7.3: Illustration of the construction of a uniformly random Delaunay triangulation of the flat square torus. We randomly sample the unit square to obtain 10 vertices (in blue). We create a finite 3×3 multilattice using the 10 vertices as a basis and translating by unit length lattice vectors e_x, e_y. The vertices are labelled by their membership to a particular sublattice $i \in \{0, 9\}$. We Delaunay triangulate all 90 vertices, and retain only edges connected to the original basis vertices (in blue). The red edges represent periodic connections coming from the periodicity of the torus.

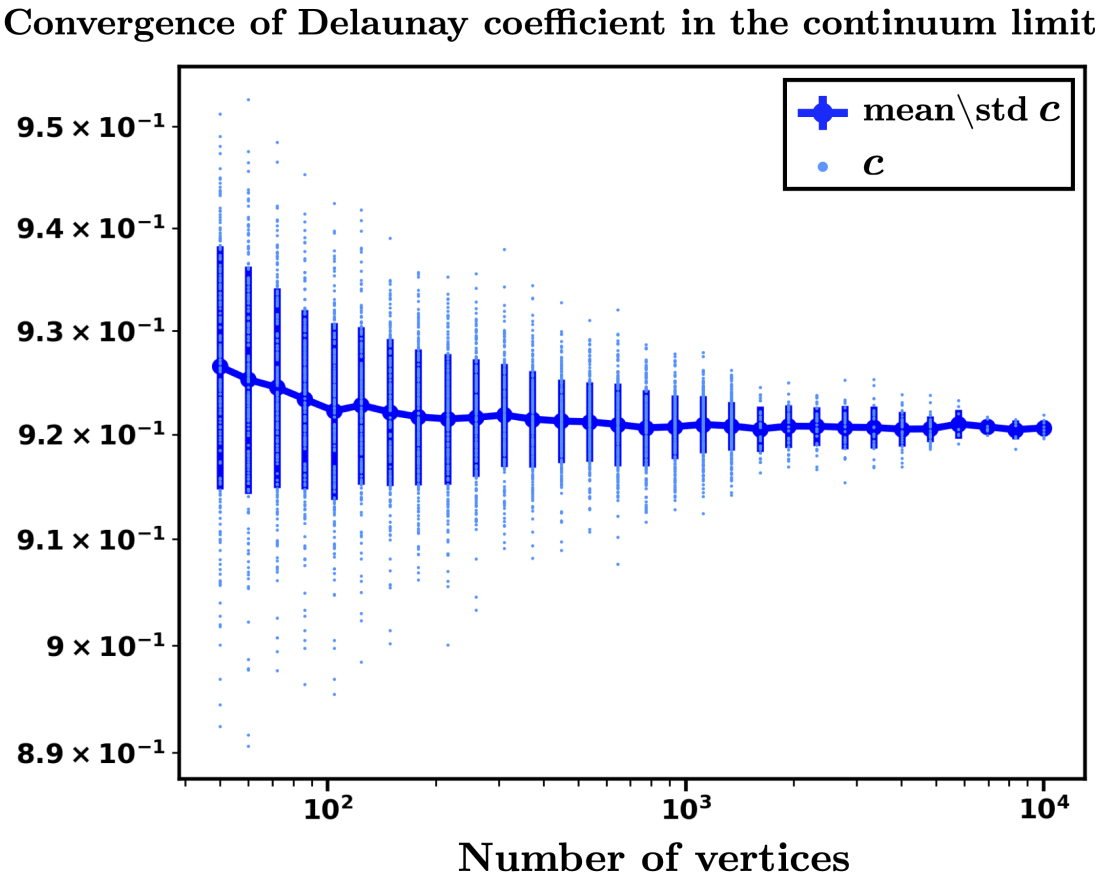

Figure 7.4: Convergence of the homogenized R tensor coefficient c (eq. (7.1)) for the uniformly random Delaunay triangulation. The mean (in dark blue) value over n graph realizations converges to $c \approx 0.921$. We decrease the number of computations n from 200 down to 10 as the standard deviation (vertical bars) decreases.

the convergence to a limiting value $c =\approx 0.921$ for up to 10^4 vertices.

7.1.3 Continuum limit

Here we compare the graph solutions to the continuum limiting solutions of eq. (7.1). We compare solutions for $(m, n) \in \{(0, 1), (1, 0)\}$. That is,

$$k^2 \;=\; \frac{0.921}{2}(2\pi)^2 \tag{7.2}$$

and

$$\{\cos(2\pi x)\,, \sin(2\pi x)\,, \cos(2\pi y)\,, \sin(2\pi y)\}\,. \tag{7.3}$$

We see convergence in figure 7.5. We cannot yet explain the $\mathcal{O}(\ell)$ convergence in place of $\mathcal{O}(\ell)^2$ convergence. In figure 7.6, we present an illustration of a series of graph NEP and continuum PDE modes.

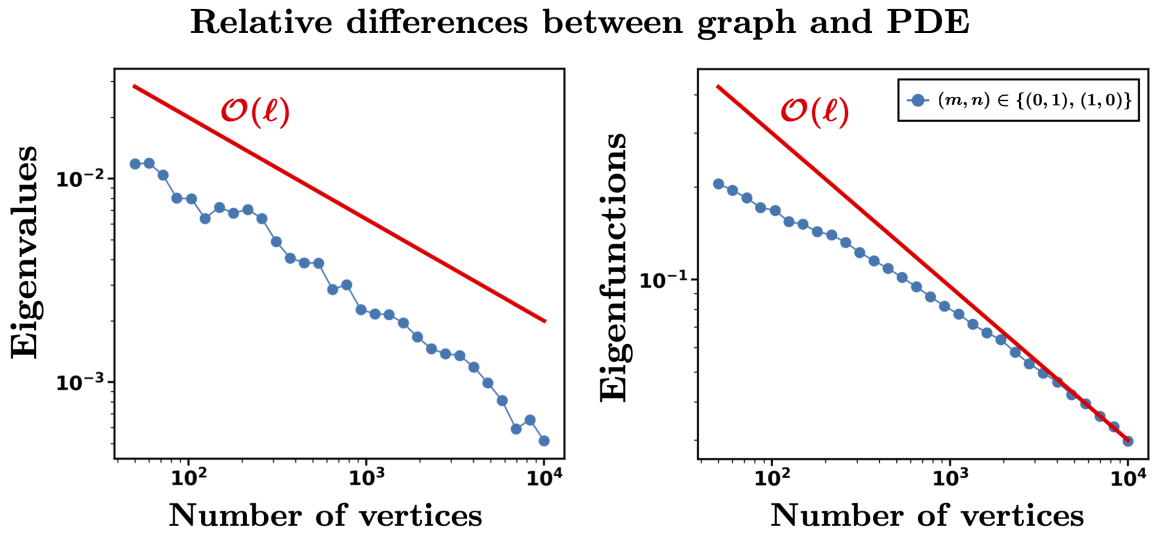

Figure 7.5: Convergence of NEP solutions to continuum limiting PDE solutions for uniformly random Delaunay triangulations of increasing densities in the flat square torus. We compare graph NEP eigenvalues and eigenfunctions to the continuum limiting eigenvalues and eigenfunctions in eq. (7.1) for the empirically determined value $c = 0.921$.

7.2 Constructing random Delaunay triangulations in spheres and balls.

Random graphs are a fascinating topic The canonical example of a random graph takes a set of n vertices and connects every pair with probability p. This is known as the $G(n, p)$ variant of the Erdös-Renyi graph. Random graphs have numerous applications, from modelling internet traffic, pandemic spread, or neural network representations. As usual, we are interested in embeddings within some Riemannian manifold M. We will study the (Delaunay) triangulation of uniformly randomly distributed points within a given M. These constructions have two steps:

1. Constructing the set of vertices V,

2. Constructing the set of edges E.

We will first provide a theory for uniformly randomly sampling the sphere and ball. Then, we will discuss edge generation for Delaunay triangulations (DTs).

7.2.1 Constructing V

Sampling general domains and locally connecting the resulting sets of points are both difficult problems but are commonplace in applications of finite elements, for example. Here, we present three different methods of randomly sampling spheres and balls They are particularly well suited to these geometries but do not necessarily generalise.

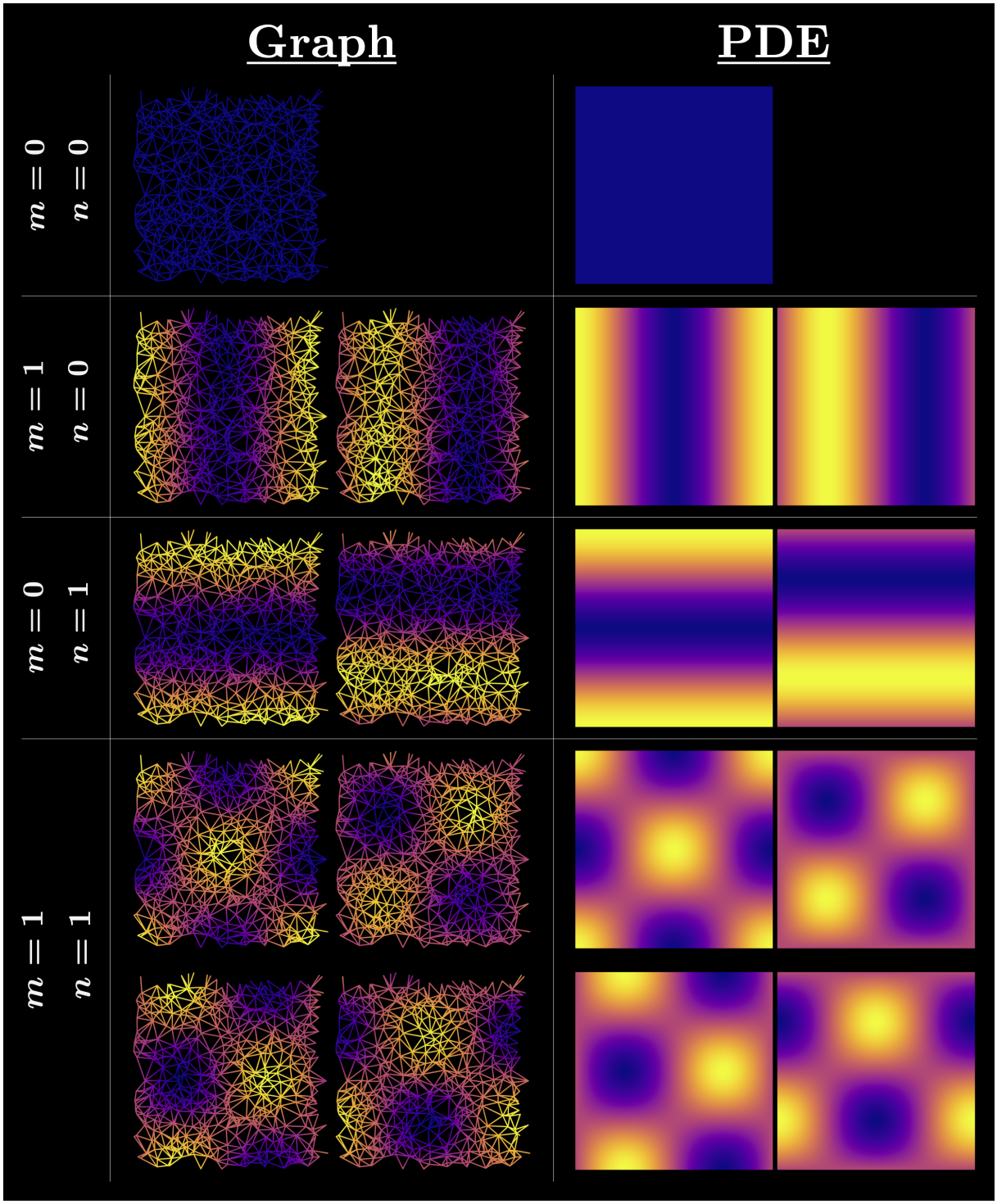

Figure 7.6: Visual comparison of eigenmodes of the NEP and PDE for the uniformly random Delaunay triangulation in the flat square torus. The PDE modes are the Fourier modes $e^{2\pi i(mx+ny)}$.

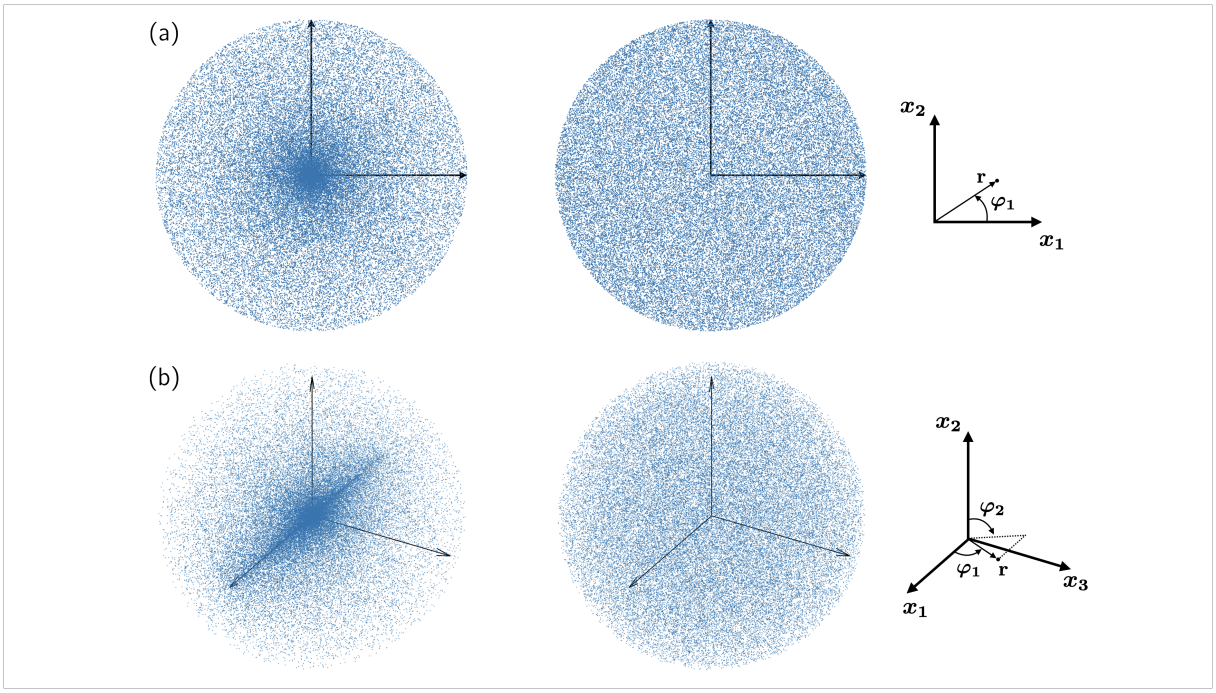

Figure 7.7: Sampling the (a) disc and (b) 3-ball. On the left are the results of uniformly sampling in the radial and angular coordinates. On the right are the results of correctly transforming the coordinates to account for spatial dependence of the spherical Jacobian. The axes on the right illustrate the coordinate choices in eqs. (7.8)–(7.12).

Coordinate reparametrizations

To illustrate the following procedure, we consider uniformly sampling the disc D^2_ρ of radius ρ. We need to find distributions for the radial and angular coordinates $r \in [0, \rho]$ and $\theta \in [0, 2\pi)$ which produce a uniform distribution of points (in the standard basis)

$$(x, y) \;=\; (r\cos(\theta)\,, r\sin(\theta)). \tag{7.4}$$

For the square, we were able to simply take samplings of $x \sim U([0,1])$ and $y \sim U([0,1])$. We cannot do the same for r and θ, as we can see in figure 7.7. The reason is that the Jacobian of the polar transformation eq. (7.4) is non-constant. The area element depends on r

$$\mathrm{d}A \;=\; r\mathrm{d}r\mathrm{d}\theta. \tag{7.5}$$

Therefore, for r and θ sampled uniformly, while a given area element contains the same number of points (in expectation), the sizes of the area elements themselves grow away from the origin, and so the distribution of points overall increases *towards* the origin. We need a transformation $u(r)$ such that $\mathrm{d}A = \mathrm{d}u\mathrm{d}\theta$. We require

$$\mathrm{d}u \;=\; r\mathrm{d}r. \tag{7.6}$$

Integrating, we find that $u : [0, \rho] \to [0, \rho^2/2]$ given by $u(r) = \frac{1}{2}r^2$ works. The (rescaled) inverse transformation $r : [0, \rho^2] \to [0, \rho]$ given by $r(u) = \sqrt{u}$ substituted back into the

coordinates in eq. (7.4) gives

$$(x, y) \;=\; (\sqrt{u}\cos(\theta)\,, \sqrt{u}\sin(\theta)). \tag{7.7}$$

The Jacobian corresponding to this transformation is $|J| = \frac{1}{2}$. Therefore, if $u \sim U([0, \rho^2])$ and $\theta \sim U([0, 2\pi])$, the area elements will be both independent of the coordinates and contain a uniform distribution of points. This is generalizable to the n-ball. The spherical coordinates are $r \in [0, \rho]$, $\varphi_i \in [0, \pi]$ for $1 \leq i < n-1$ and $\varphi_{n-1} \in [0, 2\pi)$ (as illustrateed in figure 7.7). In cartesian coordinates,

$$\begin{aligned}
x_1 &= r\cos(\varphi_1) && (7.8)\\
x_2 &= r\sin(\varphi_1)\cos(\varphi_2) && (7.9)\\
x_3 &= r\sin(\varphi_1)\sin(\varphi_2)\cos(\varphi_3) && (7.10)\\
&\dots \\
x_{n-1} &= r\sin(\varphi_1)\dots\sin(\varphi_{n-2})\cos(\varphi_{n-1}) && (7.11)\\
x_n &= r\sin(\varphi_1)\dots\sin(\varphi_{n-2})\sin(\varphi_{n-1})\,. && (7.12)
\end{aligned}$$

The volume element for the n-sphere is

$$\mathrm{d}V \;=\; r^{n-1}\sin^{n-2}(\varphi_1)\sin^{n-3}(\varphi_2)\dots\sin(\varphi_{n-2})\,\mathrm{d}r\mathrm{d}\varphi_1\mathrm{d}\varphi_2\dots\mathrm{d}\varphi_{n-1}. \tag{7.13}$$

As before, we want to find coordinates transformation $u(r), \theta_1(\varphi_1), \dots, \theta_{n-1}(\varphi_{n-1})$ such that

$$\begin{aligned}
\mathrm{d}u &= r^{n-1}\mathrm{d}r && (7.14)\\
\mathrm{d}\theta_1 &= \sin^{n-2}(\varphi_1)\mathrm{d}\varphi_1 && (7.15)\\
\mathrm{d}\theta_2 &= \sin^{n-3}(\varphi_2)\mathrm{d}\varphi_2 && (7.16)\\
&\dots \\
\mathrm{d}\theta_{n-2} &= \sin(\varphi_{n-2})\mathrm{d}\varphi_{n-2} && (7.17)\\
\mathrm{d}\theta_{n-1} &= \mathrm{d}\varphi_{n-1}. && (7.18)
\end{aligned}$$

For $n = 3$, we have

$$\begin{aligned}
u(r) &= \frac{r^3}{3} && (7.19)\\
\theta_1 &= -\cos(\varphi_1) && (7.20)
\end{aligned}$$

and we can take:

$$\begin{aligned}
r &= (3u)^{1/3} && (7.21)\\
\sqrt{1-\theta_1^2} &= \sin(\varphi_1) && (7.22)
\end{aligned}$$

where we can safely leave the square root because $\varphi_1 \in [0, \pi]$. Now we have

$$x_1 = u^{1/3}\theta_1 \tag{7.23}$$

$$x_2 = u^{1/3}\sqrt{1-\theta_1^2}\sin(\theta_2) \tag{7.24}$$

$$x_3 = u^{1/3}\sqrt{1-\theta_1^2}\cos(\theta_2)\,, \tag{7.25}$$

where $u \in [0, \rho^3]$, $\theta_1 \in [-1, 1]$, $\theta_2 \in [0, 2\pi)$. For arbitrary n, consider

$$I_m(x) = \int \sin^m(x)\mathrm{d}x. \tag{7.26}$$

Integrating by parts, we have

$$I_m(x) = -\frac{\cos(x)\sin^{m-1}(x)}{m} + \frac{m-1}{m}I_{m-2}(x). \tag{7.27}$$

It seems unlikely that a trick similar to that used in eq. (7.22) exists in general, especially given that we only have a recurrence relation for the integration step. While one could integrate and then numerically invert against uniformly randomly sampled ε_i to determine the θ_i, there are simpler methods for arbitrary n.

Rejection sampling

One way to uniformly randomly sample the disc is to uniformly randomly sample the unit square, rejecting samples not contained within the disc. This works well in 2 and 3 dimensions, though the task becomes unfeasible for much higher dimensions. The enclosing (n)-cube C^n of the n-ball B^n has side length 2. Its volume is then simply $\mathrm{vol}\,(C^{n+1}) = 2^n$. However, the volume of the sphere is

$$\mathrm{vol}(B^n) = \frac{\Pi^{n/2}}{\Gamma\left(\frac{n}{2}+1\right)}\rho^n, \tag{7.28}$$

where we take the radius $\rho = 1$. Not only does the volume of the cube increase with dimension, but the volume of the sphere also vanishes combinatorially. For $n = 10$, the sphere represents a quarter of a per cent of the hypercube. In 100 dimensions, the fraction reduces to 10^{-70}. What is amazing is that, as Brian Hayes notes in [134], we are "not talking about a pea rattling around loose inside a refrigerator carton." The unit sphere is the largest possible to fit inside the cube. To make sense of the discrepancy, while the sphere touches the centres of the 100-cube's 200 faces, it fills no space towards its 2^{100} vertices!

Isotropic Gaussian random variables

For arbitrary dimensions in the above, transforming the radial component was simple, but it became increasingly difficult for subsequent angular components. It turns out that there is a simple trick for producing an isotropic distribution of points in $\mathbb{R}^n$. We can combine this with an n-dimensional version of the transformed radial component in eq. (7.23). To

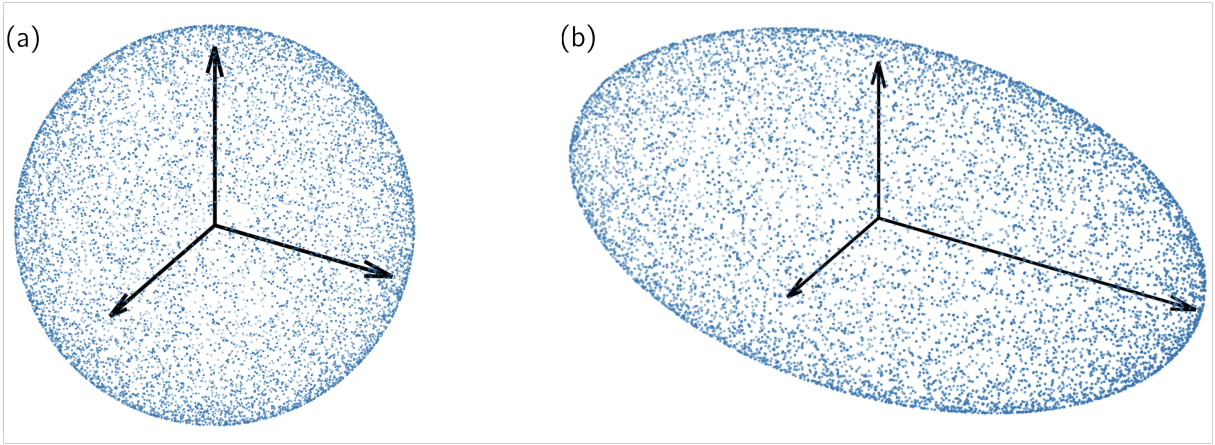

Figure 7.8: Uniformly randomly sampled surfaces. (a) S^2 is uniformly sampled with 3-dimensional standard Gaussian vectors that are normalised. (b) An ellipsoid (spheroid in this case) is sampled similarly, with the entries of the vectors allowed to have distinct variances σ_i. The principal axes of the ellipsoid are the Euclidean axes scaled by the σ_i. In this case, $(\sigma_1, \sigma_2, \sigma_3) = (1, 2, 1)$.

uniformly sample the n-sphere S^n, we exploit the following fact:

Proposition 7.2.1. *Let $x \in \mathbb{R}^{n+1}$ be a vector of $n+1$ independent Gaussian variables x_i with mean 0 and standard deviation σ_i. Then x is isotropic with respect to the ellipsoid n-dimensional $\mathcal{E}$ with principal axes $\sigma_i e_1$: its direction as a position vector in $\mathbb{R}^{n+1}$ is uniformly distributed on $\mathcal{E}$.*

Proof. The components of x are independent. Therefore, their joint probability density function is

$$f(x) \;=\; \frac{1}{\sqrt{2\pi \prod_{i=0}^{n} \sigma_i^2}} e^{-\frac{1}{2}\sum_{i=0}^{n} \frac{x_i^2}{\sigma_i^2}}. \tag{7.29}$$

In ellipsoidal coordinates, equivalent to spherical with r rescaled to $\sigma_i r$, we have

$$\sum_{i=0}^{n} \frac{x_i^2}{\sigma_i^2} \;=\; r^2. \tag{7.30}$$

Therefore, the distribution of points only depends on the ellipsoidal scaling away from the origin. □

Normalizing x places it on the n-sphere, and we then have a uniformly random sampling. This generalises to ellipsoids: if the x_i all still have mean 0 but varying standard deviations σ_i, then x is isotropic with respect to the ellipsoid with principal axes given by $\sigma_i e_i$. Examples of these two are in figure 7.8. For the n-ball, we use the angles for the $(n-1)$-sphere, and then we can uniformly randomly sample by transforming the radial component as in eq. (7.14). So

$$du \;=\; r^{n-1} dr \quad \Rightarrow \quad r \;=\; u^{\frac{1}{n}}, \quad u \in [0, \rho^n], \tag{7.31}$$

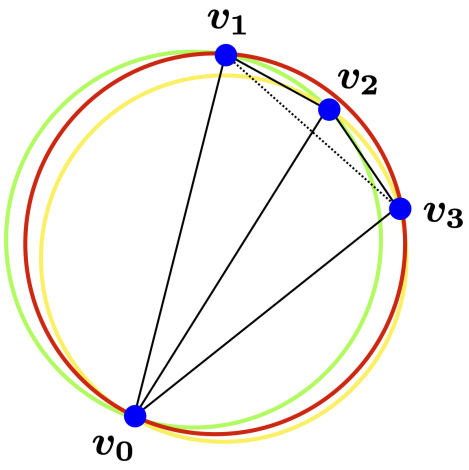

Figure 7.9: A Delaunay triangulation (in solid black) of 4 vertices in the plane. Any three vertices are connected whenever their corresponding circumcircle–the unique circle passing through each vertex–encloses no other vertex. The green and yellow circumcircles, corresponding to (v_0, v_1, v_2) and (v_0, v_2, v_3) respectively, satisfy this criterion. Therefore, each triple is connected. The red circumcircle corresponding to (v_0, v_1, v_3) does not satisfy this criterion because it encloses v_2. Therefore, v_1 and v_3 are not connected, as the dotted line indicates.

where again, for the unit ball, $\rho = 1$. The method involves generating a standard Gaussian vector x, normalizing it, and then scaling it by $u^{1/n}$ where $u \sim U([0, \rho^3 = 1^3])$.

7.2.2 Constructing E

Delaunay triangulations

A Delaunay triangulation of a set of points in the plane, although non-trivial to implement, applies a simple principle: any three points form a triangle if no other point lies within their circumcircle (the circle passing through each of the three points). Figure 7.9 illustrates a simple application of the Delaunay triangulation of four points. The same applies in arbitrary dimensions, where $d + 1$ vertices v are pairwise connected in $\mathbb{R}^d$ so long as no other vertex w is a distance $\delta < R$ away from the centre of their corresponding d-dimensional circumsphere of radius R.

7.3 Random Delaunay triangulation of the disc

In this section, we first construct a uniformly random Delaunay triangulation G of the unit disc (2−ball) B^2 in $\mathbb{R}^2$. We then compare the edgewise Laplace operator on G to its continuum limit on B^2 as a function of the density of vertices.

Setup We construct a uniformly random graph G which fills the unit disc $B^2 = \{x, y \in \mathbb{R} \mid x^2 + y^2 \leq 1\} \subset \mathbb{R}^2$. The obvious strategy would be to sample B^2 uniformly randomly

as in section 7.2.1, and then to apply a Delaunay triangulation from this point set. That is, to construct each vertex $x = r\cos(\theta), y = r\sin(\theta)$ with

$$r \sim \sqrt{U([0,1])} \tag{7.32}$$
$$\theta \sim U([0,2\pi)) \tag{7.33}$$

and then apply Scipy's Delaunay triangulation function. While this is mostly a correct approach, a significant problem arises in resolving the boundary. We want to assume a statistically uniform graph structure throughout the graph, including in the boundary region. The following two points address difficulties relating to constructing and triangulating the boundary so that the edge tensor and vertex density are statistically homogeneous in the boundary region. First, points have a probability 0 of lying on the boundary. Second, unnatural *long* edges occur between boundary vertices when the circumcentres are allowed to be arbitrarily far away. We discuss these two problems as follows.

1. The first problem relates to sampling the boundary itself. We could simply uniformly sample $\theta \sim U([0,2\pi))$, setting $r = 1$. However, there are two problems with this approach. First, we could (over)undersample angle ranges, which we don't ever want to do. We could instead nonrandomly select angles. However, this might introduce unwanted structure (symmetries) to our problem, which in turn leads to the second issue, which is how many boundary vertices to choose. This number should represent some physically representative proportion of the total vertices. However, the boundary (a circle) represents none of the area of the disc. We could select some narrow annulus enclosing the boundary. A consideration here is to ensure that the annulus is correctly extended away from $r = 1$. If we consider an annulus of width 2ε centered at $r = 1$, then the mean radial component of the boundary vertices will be on average > 1. Instead, we want the areas of the (sub)annuli on either side of $r = 1$ to be equal. Setting ε_- to be the width of the inner annulus, then the width of the outer annulus ε_+ must satisfy

$$\pi\left(r^2 - (r-\varepsilon_-)^2\right) = \pi\left((r+\varepsilon_+)^2 - r^2\right) \quad \Rightarrow \quad \varepsilon_+ = -r + \sqrt{r^2 + 2r\varepsilon_- - \varepsilon_-^2}. \tag{7.34}$$

   However, there is no obvious principle for choosing $\varepsilon = \varepsilon_- + \varepsilon_+$ as a function of $|V|$. Furthermore, we still encounter the next issue.

2. The second problem relates to connecting boundary vertices. A Delaunay triangulation will produce spurious (long) edges between boundary vertices, as is measured in figure 7.11. Figure 7.10 illustrates the mechanism behind this error. When three boundary vertices are distributed like v_0, v_1, v_2 in figure 7.10b–being close to collinear and having the middle vertex (v_1) is closest to the origin–then their corresponding circumcircle will be extended arbitrarily away from the disc. The edge $v_0 \leftrightarrow v_1$ will be artificially long. While we could simply reject those triangles whose circumcircles are centred some extended distance away, this would leave us with having to decide on such a cutoff. Furthermore, we are still left with the problem of arbitrarily selecting the boundary annulus itself. The way we contend with these issues is to introduce dummy vertices to triangulate over. We sample over a sufficiently extended

square (a larger disc would also suffice). We triangulate this point set and designate a boundary vertex as any vertex with at least one connection to a vertex with $r < 1$ and at least one connection to a vertex with $r \geq 1$. This naturally satisfies the annulus criterion, that is, there is a physically sensible number of boundary vertices on either side of $r = 1$, and connections between vertices are now restricted by the Delaunay circumcircle criterion encountering dummy vertices extending beyond the disc: red vertices are enclosed by (dotted pink) circumcircles. While this boundary vertex criterion still seems rather arbitrary, it, in some sense, produces what one would expect from perturbing vertex locations of a highly uniform configuration (e.g. a hexagonal lattice). The final product is figure 7.10c.

Continuum limit In this case, the continuum limit is

$$\frac{c}{d}\Delta f(x) \;=\; -k^2 f(x) \tag{7.35}$$

on the open disc where $f(S^1) = 0$. As measured in the previous section, the empirical local coefficicent of the R tensor for a uniformly random Delaunay triangulation is $c/d \approx 0.921/2$. Eq. (7.35) has vibrating drum solutions

$$f_{m,j}(r,\theta) \;=\; J_m(\alpha_{m,j} r)e^{im\theta}, \tag{7.36}$$

where $J_m(\alpha_{m,j}) = 0$, and

$$k^2 \;=\; \frac{c}{d}\alpha_{m,j}^2 \tag{7.37}$$

where $J_m(\alpha_{m,j}) = 0$. We show convergence for the fundamental mode with $(m, j) = (0, 1)$ in figure 7.12. We take averages of between 16-128 samples per graph size (starting with 128 at $|V| = 100$ and 16 at $|V| = 10^5$). We cannot yet explain the $\mathcal{O}(\ell)$ as opposed to $\mathcal{O}(\ell)^2$ convergence. In figure 7.13 we show a visual comparison of several graph and PDE modes.

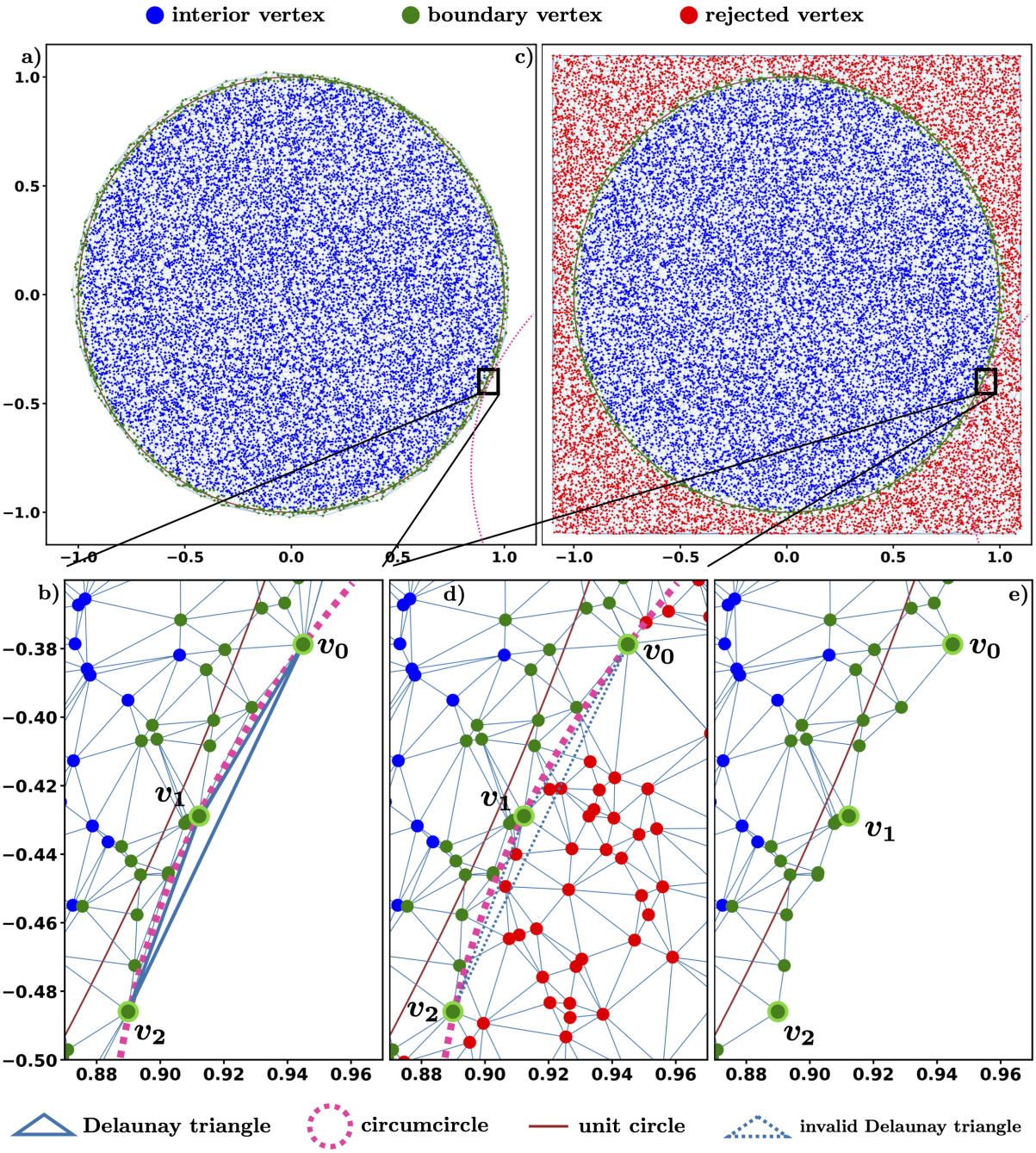

Figure 7.10: Resolving the boundary of a uniformly random Delaunay triangulation of the unit disc. a) A triangulation constructed from reparametrised uniform samplings of r, θ. This suffers from two issues: 1) choosing a number of boundary vertices as a function of the total number of vertices, and 2) the Delaunay algorithm creating spurious long edges. This latter problem is illustrated in b), where we see that the circumcircle corresponding to v_0, v_1, v_2 is allowed to extend arbitrarily far away, ending up with the Delaunay triangle between each vertex and outlier edge $v_0 \leftrightarrow v_2$. In c), we solve this problem by sampling from a larger square instead. Boundary vertices are those with at least one neighbour on each side (inner and outer) of $r = 1$. Retaining the triangulation corresponding only to interior and boundary vertices, we obtain e). As we see in d), the rejected vertices don't allow for the circumcircle from a-b). We could instead retain the method from a), and reject circumcircles whose centres lie a certain distance from the disc, but this leaves one with having to decide both an appropriate such distance, and still the problem of determining the number and placement of boundary vertices.

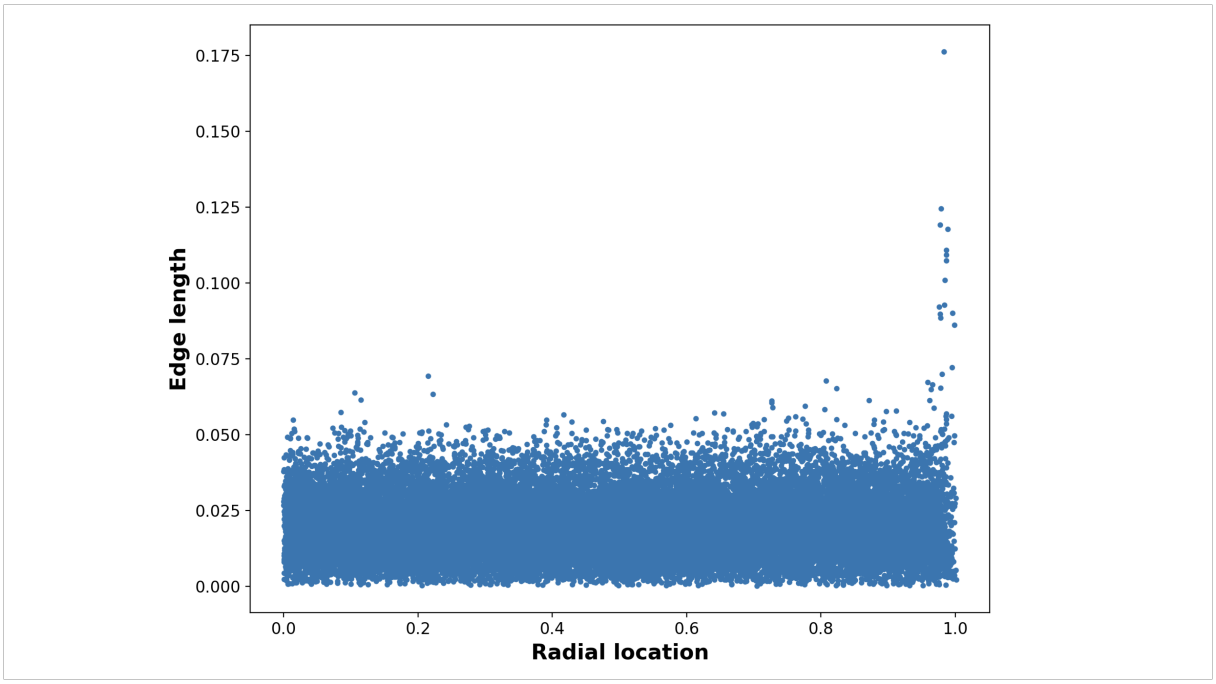

Figure 7.11: Distribution of edge lengths by the radial location of the edge midpoints in a uniformly random Delaunay triangulation of the unit disc. Using the sampling method from 7.2.1, we see invalid long edges in the boundary region. As is explained in figure 7.10, this is because circumcircles are allowed to be centred arbitrarily far beyond the boundary of the disc.

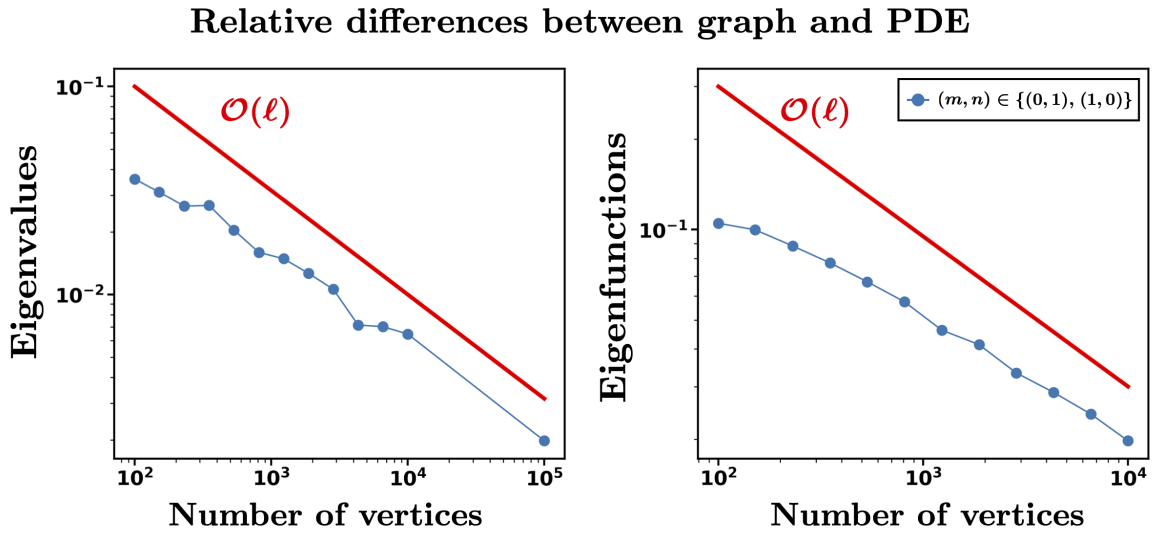

Figure 7.12: Convergence of graph solutions to continuum limiting PDE solutions for uniformly random Delaunay triangulations of increasing densities in the disc. We compare graph NEP eigenvalues and eigenfunctions to the continuum limiting eigenvalues and eigenfunctions in eq. (7.35) for the empirically determined value $c = 0.921$.

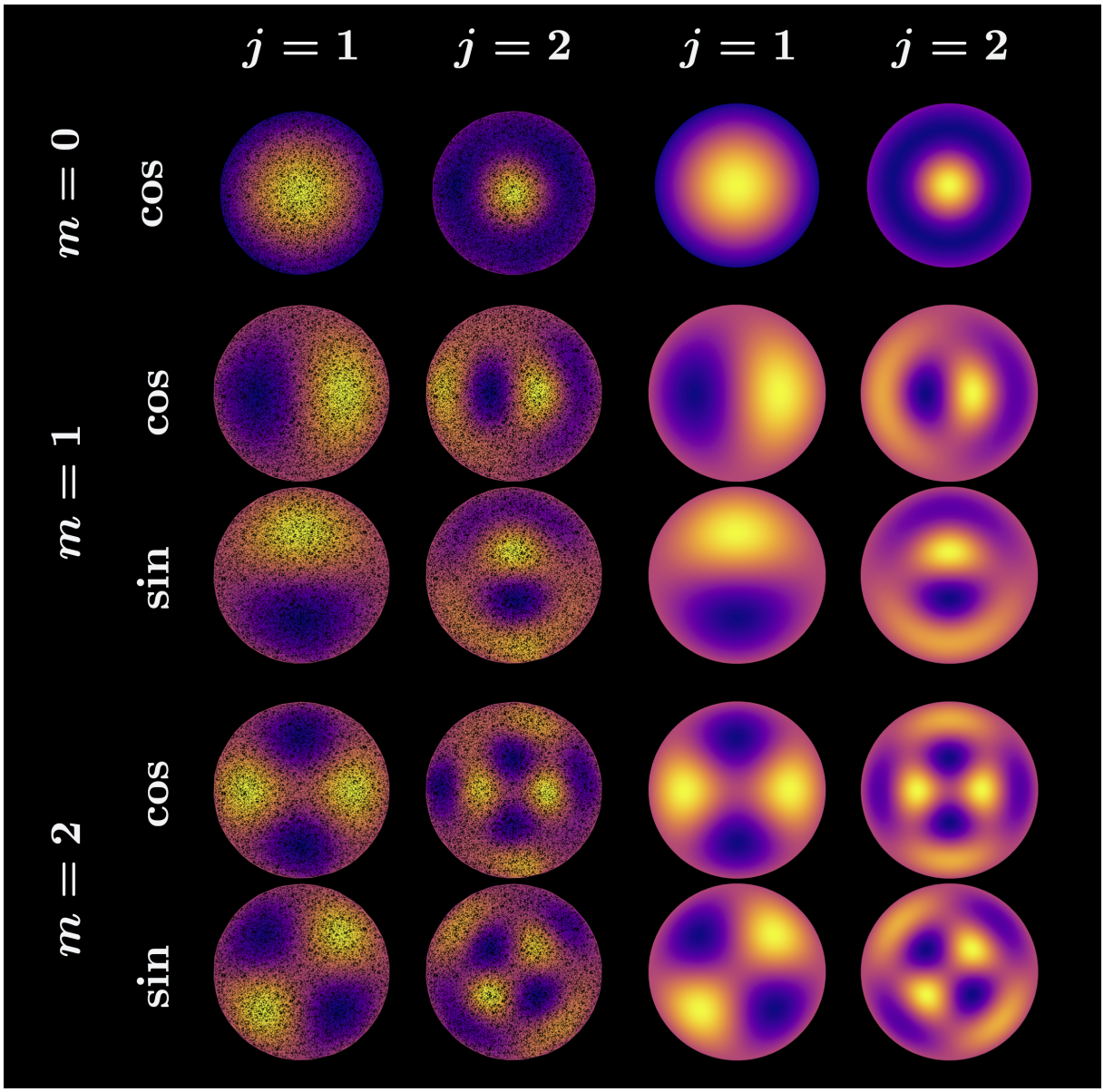

Figure 7.13: Visual comparison of graph modes and drum modes from eq. (7.36).

Chapter 8

Conclusions

Metric graphs are a bridge between fully discrete and fully continuum models of a wide range of complex phenomena. This thesis has introduced a new picture of large-scale degrees of freedom of dense metric graphs as fully continuum PDEs in higher dimensions. The continuum limit is useful for several reasons.

In some cases, a well-understood PDE gives an approximate but simpler analytical way to describe certain modes in a graph that would otherwise require pure numerical intervention. The spiderweb graph in section 5.1 is a good example of this scenario, where we find continuum solutions in terms of Bessel functions in some cases, but there does not seem to be any analytical progress possible in the graph regime.

However, more than an approximation scheme, the continuum limit gives new explanatory power to otherwise incoherent numerical computation. The random graphs of chapter 7 are perhaps the best example of this principle. In the fully random case, it is (to the author) rather startling that stable and reproducible behaviour emerges out of such a generally chaotic spectrum. Hopefully, in the future, these notions lead to exciting applications in modelling more realistic graphs that turn up in natural settings.

Finally, the continuum explanatory power is even more interesting when combined with analytically solvable graph models, which we can already glean a fair bit about. The various regular lattices in chapter 2.3 are good examples of this aspect. An example of new simple insight learned comes from seeing how, in the homogeneous and isotropic case, we obtain the standard equation for the Laplace operator, but a factor of $1/d$, the inverse dimension of the embedding space. We also found the need for a new kind of hybrid discrete-continuous local homogenization procedure even in many examples of regular periodical two-dimensional lattices.

We envision a number of future directions that would follow naturally from the work done here. Below, we give a list of potential follow up mathematical studies and areas to apply contimuum modes of metric graphs.

More complex graph structure Several interesting areas involve studying locally varying graph structue either through geometry or physical properties. Examples include:

- *Scattering in metamaterials*: Recent metric graph models [22] of scattering in metamaterials show negative refraction between periodic rectangular graphs (as in figure 4.14) with varying edge length ratios. Some of these examples use graphs that we find well-beahved limits using homogenization.

- *global graph-varying conductivity and capacity*: Much more work can be done investigating the dependence on local edge conductivity, K, and capacity, C. Particular distributions of K and C across a graph can, in principle, bring the contimuum limit into correspondence with metric Riemannian manifolds.

- *Local edge-varying conductivity and capacity*: We would like to study cases where local edge conductivity, $K(x)$, and capacity, $C(x)$, both have strong dependnce along edges. There are several ways to treat this, including breaking edges into approximately piecewise constant edges and applying our current methods. Another approach would use more general Green's functions along edges. Natural applications with complicated conductivity and capacity profiles will likely happen in biological systems.

- *Different random-graph ensembles*: We currently only studied random Delaunay triangulations. Many more options exist that might give better models of real-world graphs; e.g. random geometric graphs (vertices connected to all within an ε-ball), random trees with interconnected branches (e.g. capillary systems), percolated periodic graphs, Waxman models (probability of connection is a decaying function of distance).

- *n-level homogenization*: We would like to better understand the potential for recursive homogenization, with the lowest level comprising the discrete version presented here.

- *Non-compact embedding spaces*: We would like to investigate metric graphs of fixed density within non-compact domains such as Euclidean space; e.g. the spiderweb extending infinitely throughout the plane.

Nonlinear dynamics and non-Laplacian models Several future studies could look at more complex model equations or systems of equations.

- *KdV*: Both the linearised and nonlinear KdV equations would be extremely interesting on metric graphs. In particular, edges have specific directionality; *i.e.*, nonlinear waves move to the right and linear waves move leftward. It's far from clear how solitons would behave at vertices with multiple edges with multiple directionalities.

- *Sine-Gordon equation*: A highly nonlinear system with the same Laplace-like linear term studied here. Interestingly, the Sine-Gordon equation is well-knonw to have interesting topological dynamics (e.g., kinks and anti-kinks). It's quite interesting to consider how this might play out on dense systems.

- *Generalising to higher dimensions*: Bubbles and foams. Oxygenation via capillary systems (edges) into organs (faces).

Discretizations In 2.6, we showed the differences between the finite element cotangent Laplacian and the edgewise Laplace operator. We would like to determine whether correspondences can be made between the graph problem and the finite element discretization of the continuum limiting PDE. This would provide further insight into the differences between our continuum limit and the Laplace-Beltrami operator. This would also provide

a clearer framework for solving the continuum limit for arbitrary graphs whose solutions can only be approximated numerically

Convergence proofs The formal derivation of the continuum limit assumes weak convergence of vertex eigenfunctions to the manifold eigenfunctions. It remains for this to be proven rigourously under general conditions, both in the case that the R tensor has a well-defined continuum-limiting representation and in the random or high-oscillatory cases when homogenization is required.

Bibliography

[1] Gregory Berkolaiko and Peter Kuchment. *Introduction to quantum graphs*, volume 186 of *Mathematical Surveys and Monographs*. American Mathematical Soc., 2013.

[2] Mark Kac. Can one hear the shape of a drum? *The American Mathematical Monthly*, 73(4P2):1–23, April 1966. ISSN 1930-0972. doi: 10.1080/00029890.1966.11970915. URL http://dx.doi.org/10.1080/00029890.1966.11970915.

[3] Carolyn Gordon, David L. Webb, and Scott Wolpert. One cannot hear the shape of a drum. *Bulletin of the American Mathematical Society*, 27(1):134–138, 1992. ISSN 1088-9485. doi: 10.1090/s0273-0979-1992-00289-6. URL http://dx.doi.org/10.1090/S0273-0979-1992-00289-6.

[4] Felix Mehmeti. *Partial Differential Equations on multistructures*. CRC Press, 2001.

[5] Boris Gutkin and Uzy Smilansky. Can one hear the shape of a graph? *Journal of Physics A: Mathematical and General*, 34(31):6061–6068, July 2001. ISSN 1361-6447. doi: 10.1088/0305-4470/34/31/301. URL http://dx.doi.org/10.1088/0305-4470/34/31/301.

[6] Pavel Kurasov and Marlena Nowaczyk. Inverse spectral problem for quantum graphs. *Journal of Physics A: Mathematical and General*, 38(22):4901–4915, May 2005. ISSN 1361-6447. doi: 10.1088/0305-4470/38/22/014. URL http://dx.doi.org/10.1088/0305-4470/38/22/014.

[7] Linus Pauling. The diamagnetic anisotropy of aromatic molecules. *The Journal of chemical physics*, 4(10):673–677, 1936.

[8] J. I. Rawlinson. An alpha particle model for carbon-12. *Nuclear physics. A*, 975: 122–135, 2018. ISSN 0375-9474.

[9] J. I. Rawlinson. Quantum graph model for rovibrational states of protonated methane. *The Journal of chemical physics*, 151(16):164303–164303, 2019. ISSN 0021-9606.

[10] C. J. Halcrow and J. I. Rawlinson. Electromagnetic transition rates of c 12 and o 16 in rotational-vibrational models. *Physical review. C*, 102(1), 2020. ISSN 2469-9985.

[11] Irën Simkö, Csaba Fäbri, and Attila G. Csäszär. Quantum-chemical and quantum-graph models of the dynamical structure of ch5. *Journal of chemical theory and computation*, 19(1):42–50, 2023. ISSN 1549-9618.

[12] J. I. Rawlinson, C. Fäbri, and A. G. Csäszär. Exactly solvable 1d model explains the low-energy vibrational level structure of protonated methane. *Chemical communications (Cambridge, England)*, 57(39):4827–483, 2021. ISSN 1359-7345.

[13] Csaba Fábri, Martin Quack, and Attila G Császár. On the use of nonrigid-molecular symmetry in nuclear motion computations employing a discrete variable representation: A case study of the bending energy levels of ch 5+. *The Journal of Chemical Physics*, 147(13):134101, 2017.

[14] Christie S Chiu, Annette N Carroll, Nicolas Regnault, and Andrew A Houck. Line-graph-lattice crystal structures of stoichiometric materials. *Physical Review Research*, 4(2):023063, 2022.

[15] Joakim Hagel, Samuel Brem, Christopher Linderälv, Paul Erhart, and Ermin Malic. Exciton landscape in van der waals heterostructures. *Physical Review Research*, 3 (4):043217, 2021.

[16] Yuan Cao, Valla Fatemi, Shiang Fang, Kenji Watanabe, Takashi Taniguchi, Efthimios Kaxiras, and Pablo Jarillo-Herrero. Unconventional superconductivity in magic-angle graphene superlattices. *Nature*, 556(7699):43–50, 2018.

[17] Yuan Cao, Valla Fatemi, Ahmet Demir, Shiang Fang, Spencer L Tomarken, Jason Y Luo, Javier D Sanchez-Yamagishi, Kenji Watanabe, Takashi Taniguchi, Efthimios Kaxiras, et al. Correlated insulator behaviour at half-filling in magic-angle graphene superlattices. *Nature*, 556(7699):80–84, 2018.

[18] Claudio Amovilli, Frederik E Leys, and Norman H March. Electronic energy spectrum of two-dimensional solids and a chain of c atoms from a quantum network model. *Journal of mathematical chemistry*, 36(2):93–112, 2004.

[19] Frederik E Leys, Claudio Amovilli, and Norman H March. Topology, connectivity, and electronic structure of c and b cages and the corresponding nanotubes. *Journal of chemical information and computer sciences*, 44(1):122–135, 2004.

[20] César R de Oliveira and Vinícius L Rocha. Bidimensional honeycomb materials: A graph model through dirac operator. *Reports on Mathematical Physics*, 89(2): 231–252, 2022.

[21] Lee Fisher, Wei Li, and Stephen P Shipman. Reducible fermi surface for multi-layer quantum graphs including stacked graphene. *Communications in Mathematical Physics*, 385(3):1499–1534, 2021.

[22] Tristan Lawrie, Gregor Tanner, and Dimitrios Chronopoulos. A quantum graph approach to metamaterial design. *Scientific Reports*, 12(1):1–14, 2022.

[23] E. Doron, U. Smilansky, and A. Frenkel. Experimental demonstration of chaotic scattering of microwaves. *Physical review letters*, 65(25):3072–3075, 1990. ISSN 0031-9007.

[24] Oleh Hul, Szymon Bauch, Prot Pakoński, Nazar Savytskyy, Karol Życzkowski, and Leszek Sirko. Experimental simulation of quantum graphs by microwave networks. *Physical review. E, Statistical physics, plasmas, fluids, and related interdisciplinary topics*, 69(5):7–056205, 2004. ISSN 1063-651X.

[25] Michał Ławniczak, Jiří Lipovský, and Leszek Sirko. Non-weyl microwave graphs. *Physical review letters*, 122(14):140503–140503, 2019. ISSN 0031-9007.

[26] Vitalii Yunko, Małgorzata Białous, and Leszek Sirko. Edge switch transformation in microwave networks. *Physical review. E*, 102(1):012210–012210, 2020. ISSN 2470-0045.

[27] Junjie Lu, Jiongning Che, Xiaodong Zhang, and Barbara Dietz. Experimental and numerical investigation of parametric spectral properties of quantum graphs with unitary or symplectic symmetry. *Physical review. E*, 102(2):022309–022309, 2020. ISSN 2470-0045.

[28] Douglas N. Arnold, Guy David, David Jerison, Svitlana Mayboroda, and Marcel Filoche. Effective Confining Potential of Quantum States in Disordered Media. *Physical Review Letters*, 116(5):056602, February 2016. ISSN 0031-9007, 1079-7114. doi: 10.1103/PhysRevLett.116.056602. URL https://link.aps.org/doi/10.1103/PhysRevLett.116.056602.

[29] Marcel Filoche, Marco Piccardo, Yuh-Renn Wu, Chi-Kang Li, Claude Weisbuch, and Svitlana Mayboroda. Localization landscape theory of disorder in semiconductors. I. Theory and modeling. *Physical Review B*, 95(14):144204, April 2017. ISSN 2469-9950, 2469-9969. doi: 10.1103/PhysRevB.95.144204. URL http://link.aps.org/doi/10.1103/PhysRevB.95.144204.

[30] Marco Piccardo, Chi-Kang Li, Yuh-Renn Wu, James S. Speck, Bastien Bonef, Robert M. Farrell, Marcel Filoche, Lucio Martinelli, Jacques Peretti, and Claude Weisbuch. Localization landscape theory of disorder in semiconductors. II. Urbach tails of disordered quantum well layers. *Physical Review B*, 95(14):144205, April 2017. ISSN 2469-9950, 2469-9969. doi: 10.1103/PhysRevB.95.144205. URL http://link.aps.org/doi/10.1103/PhysRevB.95.144205.

[31] Chi-Kang Li, Marco Piccardo, Li-Shuo Lu, Svitlana Mayboroda, Lucio Martinelli, Jacques Peretti, James S. Speck, Claude Weisbuch, Marcel Filoche, and Yuh-Renn Wu. Localization landscape theory of disorder in semiconductors. III. Application to carrier transport and recombination in light emitting diodes. *Physical Review B*, 95(14):144206, April 2017. ISSN 2469-9950, 2469-9969. doi: 10.1103/PhysRevB.95.144206. URL http://link.aps.org/doi/10.1103/PhysRevB.95.144206.

[32] F. Gebhard, A. V. Nenashev, K. Meerholz, and S. D. Baranovskii. Quantum states in disordered media. i. low-pass filter approach, 2022.

[33] Evans M. Harrell II and Anna V. Maltsev. Localization and landscape functions on quantum graphs. *Transactions of the American Mathematical Society*, 373(3):1701–1729, November 2019. ISSN 0002-9947, 1088-6850. doi: 10.1090/tran/7908. URL https://www.ams.org/tran/2020-373-03/S0002-9947-2019-07908-4/.

[34] Holger Schanz and Uzy Smilansky. Periodic-orbit theory of anderson localization on graphs. *Physical Review Letters*, 84(7):1427, 2000.

[35] Peter D Hislop and Olaf Post. Anderson localization for radial tree-like random quantum graphs. *Waves in Random and Complex Media*, 19(2):216–261, 2009.

[36] Frédéric Klopp and Konstantin Pankrashkin. Localization on quantum graphs with random edge lengths. *Letters in Mathematical Physics*, 87(1):99–114, 2009.

[37] Mostafa Sabri. Anderson localization for a multi-particle quantum graph. *Reviews in Mathematical Physics*, 26(01):1350020, 2014.

[38] David Damanik, Jake Fillman, and Selim Sukhtaiev. Localization for anderson models on metric and discrete tree graphs. *Mathematische Annalen*, 376(3):1337–1393, 2020.

[39] Michele Gaio, Dhruv Saxena, Jacopo Bertolotti, Dario Pisignano, Andrea Camposeo, and Riccardo Sapienza. A nanophotonic laser on a graph. *Nature Communications*, 10(1), January 2019. doi: 10.1038/s41467-018-08132-7. URL https://doi.org/10.1038/s41467-018-08132-7.

[40] M. Brio, J. G. Caputo, and H. Kravitz. Localized eigenvectors on metric graphs, 2022.

[41] Mohammad Suja, Sunayna Binte Bashar, Bishwajit Debnath, Longxing Su, Wenhao Shi, Roger Lake, and Jianlin Liu. Electrically driven deep ultraviolet MgZnO lasers at room temperature. *Scientific Reports*, 7(1), June 2017. doi: 10.1038/s41598-017-02791-0. URL https://doi.org/10.1038/s41598-017-02791-0.

[42] Bongjin Jeong, Rashida Akter, Jeonghyun Oh, Dong-Gi Lee, Chang-Geun Ahn, Jong-Soon Choi, Md Rahman, et al. Novel electrochemical pmi marker biosensor based on quantum dot dissolution using a double-label strategy. *Scientific Reports*, 12(1):1–8, 2022.

[43] Onur Kulce, Deniz Mengu, Yair Rivenson, and Aydogan Ozcan. All-optical information-processing capacity of diffractive surfaces. *Light: Science & Applications*, 10(1), January 2021. doi: 10.1038/s41377-020-00439-9. URL https://doi.org/10.1038/s41377-020-00439-9.

[44] Danielle S. Bassett and Olaf Sporns. Network neuroscience. *Nature neuroscience*, 20(3):353–364, 2017. ISSN 1097-6256.

[45] Miriam Menzel, Markus Axer, Hans De Raedt, Irene Costantini, Ludovico Silvestri, Francesco S Pavone, Katrin Amunts, and Kristel Michielsen. Toward a high-resolution reconstruction of 3d nerve fiber architectures and crossings in the brain using light scattering measurements and finite-difference time-domain simulations. *Physical Review X*, 10(2):021002, 2020.

[46] Henry Markram. The blue brain project. *Nature reviews. Neuroscience*, 7(2):153–160, 2006. ISSN 1471-003X.

[47] Hideyuki Okano, Erika Sasaki, Tetsuo Yamamori, Atsushi Iriki, Tomomi Shimogori, Yoko Yamaguchi, Kiyoto Kasai, and Atsushi Miyawaki. Brain/minds: A japanese national brain project for marmoset neuroscience. *Neuron (Cambridge, Mass.)*, 92 (3):582–590, 2016. ISSN 0896-6273.

[48] Katrin Amunts, Christoph Ebell, Jeff Muller, Martin Telefont, Alois Knoll, and Thomas Lippert. The human brain project: Creating a european research infrastructure to decode the human brain. *Neuron (Cambridge, Mass.)*, 92(3):574–581, 2016. ISSN 0896-6273.

[49] Jennifer Stine Elam, Matthew F Glasser, Michael P Harms, Stamatios N Sotiropoulos, Jesper LR Andersson, Gregory C Burgess, Sandra W Curtiss, Robert Oostenveld, Linda J Larson-Prior, Jan-Mathijs Schoffelen, et al. The human connectome project: A retrospective. *NeuroImage*, 244:118543, 2021.

[50] Ernest Montbrió, Diego Pazó, and Alex Roxin. Macroscopic description for networks of spiking neurons. *Physical Review X*, 5(2):021028, 2015.

[51] Matteo Martinello, Jorge Hidalgo, Amos Maritan, Serena Di Santo, Dietmar Plenz, and Miguel A Muñoz. Neutral theory and scale-free neural dynamics. *Physical Review X*, 7(4):041071, 2017.

[52] Jonathan Kadmon and Haim Sompolinsky. Transition to chaos in random neuronal networks. *Physical Review X*, 5(4):041030, 2015.

[53] Samaneh Esfandiary, Ali Safari, Jakob Renner, Paolo Moretti, and Miguel A Muñoz. Anomalous lifshitz dimension in hierarchical networks of brain connectivity. *Physical Review Research*, 2(4):043291, 2020.

[54] Guoning Tang, Kesheng Xu, and Luoluo Jiang. Synchronization in a chaotic neural network with time delay depending on the spatial distance between neurons. *Physical Review E*, 84(4), October 2011. doi: 10.1103/physreve.84.046207. URL https://doi.org/10.1103/physreve.84.046207.

[55] A. Spiegler and V. Jirsa. Systematic approximations of neural fields through networks of neural masses in the virtual brain. *NeuroImage*, 83:704–725, December 2013. doi: 10.1016/j.neuroimage.2013.06.018. URL https://doi.org/10.1016/j.neuroimage.2013.06.018.

[56] Michel O. Steinmetz and Andrea E. Prota. Microtubule-targeting agents: Strategies to hijack the cytoskeleton. *Trends in Cell Biology*, 28(10):776–792, October 2018. doi: 10.1016/j.tcb.2018.05.001. URL https://doi.org/10.1016/j.tcb.2018.05.001.

[57] Sebastian Fürthauer, Bezia Lemma, Peter J. Foster, Stephanie C. Ems-McClung, Che-Hang Yu, Claire E. Walczak, Zvonimir Dogic, Daniel J. Needleman, and Michael J. Shelley. Self-straining of actively crosslinked microtubule networks. *Nature Physics*, 15(12):1295–1300, September 2019. doi: 10.1038/s41567-019-0642-1. URL https://doi.org/10.1038/s41567-019-0642-1.

[58] David B. Stein, Gabriele De Canio, Eric Lauga, Michael J. Shelley, and Raymond E. Goldstein. Swirling instability of the microtubule cytoskeleton. *Physical Review Letters*, 126(2), January 2021. doi: 10.1103/physrevlett.126.028103. URL https://doi.org/10.1103/physrevlett.126.028103.

[59] Wen Yan, Saad Ansari, Adam Lamson, Matthew A Glaser, Robert Blackwell, Meredith D Betterton, and Michael Shelley. Toward the cellular-scale simulation of motor-driven cytoskeletal assemblies. *eLife*, 11, May 2022. doi: 10.7554/elife.74160. URL https://doi.org/10.7554/elife.74160.

[60] Peter J Foster, Sebastian Fürthauer, Michael J Shelley, and Daniel J Needleman. From cytoskeletal assemblies to living materials. *Current Opinion in Cell Biology*, 56:109–114, February 2019. doi: 10.1016/j.ceb.2018.10.010. URL https://doi.org/10.1016/j.ceb.2018.10.010.

[61] Pavel Exner, Jonathan P Keating, Peter Kuchment, Alexander Teplyaev, and Toshikazu Sunada. *Analysis on Graphs and Its Applications: Isaac Newton Institute for Mathematical Sciences, Cambridge, UK, January 8-June 29, 2007*, volume 77. American Mathematical Soc., 2008.

[62] Gregory Berkolaiko et al. *Quantum Graphs and Their Applications: Proceedings of an AMS-IMS-SIAM Joint Summer Research Conference on Quantum Graphs and Their Applications, June 19-23, 2005, Snowbird, Utah*, volume 415. American Mathematical Soc., 2006.

[63] Delio Mugnolo. *Mathematical Technology of Networks: Bielefeld, December 2013*, volume 128. Springer, 2015.

[64] Olaf Post. *Spectral analysis on graph-like spaces*, volume 2039. Springer Science & Business Media, 2012.

[65] Pavel Exner and Hynek Kovařík. *Quantum waveguides*. Springer, 2015.

[66] René Dáger and Enrique Zuazua. *Wave propagation, observation and control in 1-d flexible multi-structures*, volume 50. Springer Science & Business Media, 2006.

[67] Delio Mugnolo. *Semigroup methods for evolution equations on networks*, volume 20. Springer, 2014.

[68] S. Jonathan Chapman, David P. Hewett, and Lloyd N. Trefethen. Mathematics of the faraday cage. *SIAM Review*, 57(3):398–417, January 2015. doi: 10.1137/140984452. URL https://doi.org/10.1137/140984452.

[69] Anna M. Lieb, Chris H. Rycroft, and Jon Wilkening. Optimizing intermittent water supply in urban pipe distribution networks. *SIAM Journal on Applied Mathematics*, 76(4):1492–1514, January 2016. doi: 10.1137/15m1038979. URL https://doi.org/10.1137/15m1038979.

[70] Carla Cattaneo. The spectrum of the continuous laplacian on a graph. *Monatshefte für Mathematik*, 124(3):215–235, 1997.

[71] Konstantin Pankrashkin. Spectra of schrödinger operators on equilateral quantum graphs. *Letters in Mathematical Physics*, 77(2):139–154, 2006.

[72] Pavel Exner, Aleksey Kostenko, Mark Malamud, and Hagen Neidhardt. Spectral theory of infinite quantum graphs. In *Annales Henri Poincaré*, volume 19, pages 3457–3510. Springer, 2018.

[73] Robert Carlson. Boundary value problems for infinite metric graphs. *Analysis on graphs and its applications*, 77:355–368, 2008.

[74] Robert Carlson. Dirichlet to neumann maps for infinite quantum graphs. *Networks and Heterogeneous Media*, 7(3):483–501, October 2012. doi: 10.3934/nhm.2012.7.483. URL https://doi.org/10.3934/nhm.2012.7.483.

[75] Pavel Exner, Pavel Hejčík, and Petr Šeba. Approximations by graphs and emergence of global structures. *Reports on Mathematical Physics*, 57(3):445–455, June 2006. doi: 10.1016/s0034-4877(06)80031-5. URL https://doi.org/10.1016/s0034-4877(06)80031-5.

[76] Shu Nakamura and Yukihide Tadano. On a continuum limit of discrete schrödinger operators on square lattice. *Journal of Spectral Theory*, 11(1):355–367, March 2021. doi: 10.4171/jst/343. URL https://doi.org/10.4171/jst/343.

[77] Pavel Exner, Shu Nakamura, and Yukihide Tadano. Continuum limit of the lattice quantum graph hamiltonian. *Letters in Mathematical Physics*, 112(4), August 2022. doi: 10.1007/s11005-022-01576-5. URL https://doi.org/10.1007/s11005-022-01576-5.

[78] Robert Carlson. Linear network models related to blood flow. *Contemporary Mathematics*, 415:65–80, 2006.

[79] Bertrand Maury, Delphine Salort, and Christine Vannier. Trace theorems for trees and application to the human lungs. *Networks & Heterogeneous Media*, 4(3):469, 2009.

[80] Robert Carlson and. Myopic models of population dynamics on infinite networks. *Networks and Heterogeneous Media*, 9(3):477–499, 2014. doi: 10.3934/nhm.2014.9.477. URL https://doi.org/10.3934/nhm.2014.9.477.

[81] Yu V Pokornyi and AV Borovskikh. Differential equations on networks (geometric graphs). *Journal of Mathematical Sciences*, 119(6):691–718, 2004.

[82] Alexandra Tzella and Jacques Vanneste. Dispersion in rectangular networks: Effective diffusivity and large-deviation rate function. *Physical Review Letters*, 117(11), September 2016. doi: 10.1103/physrevlett.117.114501. URL https://doi.org/10.1103/physrevlett.117.114501.

[83] Pim van der Hoorn, William J Cunningham, Gabor Lippner, Carlo Trugenberger, and Dmitri Krioukov. Ollivier-ricci curvature convergence in random geometric graphs. *Physical Review Research*, 3(1):013211, 2021.

[84] Lawrence C Evans and Ronald F Garzepy. *Measure theory and fine properties of functions*. Routledge, 2018.

[85] P. G. De Gennes. Short range order effects in the isotropic phase of nematics and cholesterics. *Molecular Crystals and Liquid Crystals*, 12(3):193–214, February 1971. doi: 10.1080/15421407108082773. URL https://doi.org/10.1080/15421407108082773.

[86] Pavel Exner, Pavel Hejčík, and Petr Šeba. Approximations by graphs and emergence of global structures. *Reports on Mathematical Physics*, 57(3):445–455, June 2006. doi: 10.1016/s0034-4877(06)80031-5. URL https://doi.org/10.1016/s0034-4877(06)80031-5.

[87] Konstantin Pankrashkin. Unitary dimension reduction for a class of self-adjoint extensions with applications to graph-like structures. *Journal of Mathematical Analysis and Applications*, 396(2):640–655, December 2012. doi: 10.1016/j.jmaa.2012.07.005. URL https://doi.org/10.1016/j.jmaa.2012.07.005.

[88] Shu Nakamura and Yukihide Tadano. On a continuum limit of discrete schrödinger operators on square lattice. *Journal of Spectral Theory*, 11(1):355–367, March 2021. doi: 10.4171/jst/343. URL https://doi.org/10.4171/jst/343.

[89] Pavel Exner, Shu Nakamura, and Yukihide Tadano. Continuum limit of the lattice quantum graph hamiltonian. *Letters in Mathematical Physics*, 112(4), August 2022. doi: 10.1007/s11005-022-01576-5. URL https://doi.org/10.1007/s11005-022-01576-5.

[90] Keenan Crane. The n-dimensional cotangent formula. 2019. URL https://api.semanticscholar.org/CorpusID:203578769.

[91] Ken Mraz. Check out the first finite elephant model i ever built... https://greatwhitefrost.net/kenmraz/ken/index.html, 2010. Accessed: 2023-10-25.

[92] Keenan Crane. The n-dimensional cotangent formula, September 2019.

[93] Max Wardetzky. *Convergence of the Cotangent Formula: An Overview*, page 275–286. Birkhäuser Basel, 2008. ISBN 9783764386214. doi: 10.1007/978-3-7643-8621-4_15. URL http://dx.doi.org/10.1007/978-3-7643-8621-4_15.

[94] Stefan Güttel and Françoise Tisseur. The nonlinear eigenvalue problem. *Acta Numerica*, 26:1–94, May 2017. doi: 10.1017/s0962492917000034. URL https://doi.org/10.1017/s0962492917000034.

[95] Wolf-Jürgen Beyn. An integral method for solving nonlinear eigenvalue problems. *Linear Algebra and its Applications*, 436(10):3839–3863, May 2012. ISSN 0024-3795. doi: 10.1016/j.laa.2011.03.030. URL http://dx.doi.org/10.1016/j.laa.2011.03.030.

[96] Matthew J. Colbrook and Alex Townsend. Avoiding discretization issues for nonlinear eigenvalue problems, 2023. URL https://arxiv.org/abs/2305.01691.

[97] Peter Lancaster. *Lambda-matrices and vibrating systems.* International series of monographs in pure and applied mathematics, v. 94. Pergamon Press, Oxford, [1st edition]. edition, 1966. ISBN 9780080116648.

[98] Daniel B. Szyld and Fei Xue. Local convergence of newton-like methods for degenerate eigenvalues of nonlinear eigenproblems. i. classical algorithms. *Numerische Mathematik*, 129(2):353–381, June 2014. ISSN 0945-3245. doi: 10.1007/s00211-014-0639-8. URL http://dx.doi.org/10.1007/s00211-014-0639-8.

[99] Xiao-Ping Chen and Hua Dai. A modified newton method for nonlinear eigenvalue problems. *East Asian Journal on Applied Mathematics*, 8(1):139–150, June 2018. doi: 10.4208/eajam.100916.061117a. URL https://doi.org/10.4208/eajam.100916.061117a.

[100] Miloud Sadkane. A smallest singular value method for nonlinear eigenvalue problems. *Linear and Multilinear Algebra*, 71(1):16–28, January 2022. doi: 10.1080/03081087.2021.2017832. URL https://doi.org/10.1080/03081087.2021.2017832.

[101] D. Girard. Un algorithme simple et rapide pour la validation croisée généralisée sur des problèmes de grande taille. *Inf. et Math. Appl. de Grenoble*, May 1987.

[102] M.F. Hutchinson. A stochastic estimator of the trace of the influence matrix for laplacian smoothing splines. *Communications in Statistics - Simulation and Computation*, 19(2):433–450, January 1990. doi: 10.1080/03610919008812866. URL https://doi.org/10.1080/03610919008812866.

[103] Michael F Hutchinson. A stochastic estimator of the trace of the influence matrix for laplacian smoothing splines. *Communications in Statistics-Simulation and Computation*, 18(3):1059–1076, 1989.

[104] Alice Cortinovis and Daniel Kressner. On randomized trace estimates for indefinite matrices with an application to determinants. *Foundations of Computational Mathematics*, 22(3):875–903, July 2021. doi: 10.1007/s10208-021-09525-9. URL https://doi.org/10.1007/s10208-021-09525-9.

[105] S. Muthukrishnan. Data streams: Algorithms and applications. *Foundations and Trends® in Theoretical Computer Science*, 1(2):117–236, 2005. doi: 10.1561/0400000002. URL https://doi.org/10.1561/0400000002.

[106] Shashanka Ubaru and Yousef Saad. Applications of trace estimation techniques. In *Lecture Notes in Computer Science*, pages 19–33. Springer International Publishing, 2018. doi: 10.1007/978-3-319-97136-0_2. URL https://doi.org/10.1007/978-3-319-97136-0_2.

[107] Haim Avron. Counting triangles in large graphs using randomized matrix trace estimation, 2010. URL https://api.semanticscholar.org/CorpusID:3199817.

[108] Raphael A. Meyer, Cameron Musco, Christopher Musco, and David P. Woodruff. Hutch++: Optimal stochastic trace estimation. In *Symposium on Simplicity in*

Algorithms (SOSA), pages 142–155. Society for Industrial and Applied Mathematics, January 2021. doi: 10.1137/1.9781611976496.16. URL https://doi.org/10.1137/1.9781611976496.16.

[109] David Persson, Alice Cortinovis, and Daniel Kressner. Improved variants of the hutch++ algorithm for trace estimation. *SIAM Journal on Matrix Analysis and Applications*, 43(3):1162–1185, July 2022. doi: 10.1137/21m1447623. URL https://doi.org/10.1137/21m1447623.

[110] Sidney Holden. Metric graph, 2024. URL https://github.com/sidneyholden1/metric_graph.

[111] Jacques Martinet. *Perfect Lattices in Euclidean Spaces*. Springer Berlin Heidelberg, 2003. ISBN 9783662051672. doi: 10.1007/978-3-662-05167-2. URL http://dx.doi.org/10.1007/978-3-662-05167-2.

[112] Robert A. Evarestov. *Quantum Chemistry of Solids: LCAO Treatment of Crystals and Nanostructures*. Springer Berlin Heidelberg, 2012. ISBN 9783642303562. doi: 10.1007/978-3-642-30356-2. URL http://dx.doi.org/10.1007/978-3-642-30356-2.

[113] Henry Y.T. Ngan, Grantham K.H. Pang, and Nelson H.C. Yung. Motif-based defect detection for patterned fabric. *Pattern Recognition*, 41(6):1878–1894, June 2008. ISSN 0031-3203. doi: 10.1016/j.patcog.2007.11.014. URL http://dx.doi.org/10.1016/j.patcog.2007.11.014.

[114] Eli Chertkov and Bryan K. Clark. Motif magnetism and quantum many-body scars. *Physical Review B*, 104(10), September 2021. ISSN 2469-9969. doi: 10.1103/physrevb.104.104410. URL http://dx.doi.org/10.1103/PhysRevB.104.104410.

[115] M. Pitteri. Geometry and symmetry of multilattices. *International Journal of Plasticity*, 14(1–3):139–157, January 1998. ISSN 0749-6419. doi: 10.1016/s0749-6419(97)00045-4. URL http://dx.doi.org/10.1016/S0749-6419(97)00045-4.

[116] Gus L. W. Hart and Rodney W. Forcade. Generating derivative structures from multilattices: Algorithm and application to hcp alloys. *Physical Review B*, 80(1), July 2009. ISSN 1550-235X. doi: 10.1103/physrevb.80.014120. URL http://dx.doi.org/10.1103/PhysRevB.80.014120.

[117] E. D. Sanders, A. Pereira, and G. H. Paulino. Optimal and continuous multilattice embedding. *Science Advances*, 7(16), April 2021. ISSN 2375-2548. doi: 10.1126/sciadv.abf4838. URL http://dx.doi.org/10.1126/sciadv.abf4838.

[118] Branko Grunbaum and G C Shephard. *Tilings and Patterns*. Dover Books on Mathematics. Dover Publications, Mineola, NY, June 2016.

[119] 2005. URL https://www.flickr.com/photos/gruban/11341048/.

[120] 2024. URL https://mcescher.com/gallery/symmetry/.

[121] 2007. URL https://www.nature.com/news/2007/070219/full/news070219-9.html.

[122] https://www.newscientist.com/article/mg24532680-900-spiders-think-with-their-webs-challenging-our-ideas-of-intelligence/, 0000.

[123] Victor Padilla-Sanchez. Structural model of bacteriophage t4. *WikiJournal of Science*, 4(1):5, 2021. doi: 10.15347/wjs/2021.005. URL https://doi.org/10.15347/wjs/2021.005.

[124] Yury Voytekhovsky. On the exotic fishes given to... geometry. *Nature Precedings*, August 2008. doi: 10.1038/npre.2008.2191.1. URL https://doi.org/10.1038/npre.2008.2191.1.

[125] Graziano Vernizzi, Rastko Sknepnek, and Monica Olvera de la Cruz. Platonic and archimedean geometries in multicomponent elastic membranes. *Proceedings of the National Academy of Sciences*, 108(11):4292–4296, February 2011. doi: 10.1073/pnas.1012872108. URL https://doi.org/10.1073/pnas.1012872108.

[126] H.-W. Ackermann. 5500 phages examined in the electron microscope. *Archives of Virology*, 152(2):227–243, October 2006. doi: 10.1007/s00705-006-0849-1. URL https://doi.org/10.1007/s00705-006-0849-1.

[127] André M. Comeau, Graham F. Hatfull, Henry M. Krisch, Debbie Lindell, Nicholas H. Mann, and David Prangishvili. Exploring the prokaryotic virosphere. *Research in Microbiology*, 159(5):306–313, June 2008. doi: 10.1016/j.resmic.2008.05.001. URL https://doi.org/10.1016/j.resmic.2008.05.001.

[128] Richard Lane Calendar, editor. *The Bacteriophages*. Oxford University Press, New York, NY, 2 edition, October 2005.

[129] Geoffrey M Vasil, Daniel Lecoanet, Keaton J Burns, Jeffrey S Oishi, and Benjamin P Brown. Tensor calculus in spherical coordinates using jacobi polynomials. part-i: Mathematical analysis and derivations. *Journal of Computational Physics: X*, 3: 100013, 2019.

[130] Keaton J Burns, Geoffrey M Vasil, Jeffrey S Oishi, Daniel Lecoanet, and Benjamin P Brown. Dedalus: A flexible framework for numerical simulations with spectral methods. *Physical Review Research*, 2(2):023068, 2020.

[131] Daniel Lecoanet, Geoffrey M Vasil, Keaton J Burns, Benjamin P Brown, and Jeffrey S Oishi. Tensor calculus in spherical coordinates using jacobi polynomials. part-ii: implementation and examples. *Journal of Computational Physics: X*, 3: 100012, 2019.

[132] Grigoris Pavliotis and Andrew Stuart. *Multiscale methods*. Texts in Applied Mathematics. Springer, New York, NY, 2008 edition, February 2008.

[133] Leonid Berlyand and Volodymyr Rybalko. *Getting Acquainted with Homogenization and Multiscale*. Springer International Publishing, 2018. ISBN 9783030017774. doi: 10.1007/978-3-030-01777-4. URL http://dx.doi.org/10.1007/978-3-030-01777-4.

[134] Brian Hayes. An adventure in the nth dimension. *American Scientist*, 99(6):442, 2011. ISSN 1545-2786. doi: 10.1511/2011.93.442. URL http://dx.doi.org/10.1511/2011.93.442.